Determining and Optimizing the Current and Magnetic Field Dependence of Spin-Torque and Spin Hall Nano-Oscillators

Toward Next-Generation Nanoelectronic Devices and Systems

SEYED AMIR HOSSEIN BANUAZIZI

Doctoral Thesis in Applied Physics
School of Engineering Sciences
KTH Royal Institute of Technology
Stockholm, Sweden 2018

KTH Royal Institute of Technology
School of Engineering Sciences
Department of Applied Physics
SE-164 40 Kista
SWEDEN

TRITA-SCI-FOU 2018:26
ISBN 978-91-7729-824-3

Akademisk avhandling som med tillstånd av Kungliga Tekniska högskolan framlägges till offentlig granskning för avläggande av doktorsexamen i Fysik fredagen den 15 juni 2018 klockan 10.00 i Sal B, Electrum, Kungl Tekniska högskolan, Kistagången 16, Kista.

Tryck: Universitetsservice US AB

"All praise is for God for all His praiseworthy acts, for all His favors and blessings ... His praise is evident through His generosity, whose bestowal stretches out liberally. His treasures never decrease, rather the frequency of His giving increases His generosity and kindness. Surely He is the Mighty, the Bestower."
Duaa Al-Iftitah (The Supplication of the Opening) by Imam Mahdi (AS)

To my family

Abstract

Spin-torque and spin Hall nano-oscillators are nanoscale devices (about 100 nm) capable of producing tunable broadband high-frequency microwave signals ranging from 0.1 GHz to over 65 GHz that several research groups trying to reach up to 200 - 300 GHz. Their development is ongoing for applications in high-frequency nanoelectronic devices and systems, such as mobile phones, wireless networks, base stations, vehicle radars and even medical applications.

This thesis covers a wide range of characterizations of spin-torque and spin Hall nano-oscillator devices that aim to investigate their current and magnetic field dependency, as well as to suggest improvements in these devices to optimize their application in spintronics and magnonics. The work is primarily based on experimental methods for characterizing these devices by building up new measurement systems, but it also includes numerical and micromagnetic simulations.

Experimental techniques: In order to characterize the fabricated nanodevices in a detailed and accurate manner through their electrical and microwave responses, new measurement systems capable of full 3D control over the external magnetic fields will be described. In addition, a new method of probing an operational device using magnetic force microscopy (MFM) will be presented.

Spin-torque nano-oscillators: We will describe remarkable improvements in the performance of spin-torque nano-oscillators (STNOs) that enhance their integration capability with applications in microwave systems. In nanocontact (NC-) STNOs made from a conventional spin-valve stack, though with thicker bottom electrodes, it is found the auto-oscillations can be excited with higher frequencies at lower threshold currents, and with higher output powers. We also find that this idea is useful for tuning spin-wave resonance and also controlling the thermal budget. Furthermore, a detailed study of magnetic droplet solitons and spin-wave dynamics in NC-STNOs will be described. Finally, we demonstrate ultra-high frequency tunability in low-current STNOs based on perpendicular magnetic tunnel junctions (p-MTJs).

Spin Hall nano-oscillators: Characterizations of spin Hall nano-oscillator (SHNO) devices based on different structures and materials with both conventional and novel methods will be described. A detailed study of the current, temperature, and magnetic field profiles of nanogap SHNOs will be presented. In addition, we show the current and magnetic field dependence of nanoconstriction-based SHNOs. Moreover, it is shown that multiple SHNOs can be serially synchronized, thereby increasing their output power and enhancing the usage of these devices in applications such as neuromorphic computing. We show synchronization of multiple nanoconstriction SHNOs in the presence of a low in-plane magnetic field. Finally, there is a demonstration of the results of a novel method for probing an operational SHNO using MFM.

Keywords: nanoelectronics, spintronics, nanomagnetism, ferromagnetic materials, microwave oscillators, magnetization dynamics, spin waves, giant magneto-resistance, spin Hall effect, spin-torque nano-oscillators, spin Hall nano-oscillators, numerical modeling, electrical characterization, microwave characterization, magnetic force microscopy.

Sammanfattning

Spinntroniska oscillatorer är ca 100 nm stora nano-komponenter som kan generera avstämningsbara mikrovågssignaler över ett mycket stort frekvensområde. Frekvensområdet sträcker sig i dagsläget från 0,1 GHz till över 65 GHz och flera forskningsgrupper försöker att nå upp till 200-300 GHz. De spinntroniska oscillatorerna baseras på en effekt som kallas spinnvridmoment och de första oscillatorerna kallades därför spinnvridmomentsnano-oscillatorer (eng. spin torque nano-oscillators) som vanligtvis förkortas STNO:er. De senaste åren har man även använt den s.k. spinn-Hall-effekten och oscillatorer baserade på detta förkortas därför SHNO:er. Båda sorternas oscillatorer är under kraftig utveckling för att kunna användas inom olika högfrekvenstillämpningar som t.ex. mobiltelefon, trådlösa nätverk, basstationer, fordonsradar och även medicinska tillämpningar.

Denna avhandling täcker ett brett spektrum av olika mätningar på STNO:er och SHNO:er för att bestämma deras ström- och magnetfältsberoenden samt föreslå förbättringar av deras design för att använda dem inom spinntronik och magnonik. Arbetet bygger i första hand på experimentella metoder för att utveckla nya mätsystem, men det innehåller också numeriska och mikromagnetiska simuleringar.

Experimentella tekniker: För att kunna göra detaljerade och noggranna mätningar, som funktion av ström genom komponenten samt magnetfält runt komponenten, har två nya mätuppställningar utvecklats, båda med målet att enkelt kunna variera styrka och riktning på det magnetiska fältet i tre dimensioner. Dessutom presenteras en ny metod för att studera komponenterna med s.k. magnetkraftsmikroskopi (MFM).

STNO:er: Avhandlingen presenterar väsentliga förbättringar av prestanda hos STNO:er genom att öka tjockleken på det understa metall-lager som hela STNO:n är uppbyggd på. I sådana förbättrade STNO:er kan mikrovågssignaler med högre frekvens, högre uteffekt, och lägre tröskelström realiseras. Dessutom får komponenterna bättre värmeledningsförmåga så att de kan klara högre drivströmmar. Vidare beskrivs en detaljerad studie av magnetdroppsolitoner och spinnvågsdynamik i STNO:er. Slutligen beskrivs en ultrahög frekvensavstämbarhet i STNO:er baserade på magnetiska tunnlingselement med s.k. vinkelrät anisotropi.

SHNO:er: Avhandlingen beskriver också mätningar på SHNO:er baserade på olika strukturer och material, studerade med både konventionella och nya metoder. En detaljerad studie av temperatur och magnetfältsprofiler i s.k. nano-gap-SHNO:er presenteras. Dessutom presenterar avhandlingen detaljerade studier av magnetfältsberoendet hos s.k. nano-förträngnings-SHNO:er. Vidare har det visat sig att flera sådana SHNO:er kan synkroniseras seriellt och därigenom få en kraftigt ökad uteffekt. Detta möjliggör i förlängningen också s.k. neuromorfiska beräkningar. Avhandlingen visar att en kedja av sådana SHNO:er också kan synkroniseras även vid låga magnetfält. Slutligen beskrivs de första mätningarna på SHNO:er med hjälp av MFM.

Publications

List of appended papers

(I) **Seyed Amir Hossein Banuazizi**, and Johan Åkerman, *"Microwave probe stations with three-dimensional control of the magnetic field to study high-frequency dynamics in nanoscale devices"*, Accepted for publication in Review of Scientific Instruments (2018).

(II) **Seyed Amir Hossein Banuazizi**, Afshin Houshang, Ahmad A. Awad, Lyubov M. Belova, and Johan Åkerman, *"Magnetic force microscopy of an operational nano device"*, Manuscript.

(III) **Seyed Amir Hossein Banuazizi**, Sohrab R. Sani, Anders Eklund, Maziar M. Naiini, Seyed Majid Mohseni, Sunjae Chung, Philipp Dürrenfeld, B. Gunnar Malm, and Johan Åkerman, *"Order of magnitude improvement of nano-contact spin torque oscillator performance"*, Nanoscale **9**, 1896 (2017).

(IV) Masoumeh Fazlali[†], **Seyed Amir Hossein Banuazizi**[†], Martina Ahlberg, Mykola Dvornik, Sohrab R. Sani, Seyed Majid Mohseni, and Johan Åkerman ([†]*equal contribution*), *"Tuning exchange-dominated spin-waves using lateral current spread in nano-contact spin-torque nano-oscillators"*, Under review in Applied Physics Letters (2018).

(V) **Seyed Amir Hossein Banuazizi**, Seyed Majid Mohseni, Sohrab R. Sani, Anders Eklund, Maziar M. Naiini, B. Gunnar Malm, and Johan Åkerman, *"Control of thermal budget in nanocontact spin torque nano-oscillators"*, Manuscript.

(VI) Morteza Mohseni, M. Hamdi, H. F. Yazdi, **Seyed Amir Hossein Banuazizi**, S. R. Sani, S. Chung, J. Åkerman, and Majid Mohseni, *"Magnetic droplet soliton nucleation in oblique fields"*, Physical Review B **97**, 184402 (2018).

(VII) Quang Tuan Le, Anders Eklund, **Seyed Amir Hossein Banuazizi**, Sunjae Chung, Vahid Fallahi, Thi Ngoc Anh Nguyen, M. Yamanouchi, Eli CI. Enobio, S. Ikeda, Hideo Ohno, Johan Åkerman, *"Ultra-high frequency tunability in low-current spin torque nano-oscillators based on perpendicular magnetic tunnel junctions"*, Manuscript.

(VIII) **Seyed Amir Hossein Banuazizi**, Ahmad A. Awad, Philipp Dürrenfeld, Hamid Mazraati, and Johan Åkerman, *"Current, temperature, and magnetic field profiles in nano-gap spin Hall nano-oscillators"*, Manuscript.

(IX) Hamid Mazraati, **Seyed Amir Hossein Banuazizi**, Seyyed Ruhollah Etesami, Mykola Dvornik, Sunjae Chung, Afshin Houshang, Ahmad A. Awad, and Johan Åkerman, *"Mapping out the in-plane spin wave modes of constriction based spin Hall nano-oscillators"*, Manuscript.

(X) Hamid Mazraati, Shreyas Muradlihar, Seyyed Ruhollah Etesami, Mykola Dvornik, Mohammad Zahedinejad, **Seyed Amir Hossein Banuazizi**, Sunjae Chung, Ahmad A. Awad, and Johan Åkerman, "In-plane field angle dependence of mutually synchronized constriction based spin Hall nano-oscillators", Manuscript.

List of related papers not included in this thesis

(XI) Anders J. Eklund, Stefano Bonetti, Sohrab R. Sani, S. Majid Mohseni, Johan Persson, Sunjae Chung, **Seyed Amir Hossein Banuazizi**, Ezio Iacocca, M. Östling, Johan Åkerman, and B. Gunnar Malm, *"Dependence of the colored frequency noise in spin torque oscillators on current and magnetic field"*, Applied Physics Letters, **104**, 092405 (2014).

(XII) Z. Sheykhifard, S. Majid Mohseni, B. Tork, M. R. Hajiali, L. Jamilpanah, B. Rahmati, F. Haddadi, M. Hamdi, S. Morteza Mohseni, M. Mohammadbeigi, A. Ghaderi, S. Erfanifam, M. Dashtdar, F. Feghhi, N. Ansari, S. Pakdel, M. Pourfath, A. Hosseinzadegan, M. Bahreini, S. H. Tavassoli, M. Ranjbar, **Seyed Amir Hossein Banuazizi**, S. Chung, J. Åkerman, N. Nikkam, A. Sohrabi, S. E. Roozmeh, *"Magnetic graphene/Ni-nano-crystal hybrid for small field magnetoresistive effect synthesized via electrochemical exfoliation/deposition technique"*, Journal of Materials Science: Materials in Electronics **29(5)** (2018): 4171–4178.

Contents

Contents **xi**

Acknowledgements **xiii**

List of Figures **xv**

Symbols and Abbreviations **xvii**

Summary of Appended Papers **xxi**

1 Introduction **1**

2 Theoretical Background **5**
2.1 Magnetism and Magnetic Materials 5
2.2 Anisotropic Magnetoresistance 6
2.3 Giant Magnetoresistance 6
2.4 Tunneling Magnetoresistance 7
2.5 Spin-Transfer Torque 8
2.6 Spin Hall Effect 10

3 Fabrication and Experimental Techniques **11**
3.1 Device Fabrication Process 11
3.2 Measurement Techniques 14
3.3 Developed Measurement and Characterization Systems 17

4 Spin-Torque Nano-Oscillators **31**
4.1 Improvement of NC-STNO Performance 32
4.2 Spin-Transfer Torque Ferromagnetic Resonance of NC-STNOs . 40
4.3 Tuning Spin-Wave Resonance in NC-STNOs 42
4.4 Control of Thermal Budget in NC-STNOs 46
4.5 NC-STNO in Oblique Magnetic Fields: Characterization of High Frequency Responses 49

4.6 NC-STNO in Oblique Magnetic Fields: Magnetic Droplet Soliton Nucleation 53
4.7 Low-Current STNOs Based on Perpendicular Magnetic Tunnel Junctions 58

5 Spin Hall Nano-Oscillators **63**
5.1 Current, Field, and Temperature Profiles in Nanogap SHNOs . . 64
5.2 Mapping Out the In-Plane Modes of Nanoconstriction-Based SHNOs 70
5.3 In-plane Mutual Synchronization of Nanoconstriction-Based SHNOs 76
5.4 Magnetic Force Microscopy of Nanoconstriction-Based SHNOs . 79

6 Conclusion and Future Work **83**

Bibliography **85**

7 Papers **101**

Acknowledgements

I received my M.Sc. in Systems, Control, and Robotics from KTH Royal institute of Technology in 2013 after completing my thesis at the Applied Spintronics Laboratory. While working on my thesis, I developed and built two new measurement systems for characterizing nanoelectronic devices, and became eager to continue as a Ph.D. student in the attractive and cutting-edge field of *spintronics*. This thesis summarizes my four years' work as a Ph.D. student at the Applied Physics department. I am very thankful to everyone who supported me, both professionally and personally, and made my Ph.D. studies an interesting, educational, and exciting part of my life.

I would like to express my deepest gratitude to Professor Johan Åkerman, first for giving me the incredible opportunity to work under his supervision at the Applied Spintronics Group, and also for his help in find my way through the world of nanotechnology, regarding which he patiently taught me much of value. Besides his scientific excellence, he is a skilled project manager who kindly and systematically encouraged me to explore, and gave me the courage to innovate.

I am thankful to Associate Professor B. Gunnar Malm for his integrity and excellent feedback, to Professor Liubov Belova for sharing her insights during our successful collaborations, and to Assistant Professor Martin Månsson for his precise and valuable comments in his review of this thesis.

Furthermore, I would like to thank my senior colleagues and friends in our research group, Assistant Professor Seyed Majid Mohseni for his continuous professional discussions and support—as well as his kindness and generosity—Dr. Sohrab R. Sani for his amiabile, pleasant, and cooperative spirit, and Dr. Sunjae Chung for his valuable training. I also would like to thank Dr. Ahmad A. Awad, Dr. Quang Tuan Le, Dr. Masoumeh Fazlali, Dr. Anders Eklund, Dr. Maziar A. M. Naiini, Dr. Philipp Dürrenfeld, Dr. Randy K. Dumas, Dr. Martina Ahlberg, Dr. Mykola Dvornik, and Dr. Afshin Houshang for the invaluable discussions and inspiring collaborations we have had over the years.

I would like to express my appreciation to my office mates Hamid Mazraati, Sheng Jiang, and Dr. Fatjon Qejvanaj for their fruitful support and collaboration. Fredrik Magnusson is also due thanks for his great technical assistance and pleasant fika breaks at NanOsc.

I would like to acknowledge all my past and current colleagues in the Applied Spintronics group at both KTH and the University of Gothenburg: Dr. Anh Nguyen, Assistant Professor Pranaba Muduli, Dr. Mojtaba Ranjbar, Dr. Mohammad Haidar, Dr. Ezio Iacocca, Dr. Yuli Yin, Mohammad Zahedinejad, Dr. Seyyed Ruhollah Etesami, Dr. Himanshu Fulara, Dr. Roman Khymyn, Shreyas Muradlihar, and Jinjin Yue.

Special thanks go to my best friends at Electrum: Dr. Seyed Hassan Sohofi, Dr. Seyed Hossein Attarzadeh Niaki, Dr. Nader Nikkam, Amin Azari, Meysam Masoudi, Rehan Raza and Dr. Saleh Kargarrazi for the interactive discussions and all the good memories.

I thank the departmental administrators over the years—Madeleine Printzsköld, Susy Mathew, Sara Tiste, and Jonna Holmlund Åsman—for their kindness in organizing administrative issues.

I thank everyone who has helped me carry out this research and all the research organizations, institutions, and companies that have funded it.

I owe a deep appreciation to Assistant Professor Alireza Tavakoli Targhi who, like an older brother, encouraged and guided me over the years, even before I moved to Sweden. I have learned a great deal from him, and I am grateful to have such a friend who helped me out and improved my knowledge and worldview.

Last but not least, my deepest and heartfelt gratitude and appreciation goes to all members of my family for their love, patience, prayers, unconditional support, and blessings. I dedicate this thesis to you!

Seyed Amir Hossein Banuazizi,
Stockholm, May 2018

سیدامیرحسین بنوعزیزی
استکهلم، خرداد ۱۳۹۷

List of Figures

2.1 Schematic of the basic GMR concept 7
2.2 Illustration of the terms in the Landau–Lifshitz–Gilbert–Slonczewski equation 9
2.3 Schematic of a spin-torque nano-oscillator 9
2.4 Illustration of spin Hall effect concept 10

3.1 AJA sputtering machine 11
3.2 Sputtering process 12
3.3 AGM measurement system 13
3.4 Fabricated NC-STNO device 14
3.5 Schematic of the ST-FMR measurement set-up 14
3.6 Schematic of the microwave measurement set-up 15
3.7 Transmission line for microwave measurements 16
3.8 Components of developed field rotational microwave probe station . 19
3.9 Developed field rotational microwave probe station 21
3.10 Developed control panel of the field rotational microwave probe station 22
3.11 Schematic of developed 3D field rotational microwave probe station 24
3.12 Developed 3D field rotational microwave probe station 25
3.13 Developed control panel of the 3D field rotational microwave probe station 26
3.14 Magnetic field characterization of the 3D field rotational microwave probe station 27
3.15 MFM set-up 29
3.16 Developed MFM stage for microwave measurements 30

4.1 NC-STNO device schematic and SEM image 33
4.2 Resistance of NC-STNOs 34
4.3 Simulations of NC-STNO devices (Current density) 35
4.4 Power spectral density of NC-STNO devices as a function of current 37
4.5 Extracted and calculated threshold current of NC-STNO devices . . 38
4.6 Integrated power and power conversion efficiency of NC-STNO devices 39
4.7 ST-FMR spectra of an NC-STNO device 41

4.8 ST-FMR spectrum of NC-STNO devices 42
4.9 Mean value of effective diameter in NC-STNO devices 43
4.10 Simulations of NC-STNO devices (Oe field) 44
4.11 Simulations of an NC-STNO device (Joule heating) 47
4.12 Calculated Joule heating in all layers of an NC-STNO device 48
4.13 Calculated Joule heating in NC-STNO devices 48
4.14 Power spectral density of an NC-STNO as a function of OOP field angle 49
4.15 Power spectral density of an NC-STNO as a function of IP field angle 50
4.16 Properties of the output spectrum of an NC-STNO 51
4.17 Angular field-dependent MR of the NC-STNO 53
4.18 Field-magnitude-dependent MR of NC-STNO 54
4.19 Power spectral density of NC-STNO as a function of applied field angle 55
4.20 Spatial profiles of spin-wave excitations of NC-STNO at OOP field angles 56
4.21 Phase diagram of the droplet nucleation critical angles θ_c 57
4.22 Schematic of MTJ-based STNO device structure 58
4.23 Power spectral density as a function of current in MTJ-based STNOs 59
4.24 Field-magnitude dependency of MTJ-based STNO frequency 60
4.25 Power spectral density as a function of applied field in MTJ-based STNOs 61

5.1 Nanogap SHNO device schematic and SEM image 64
5.2 Power spectral density and AMR curves of a nanogap SHNO 65
5.3 Normalized AMR curves of a nanogap SHNO 66
5.4 Simulations of a nanogap SHNO (Joule heating) 68
5.5 Simulations of a nanogap SHNO (Oe field) 69
5.6 Nanoconstriction-based SHNO schematic and AMR curve 70
5.7 Power spectral density and linewidth of a nanoconstriction-based SHNO (Current dependency) 71
5.8 Power spectral density and linewidth of a nanoconstriction-based SHNO (Field angle dependent) 72
5.9 Simulation of power colormap and normalized volume in a nanoconstriction-based SHNO (Current dependent) 73
5.10 Simulation of mode profile of a nanoconstriction-based SHNO 74
5.11 Schematic and power spectral density of a double nanoconstriction-based SHNO (current dependency) 77
5.12 Power spectral density of a double nanoconstriction-based SHNO (field angle dependency) 78
5.13 Nanoconstriction-based SHNO schematic and SEM image 79
5.14 Nanoconstriction-based SHNO on the stage of the MFM system . . 80
5.15 AFM and MFM of a nanoconstriction-based SHNO 81

Symbols and Abbreviations

List of Symbols

α	Gilbert damping constant
ΔH	linewidth (FWHM)
ΔH_0	inhomogeneous linewidth broadening
$\theta, \theta_{\mathrm{ext}}$	out-of-plane angle of external field
θ_{int}	out-of-plane angle of magnetization
θ_{lin}	linear internal magnetization angle
Θ_{SH}	spin Hall angle
$\rho_{\parallel}$	resistivity for current parallel to magnetization
$\rho_{\perp}$	resistivity for current perpendicular to magnetization
σ^{s}_{xy}	transverse Hall conductivity
τ	spin-torque coefficient
φ	in-plane angle of external field
A	exchange stiffness
$\vec{B}, B$	magnetic flux
$d, d_{\mathrm{NM}}, d_{\mathrm{FM}}$	layer thickness
d_{cc}	distance between two constrictions
f_0	ferromagnetic resonance frequency
f_{rf}	(external) microwave frequency
$\vec{H}_{\mathrm{eff}}$	effective magnetic field
H, H_{ext}	external magnetic field
H_0	ferromagnetic resonance field
H_{ex}	exchange field
H_{int}	internal magnetic field
H_{Oe}	Oersted field

List of Symbols (continued)

h_{rf}	microwave magnetic field
I	current
I_{beam}	ion beam current
$J_{C,\mathrm{rf}}$	microwave charge-current density
$J_{S,\mathrm{rf}}$	microwave spin-current density
$\overrightarrow{k}$	wave vector
$\overrightarrow{M}$	magnetization
M_0	saturation magnetization
M_{eff}	effective magnetization
N	nonlinear frequency coefficient
p	PSSW mode quantization number
$\overrightarrow{P}$	polarization of spin or charge current
t	time
U_{acc}	ion beam acceleration voltage
U_{beam}	ion beam voltage
V_{mix}	mixing voltage

List of Physical Constants

$\gamma/2\pi$	gyromagnetic ratio of the electron	28.0240 GHz/T
μ_0	vacuum permeability	$4\pi \times 10^{-7}$ Vs/(Am)
μ_B	Bohr magneton	9.274×10^{-24} J/(T)
e	elementary charge	1.602×10^{-19} C
$\hbar$	reduced Planck constant	1.055×10^{-34} Js

List of Abbreviations

μ-BLS	microfocused Brillouin light scattering
ac	alternating current
AFM	atomic force microscope
AHE	anomalous Hall effect
AMR	anisotropic magnetoresistance
dc	direct current
CPW	coplanar waveguide
DUT	device under test

List of Abbreviations (continued)

EBL	electron beam lithography
FM	ferromagnet, ferromagnetic
FMR	ferromagnetic resonance
FWHM	full width at half maximum
GMR	giant magnetoresistance
HV	high vacuum
IBE	ion beam etching
LLGS	Landau–Lifshitz–Gilbert–Slonczewski (equation)
LNA	low-noise amplifier
MFM	magnetic force microscope
MTJ	magnetic tunnel junction
NC	nanocontact
NC-STNO	nanocontact spin-torque nano-oscillator
NM	nonmagnet, nonmagnetic
rf	radio frequency
PSD	power spectral density
PSSW	perpendicular standing spin wave
Py	permalloy ($Ni_{80}Fe_{20}$)
RBW	resolution bandwidth
RIE	reactive ion etching
SEM	scanning electron microscope
SHE	spin Hall effect
SHNO	spin Hall nano-oscillator
ST-FMR	spin-torque ferromagnetic resonance
STNO	spin-torque nano-oscillator
STT	spin-transfer torque
SV	spin valve
SW	spin wave
TMR	tunneling magnetoresistance
VBW	video bandwidth
YIG	yttrium iron garnet ($Y_3Fe_gO_{12}$)

Summary of Appended Papers

- **Paper I:**
  Seyed Amir Hossein Banuazizi and Johan Åkerman, *"Microwave probe stations with three-dimensional control of the magnetic field to study high-frequency dynamics in nanoscale devices"*, Accepted for publication in Review of Scientific Instruments (2018).
  Summary: This paper presents the design and implementation of two microwave probe stations with the results of electrical and microwave measurements of NC-STNOs and SHNOs to test and demonstrate the ability of these two systems.
  Author's contribution: The author designed and built the measurement systems, performed all measurements, and contributed to analyzing the data and writing the manuscript.

- **Paper II:**
  Seyed Amir Hossein Banuazizi, Afshin Houshang, Ahmad A. Awad, Lyubov M. Belova, and Johan Åkerman, *"Magnetic force microscopy of an operational nano device"*, Manuscript.
  Summary: This paper describes the development of a magnetic force microscope for scanning an operational nanoscale device presents the results of probing an operational nanoconstriction-based SHNO device.
  Author's contribution: The author developed the magnetic force microscopy system by designing and building the microwave probe station and contributed to the design of the nanodevice, the electrical microwave measurements, the magnetic force microscopy, the data analysis, and the writing of the manuscript.

- **Paper III:**
  Seyed Amir Hossein Banuazizi, Sohrab R. Sani, Anders Eklund, Maziar M. Naiini, Seyed Majid Mohseni, Sunjae Chung, Philipp Dürrenfeld, B. Gunnar Malm, and Johan Åkerman, *"Order of magnitude improvement of nano-contact spin torque oscillator performance"*, Nanoscale **9**, 1896 (2017).
  Summary: This paper discusses the impact of the thickness of the NC-STNO Cu underlayer on both the auto-oscillation threshold current (I_c) and the

microwave output power. Based on experimental results and numerical simulations, I_c can be reduced by as much as 40% and the output power can be increased by an order of magnitude by increasing the Cu thickness of the underlayer from 10 to 70 nm.
Author's contribution: The author developed the electrical microwave measurement circuit and performed all measurements, developed the numerical simulations, analyzed the data, analyzed the results, and wrote the manuscript.

- **Paper IV:**
  Masoumeh Fazlali[†], Seyed Amir Hossein Banuazizi[†], Martina Ahlberg, Mykola Dvornik, Sohrab R. Sani, Seyed Majid Mohseni, and Johan Åkerman, *"Tuning exchange-dominated spin-waves using lateral current spread in nano-contact spin-torque nano-oscillators"*, Under review in Applied Physics Letters (2018).
  Summary: This paper discusses the possibility of tuning the spinwave resonance mode by altering the current distribution and thus the distribution of the Oersted field (H_{Oe}) by varying the thickness of the Cu underlayer in NC-STNOs.
  Author's contribution: ([†]*equal contribution*) The author developed and implemented the numerical simulations, contributed to the data analysis and to the writing of the manuscript.

- **Paper V:**
  Seyed Amir Hossein Banuazizi, Seyed Majid Mohseni, Sohrab R. Sani, Anders Eklund, Maziar M. Naiini, B. Gunnar Malm, and Johan Åkerman, *"Control of thermal budget in nanocontact spin torque nano-oscillators"*, Manuscript.
  Summary: This paper investigates Joule heating in GMR nanocontact STNO by means of numerical simulations. The results show that by increasing the Cu thickness of the lower electrode from 10 to 70 nm, the temperature of the ferromagnet can be lowered down by around 50%.
  Author's contribution: The author developed and executed the numerical simulations, analyzed the data, and wrote the manuscript.

- **Paper VI:**
  Morteza Mohseni, M. Hamdi, H. F. Yazdi, Seyed Amir Hossein Banuazizi, S. R. Sani, S. Chung, J. Åkerman, and Majid Mohseni, *"Magnetic droplet soliton nucleation in oblique fields"*, Physical Review B **97**, 184402 (2018).
  Summary: This paper presents evidence of droplet dynamics in oblique fields using electrical measurements of NC-STNOs, supported by micromagnetic simulations. The results show that the droplet is present in oblique fields while a transition occurs in certain angles, where the droplet changes to another propagating spin wave type. This was verified by simulations and by determining the spin-wave nonlinear coefficient.

Author's contribution: The author contributed to developing the measurement techniques, electrical microwave measurements, and writing the manuscript.

- **Paper VII:**
  Quang Tuan Le, Anders Eklund, Seyed Amir Hossein Banuazizi, Sunjae Chung, Vahid Fallahi, Thi Ngoc Anh Nguyen, M Yamanouchi, Eli CI Enobio, S Ikeda, Hideo Ohno, and Johan Åkerman, *"Ultra-high frequency tunability in low-current spin torque nano-oscillators based on perpendicular magnetic tunnel junctions"*, Manuscript.
  Summary: This paper discusses STNOs based on nanopillar MTJs, in which both the free and polarizer layers are PMA CoFeBs. The results demonstrate high-frequency STNO operation from 5 GHz to 10 GHz in a 100 nm nanopillar based on a perpendicular-anisotropy CoFeB-MgO magnetic tunnel junction; this is the highest oscillation frequency achieved in the family of MgO-based MTJ nanopillar STNOs. The paper also demonstrates ultra-high current frequency tunabilities (up to 4.4 GHz/mA) and extremely low-onset current densities (on the order of 10^5 A/cm^2).
  Author's contribution: The author contributed to developing the measurement techniques, the electrical microwave measurements, the data analysis, and the writing of the manuscript.

- **Paper VIII:**
  Seyed Amir Hossein Banuazizi, Ahmad A. Awad, Philipp Dürrenfeld, Hamid Mazraati, and Johan Åkerman, *"Current, temperature, and magnetic field profiles in nano-gap spin Hall nano-oscillators"*, Manuscript.
  Summary: This paper presents a study of the current, field, and temperature profiles of nanogap spin Hall nano-oscillators based on both experimental measurements and numerical simulations.
  Author's contribution: The author performed all the electrical and microwave measurements, developed the numerical simulations, analyzed the data, and wrote the manuscript.

- **Paper IX:**
  Hamid Mazraati, Seyed Amir Hossein Banuazizi, Seyyed Ruhollah Etesami, Mykola Dvornik, Sunjae Chung, Afshin Houshang, Ahmad A. Awad, and Johan Åkerman, *"Mapping out the in-plane spin wave modes of constriction based spin Hall nano-oscillators"*, Manuscript.
  Summary: This paper discusses the auto-oscillating spin-wave modes in nanoconstriction-based SHNOs as a function of current, external in-plane magnetic field magnitude and angle, and constriction size.
  Author's contribution: The author contributed to the electrical microwave

measurements, the data analysis, and the writing of the manuscript.

- **Paper X:**
  Hamid Mazraati, Shreyas Muradlihar, Seyyed Ruhollah Etesami, Mykola Dvornik, Mohammad Zahedinejad, Seyed Amir Hossein Banuazizi, Sunjae Chung, Ahmad A. Awad, and Johan Åkerman, "In-plane field angle dependence of mutually synchronized constriction based spin Hall nano-oscillators", Manuscript.
  Summary: This paper presents for the first time mutual SHNO synchronization in in-plane fields (H_{IP}) as low as 30 mT.
  Author's contribution: The author contributed to the data analysis and to the writing of the manuscript.

Chapter 1

Introduction

Nanoscale magnetic materials have attracted considerable attention in recent decades in terms of novel magnetic structures [1], nanocomposite magnets [2], spintronic devices [3, 4], domain-structure and domain-wall motion for applications in recording devices [5], microelectromechanical systems (MEMS) [6], telecommunications [7], and the aerospace industry [8], as well as biosensors [9, 10], energy applications [11], and more recently neuromorphic computing [12].

Specifically, the utilization of the *spin* degree of freedom and the discovery of *spin-transfer torque* [13] have revolutionized nanoelectronic systems based on *spintronic* devices [14]. The origin of spintronics lies in giant magnetoresistance (GMR), which Albert Fert and Peter Grünberg separately discovered in 1988 in ferromagnetic (FM)–nonmagnetic (NM) metallic multilayers [15, 16] and for which they jointly won the 2007 Nobel Prize in Physics [17, 18].

Spintronics components are now the basis of all magnetic hard disk drives, where they implement high-performance nonvolatile magnetic random access memory (MRAM) [5, 19, 20]. Moreover, microwave spintronics has the potential to transform the design of high-frequency microwave systems [21] and it shows great promise for magnetic field sensors [22] and as an enabler of spin-wave logic devices as an alternative to today's transistor-based computer logic [23, 24]. It also has potential to contribute to microwave-band wireless communication—for example, 4G mobile phones currently utilize frequencies up to 2 GHz, and 5G technology is being designed to use frequencies up to 100 GHz [25].

Spin-torque and spin Hall nano-oscillators [26, 27, 28, 29, 30] are two examples of nanosized spintronic devices that can generate GHz microwave frequencies and are highly promising for a variety of applications. Spin-torque nano-oscillators (STNOs) are CMOS-integrable [31, 32, 33] and have highly tunable frequencies for applications in microwave technology [34], where strong frequency dependence on a magnetic field is an advantage. This makes the technology an excellent candidate for the the next generation of magnetic field sensors [22].

In STNOs, spin-transfer torque (STT) [35, 36, 37] from a direct spin-polarized current drives and controls the auto-oscillation of the local free-layer magnetization which, through its oscillating magnetoresistance, transforms the direct current into a tunable microwave voltage. Recent investigations have shown that the spin Hall effect (SHE) in a nonmagnetic film with a strong spin-orbit interaction (e.g., Pt and W) [38, 39, 40] can induce pure spin currents that may be used to exert enough STT onto an adjacent ferromagnetic thin film to drive the spin-wave auto-oscillations. This is the basis of SHNO device functionality.

Thesis Outline

The aim of this thesis is to develop spintronic devices for use in real applications as signal generators and sensors in nanoelectronic circuits and computing devices. A wide range of characterizations of spin-torque and spin Hall nano-oscillator devices is performed in order to investigate their current and magnetic field dependencies and to propose improvements for optimizing the applicability of nano-oscillator devices in spintronics [14] and magnonics [41]. The work is primarily based on experimental methods of characterizing the developed devices by building new measurement systems, but also includes numerical and micromagnetic simulations in order to gain a better understanding of the operational mechanisms of the devices and to confirm the experimental results. The main material of the thesis is presented in three chapters:

1. Fabrication and Experimental Techniques:

This chapter has 2 sections:

i) Fabrication processes: the process of fabricating the spin-torque and spin Hall nano-oscillator devices is briefly described.

ii) Measurement techniques: After fabrication, all the devices were characterized by their electrical and microwave responses in an external magnetic field under the application of dc and microwave currents. Since anisotropic magnetic materials and the spin-torque effect are angle dependent, studying magnetic films and devices for room temperature applications requires the use of a probe station equipped with high-frequency tools capable of changing the magnetic field's direction with respect to the sample plane. This chapter presents the general methodology followed in characterizing the devices and introduces two new measurement systems that allow full 3D control of the external magnetic field. In addition, a new method of probing an operational nanodevice using magnetic force microscopy (MFM) is presented.

2. Spin-Torque Nano-Oscillators:

In this chapter, remarkable improvements in the performance of spin-torque nano-oscillators (STNOs) are described, with the support of experimental results and simulations. The auto-oscillation dynamic properties of nanocontact spin-torque nano-oscillators (NC-STNOs) constructed from a conventional spin-valve stack—though with thicker bottom electrodes—are described, and auto-oscillations with higher frequencies at lower threshold currents and higher output powers are demon-

strated. Further, it is shown that using a thicker copper layer for the bottom electrode is useful in tuning the spin-wave resonance and controlling the thermal budget in NC-STNOs. Further, we present two types of NC-STNO in oblique magnetic fields with detailed studies characterizing their high-frequency responses, as well as their magnetic droplet solitons and spin-wave dynamics. Finally, we introduce a low-current STNO based on perpendicular magnetic tunnel junctions (p-MTJs) with ultrahigh frequency tunability.

3. Spin Hall Nano-Oscillators:
This chapter describes the characterizations of spin Hall nano-oscillator (SHNO) devices based on different structures and materials, using conventional and novel methods. A detailed study of current and induced magnetic field, as well as the temperature profiles of nanogap SHNOs, are presented. This is be followed by descriptions of the dependencies on current and in-plane magnetic fields of nanoconstriction spin Hall nano-oscillators based on NiFe/Pt and NiFe/W. It has been shown that multiple SHNOs can be serially synchronized, thereby increasing their output power and enhancing the value of these devices in applications. Here we show the dependency of synchronization in multiple of nanoconstriction SHNOs on a low in-plane magnetic field. Finally, we present the results of a novel method of probing an operational nanoconstriction-based SHNO using MFM.

Chapter 2

Theoretical Background

2.1 Magnetism and Magnetic Materials

Applied physics aims to use and study basic materials for a range of different purposes, such as semiconductor physics, optics, photonics, and quantum physics, with the aim of developing advanced microelectronic and nanoelectronic devices and systems, including data communications systems, memory systems, sensor systems, optical and electro-optical systems, and power supplies. In particular, to develop rapid memory systems, wireless communications, and sensitive sensors, spintronics is being used to design nanoelectronic components based on the the magnetic properties of materials. Magnetic random access memory (MRAMs), signal generators, and magnetic sensors are among the most significant devices based on spintronics.

Magnetic materials are the basis of all spintronics devices. Spin is an exclusively quantum mechanical phenomenon carried by elementary particles as an intrinsic form of angular momentum [42]. Various situations are found in atoms: in most, the electrons occur in pairs with opposite spins, which give rise to mutually canceling magnetic fields. On the other hand, some materials—the ferromagnetic materials such as‘ nickel, cobalt, and iron—have unpaired electrons that generate a net magnetic field and which significantly respond to external magnetic fields. On the other hand, as a result of the Zeeman effect, ferromagnetic materials have a spin split density of state which causes spin polarization in electrons [43]. As a result, current flowing through these materials becomes spin polarized.

Ferromagnetic materials possess an intrinsic resonance mechanism, called ferromagnetic resonance (FMR) [44]. The actual FMR frequency depends on the material, and typically lies in the microwave regime, ranging from a few GHz to tens of GHz. By exciting and driving the FMR by applying an external magnetic field and sending an electric current through the material, the spin-transfer torque effect will drive the oscillation [13].

The output electrical oscillations arise from the giant magnetoresistance effect (GMR), for which the Nobel Prize in Physics was awarded in 2007 [15, 16]. Based on physical phenomena such as GMR, the spin Hall effect (SHE) [45, 46], spin-transfer torque (STT)[35, 36, 37], and tunneling magnetoresistance (TMR) [47, 48], various magnetodynamical mechanisms can be excited in magnetic thin films and devices using dc electrical currents. For example, since the late 1990s, improvements in the GMR and TMR effects have driven the development of hard disks, which now employ GMR-based and TMR-based sensor heads to read the weak magnetic fields of magnetic domains pointing either up or down, representing stored zeros and ones.

2.2 Anisotropic Magnetoresistance

In ferromagnetic materials, the dependence of electric resistance on the orientation of the current flow with respect to the magnetization direction is called anisotropic magnetoresistance (AMR) [49]. This angular dependency of resistance is described by:

$$\rho = \rho_{\perp} + (\rho_{\parallel} - \rho_{\perp})\ cos^2\theta \tag{2.1}$$

where $\rho_{\perp}$ and $\rho_{\perp}$ represent the resistivity of the ferromagnet when current flow and magnetization direction are in the perpendicular and parallel states, respectively, and θ is an arbitrary angle between these two. AMR arises as the effect of both spin-orbit coupling and the magnetization on the charge carriers.

2.3 Giant Magnetoresistance

Giant magnetoresistance (GMR), which was discovered in magnetic multilayers by Albert Fert and Peter Grünberg (for which they jointly won the Physics Nobel Prize in 2007 [15, 16]), refers to the variation in resistance of ferromagnetic (FM)–nonmagnetic (NM) metallic multilayers. Fert and Grünberg showed that, in a multilayer structure consisting of magnetic and metallic thin films (their study used Fe and Cr layers), the resistance depends on the magnetization orientation of the magnetic layers. This leads to low resistance for parallel and high resistance for antiparallel ferromagnetic layers (Figure 2.1) [50].

In addition, the magnetoresistance (MR) ratio quantifies GMR effect:

$$MR = \frac{R_{AP} - R_P}{R_P}. \tag{2.2}$$

Here R_{AP} is the resistance in the antiparallel structure and R_P is the resistance in the parallel structure. For spintronics applications, a high value of GMR ration is required. In these structures (Figure 2.1), we can have two situations describing the flow of current:

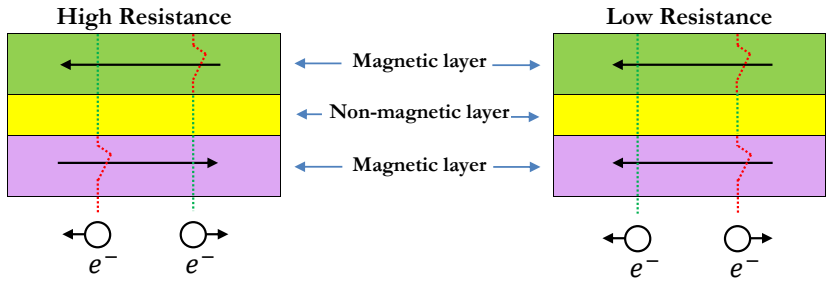

Figure 2.1: Schematic of the basic GMR concept. Overall resistance is high when the directions of the magnetic layers are in antiparallel alignment; resistance is low when they are in parallel alignment.

1. Current in plane (CIP), where the current flows parallel to the layers;
2. Current perpendicular to plane (CPP), where the current flows perpendicularly to the magnetic layers, increases scattering events and thus the MR ratio.

To achieve the spin-transfer torque effect which will be described later, a high spin-polarized current is required. This can be achieved in CPP structures by fabricating specific geometries like nanopillar or nanocontact.

2.4 Tunneling Magnetoresistance

In tunneling magnetoresistance (TMR), the layer structure is similar to that of GMR, except that the ferromagnetic layers (the reference layer and the free layer) are separated by an ultrathin insulating layer. In magnetic tunnel junctions (MTJs), electrons can tunnel through the thin insulating layer, the probability of which depends on the relative magnetization direction between the two ferromagnetic layers. Then, as with GMR, resistance is low when the magnetization orientations of the free and reference layers are parallel, and resistance is high when the layers are antiparallel to each other. The TMR ratio in a MTJ is defined as:

$$TMR = \frac{2P_1P_2}{1 - P_1P_2}, \tag{2.3}$$

where P_1 and P_2 are the spin polarizations of the ferromagnetic layers:

$$P_i = \frac{D_{i\uparrow} - D_{i\downarrow}}{D_{i\uparrow} + D_{i\downarrow}};\ i = 1, 2. \tag{2.4}$$

Here, at the Fermi energy level of the ferromagnet, $D_{i\uparrow}$ and $D_{i\downarrow}$ are the density of up-spin and down-spin electrons. In addition, while the GMR ratio is on the order of a few percent (1%–2%) [51], the TMR ratio may exceed 150% [52, 53].

2.5 Spin-Transfer Torque

As discussed in the previous sections, structures with antiparallel moments have higher electrical resistance. In addition, calculations have shown that the spin-polarized current that flows perpendicular to the plane in these structures can transfer angular momentum between the layers and thus cause a torque on the magnetic moments [36, 35, 50].

To experimentally observe this phenomenon, it has proven necessary to use a soft magnetic material with high spin polarized density. Experiments on the small scale have shown that, in a structure with the current perpendicular to plane (CPP), this can be achieved using a thick magnetic layer (fixed layer) to polarize the current while the other layer is thin (free layer) and causes spin-transfer effects. These CPP structures are called spin valves (SVs) [54, 55, 13]. Magnetization dynamics refer to the time evolution of the magnetic properties of the system; they can help us understand basic phenomena and may also possess industrial applications. The dynamics of magnetic domains are generally described by the Landau–Lifshitz–Gilbert (LLG) equation with an additional Slonczewski spin-torque term (Figure 2.2):

$$\begin{aligned}\frac{\partial \vec{M}}{\partial t} = &- \gamma(\vec{M} \times \vec{H}_{\text{eff}}) \\ &+ \frac{\gamma\alpha}{M_0}\Big[\vec{M} \times (\vec{M} \times \vec{H}_{\text{eff}})\Big] \\ &+ \tau\Big[\vec{M} \times (\vec{M} \times \vec{P})\Big].\end{aligned} \tag{2.5}$$

Here $\vec{M}$ is the magnetization direction, $\vec{H}_{\text{eff}}$ is the effective magnetic field, and γ is the gyromagnetic ratio. The first (blue) term is called the Larmor precession and describes how the direction of magnetization precesses around the effective magnetic field. Also, α is the Gilbert damping parameter, and the second (red) term is related to Gilbert damping, which forces the magnetization vector to skew around the effective field direction. The effective field can described as:

$$H_{\text{eff}} = -\frac{\partial E}{\partial M}, \tag{2.6}$$

where E is the sum of all magnetic energies, including the Zeeman, exchange, dipolar, and spin-orbit energies [56]. The third (green) term in Equation 2.5 represents the Slonczewski-Berger torque or spin-transfer torque (STT) which describes a current-induced torque, which is oriented antiparallel to the Gilbert damping, resulting from the nonparallel alignment of the current polarization $\vec{P}$ with $\vec{M}$. A sufficiently large antidamping torque from this term, can overcome the natural damping and leads to the steady-state precession of $\vec{M}$ (oscillation in the ferromagnet).

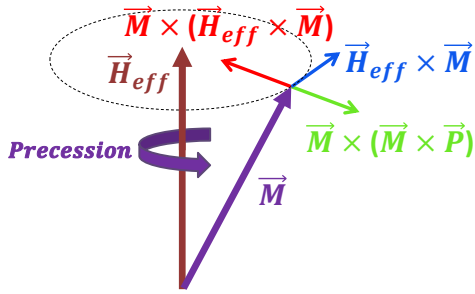

Figure 2.2: Illustration of the terms in the Landau–Lifshitz–Gilbert–Slonczewski (LLGS) equation (Equation 2.5). The first (blue) term corresponds to a circular precession around $\vec{H}_{\text{eff}}$, while the second (red) contribution describes Gilbert damping, which leads to a damped movement around the effective field direction. The third (green) term is the spin-transfer torque, which can compensate the damping by sufficiently large spin-polarized currents and causes steady-state precession.

Figure 2.3 shows the most common configuration of the magnetic film stack of a spin-torque nano-oscillator (STNO) consisting of a fixed ferromagnetic layer, a nonmagnetic spacer, and a free ferromagnetic layer. In this type of STNO, the injection of a perpendicular electrical current causes spin torque and then oscillation in the free layer.

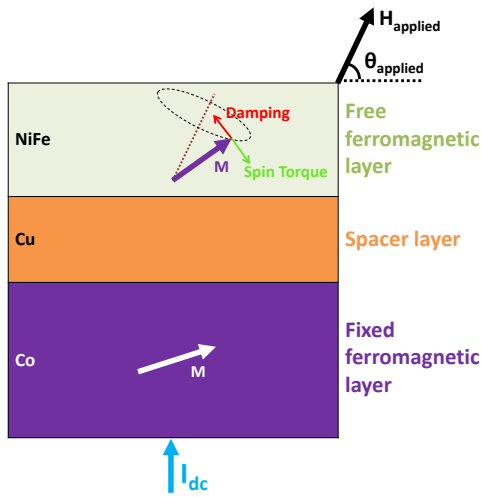

Figure 2.3: Schematic representation of a STNO (side view) consisting of a fixed ferromagnetic layer, a nonmagnetic spacer, and a free ferromagnetic layer.

2.6 Spin Hall Effect

In 1879, Edwin H. Hall discovered that a potential difference can be generated across a conductor when it carries a current subject to a transverse magnetic field [57]. This effect is called the Hall effect, and can be described as the Lorentz force acting on the moving electrons. Shortly after this discovery, he also found a similar effect in the ferromagnetic materials, nickel (Ni) and cobalt (Co). He realized that the transverse voltage depends not only on the magnetic field, but also on the magnetization direction of the ferromagnetic material. This effect is known as the anomalous Hall effect (AHE) [58]. The AHE provides direct evidence of spin-dependent forces with opposite signs to the electrons, which transforms to a charge imbalance on the sides of the conductor on account of the net spin polarization in the ferromagnetic material.

The spin Hall effect (SHE) is conceptually similar to the AHE in nonmagnetic materials. When a current passes through a nonmagnetic material in the SHE, it will not be polarized, and since there is no spin imbalance in a nonmagnetic material, the spin-dependent charge separation will not result in a measurable voltage. However, in nonmagnetic materials, the spin-dependent transverse potential difference leads to the separation of electrons of opposite polarities towards the opposite edges of the material without a charge imbalance (Figure 2.4). [59, 60, 38, 61, 62, 63] The spin Hall angle (SHA), Θ_{SH}, quantifies the conversion efficiency between charge current and pure spin current, and can be calculated based on the following [63]:

$$\Theta_{\mathrm{SH}} = \frac{\sigma^s_{xy}}{\sigma^c_{xx}} \frac{e}{\hbar}, \tag{2.7}$$

where σ^s_{xy} and σ^c_{xx} are respectively the transverse spin Hall conductivity and the longitudinal charge conductivity of the material. The SHA is usually given as a percentage, and may be either positive or negative. According to its relatively high SHA with high conductivity, platinum (Pt) is the most commonly used material for implementing the SHE. [38, 64] However, for a thin-film device with W, the SHA as high as Θ_{SH}=33 % has been reported. [65]

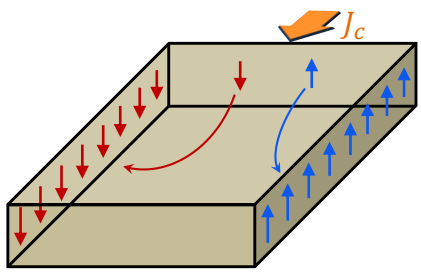

Figure 2.4: Illustration of spin Hall effect concept.

Chapter 3

Fabrication and Experimental Techniques

3.1 Device Fabrication Process

In this section, the process of fabricating the spin-torque and spin Hall nano-oscillator devices is briefly described.

Sputter deposition

Sputtering deposition is a technique of forming multilayer magnetic materials using a sputtering machine. In the present work, an AJA ATC Orion-8 is used, shown in

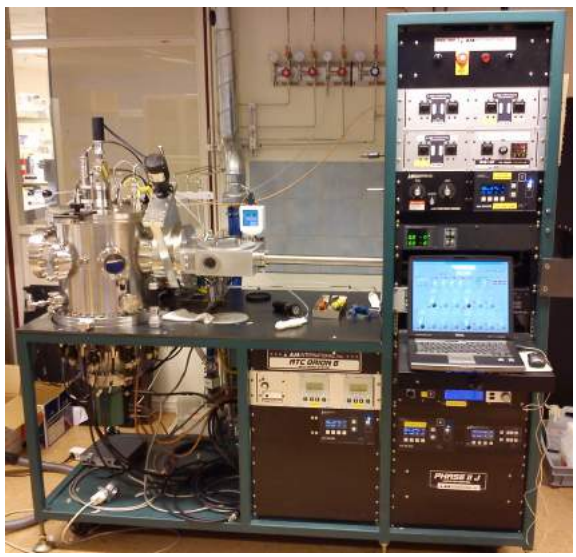

Figure 3.1: AJA Sputtering Machine at KTH.

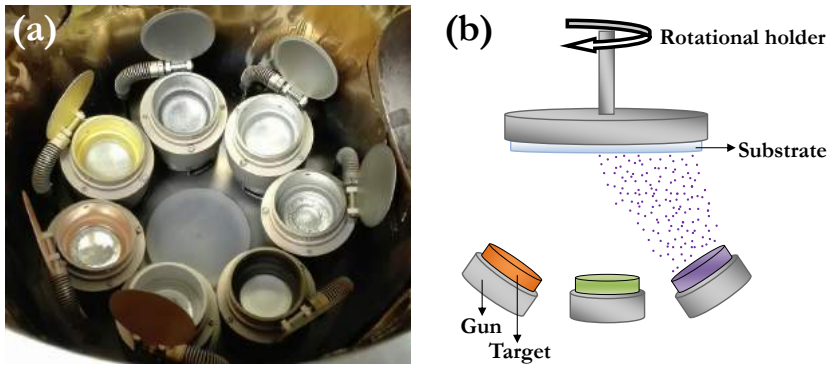

Figure 3.2: (a) Inside of the AJA sputtering machine chamber, which has seven guns that can deposit materials from seven different targets. (b) Schematic of the sputtering Process.

Figure 3.1. This machine consists of a high vacuum (HV) chamber, equipped with confocal sputtering guns arranged circularly in the bottom of the vacuum chamber (Figure 3.2(a)). As illustrated in Figure 3.2(b), the samples are mounted facing down onto the substrate holder, and to start the process a neutral gas such as argon is employed to sputter and then deposit very small pieces of the target material onto the substrate. The position of the targets and their angles, based on the distance from substrate, as well as the rotation of the substrate, can be selected to deliver a uniform thickness on a 4" wafer Si substrate or a square piece of sapphire.

To obtain good performance from the spin-torque nano-oscillator (STNO) and spin Hall nano-oscillator (SHNO) devices described in this thesis, roughness should be kept to a minimum through a carefully controlled deposition rate. This rate in turn depends on the calibration of the deposition pressure and on the applied power, which should be set optimally. The setting details of sputtering process of fabricated STNO and SHNO devices are e.g. available in Paper III [66] and Paper IX, respectively.

Magnetometry

Following the sputtering process and fabrication of the magnetic single layer or multilayer, it is important to determine the magnetic anisotropy of the sample, before the device fabrication. Since, we need to make sure that the sample stack has the expected switching mechanism and magnetization reversal of individual layers and their interactions. One way of this study is magnetometry. In this thesis, alternating-gradient magnetometer (AGM) shown in Figure 3.3, is used which is one of the most common magnetometers. This system measures hysteresis loops of magnetic structures in both in-plane and out-of-plane orientations of the applied

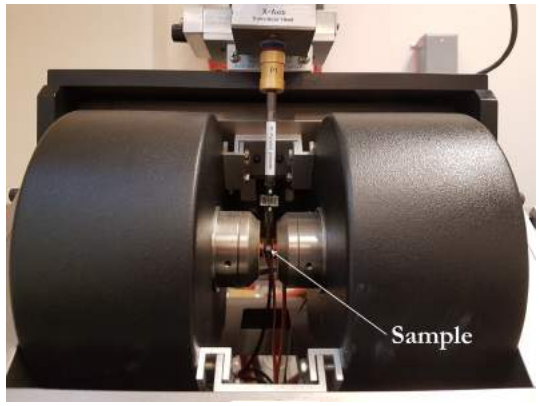

Figure 3.3: AGM measurement system at KTH with a probe holding a sample to measure hysteresis loop at the in-plane magnetic fields.

field. For each of these orientations, the AGM has its specific probes which we employ them.

Etching

Once we have a uniform wafer of a single or multiple layers of the desired magnetic properties, it is time for the fabrication process. To fabricate electronic devices, etching is commonly used to form and separate the elements.

In the process of fabrication of our devices, the following two etching techniques were employed:

1. pure argon sputter etching was used to define the device boundary and to form the active area.

2. fluorine-based reactive ion etching (RIE) steps were used to produce openings in the insulation layer.

Lithography

The final phase in the fabrication of the STNOs and SHNOs involves several lithography steps to define different microsized and nanosized features of our devices. Electronic devices such as NC-STNOs and SHNOs are fabricated using lithography. There are different scales involved in these devices, from the nanometer to the micrometer scale, and multiple lithography steps are thus necessary to produce the different parts. For example, to fabricate the NC-STNOs presented in this thesis, five lithography steps were used to fabricate high-quality devices. Depending on

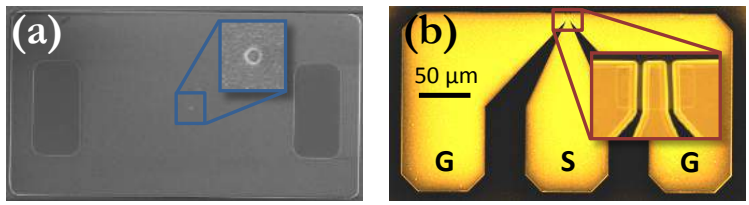

Figure 3.4: (a) SEM image of a mesa with an EBL-manufactured nanocontact and two bottom contacts etched in SiO_2. (b) SEM image of a fabricated device with GSG measurement pads.

the size of the feature, two systems were utilized. For manufacturing of resolutions below 650 nm, an XLS 7500/2145 i-line stepper was employed and for nanosized features (less than 100 nm), an electron-beam lithography (EBL) system was used (Figure 3.4(a)). After fabrication of the NC-STNOs, each wafer usually contains 28 dies, each of which has 40 rows and 9 column; each die thus has 360 devices shown in Figure 3.4(b). [67]

3.2 Measurement Techniques

3.2.1 Spin-Transfer Torque Ferromagnetic Resonance

The term *ferromagnetic resonance* (FMR) describes the collective movement (precession) of the magnetization in a ferromagnetic material in the presence of an external magnetic field. In conventional FMR measurements, a low-amplitude radio

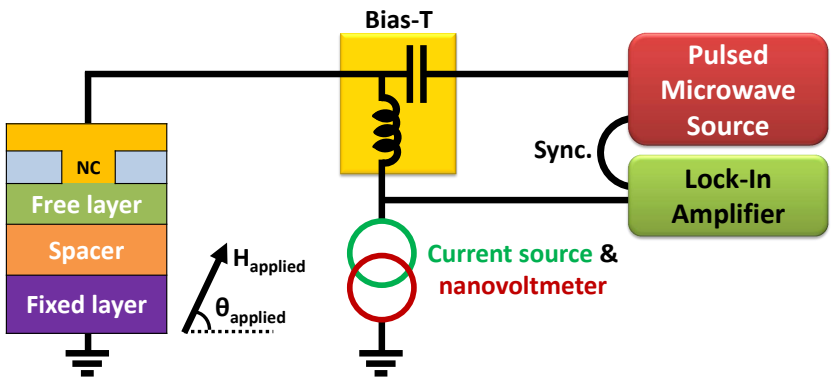

Figure 3.5: Schematic of the ST-FMR measurement set-up. The microwave source provides a pulsed output with a modulation frequency of ≈ 100 Hz, which is synchronized to the lock-in amplifier for detecting the resulting dc mixing voltage while the external field is swept. The illustrated device is a NC-STNO.

frequency (rf) field is applied to excite the oscillation of the magnetic moment in a ferromagnetic thin film under the resonance frequency condition of $f_{field} = f_{osc}$, which results in a dramatic reduction in the effective damping. However, in spin-torque FMR (ST-FMR) [68, 69, 70, 71, 72], a combination of both rf and dc currents is used to drive the excitations of the magnetic moments, causing the collective precession of the spins in the free layer of STNO and SHNO devices under an external dc magnetic field. This collective spin precession results in a time-varying resistance which, multiplied by the applied microwave current of the same frequency, generates a dc mixing voltage that can be measured using the ST-FMR measurement set-up schematically illustrated in Figure 3.5. The magnitude of the output voltage is typically small (on the order of μV), so to enhance the signal-to-noise ratio, a lock-in type measurement is used to modulate the amplitude of the microwave current.

3.2.2 Microwave and DC Measurements

The NC-STNO and SHNO devices are characterized by the electrical microwave signal generated from the spin-torque-driven precession of magnetization. The result of this precession is to create a time-varying angle between the bias current and the magnetization direction of the FM layer, leading to a rapid oscillation of the device in the GHz range. As shown in Figure 3.6, this output will be experimentally decoupled from the applied dc current and detected as an ac voltage signal using a broadband (up to 40 GHz) bias-T in the measurement circuit. Since the microwave signals generated have very low power spectral density (PSD), a low-noise amplifier (LNA) with a gain of ≥40 dB and a noise figure on the order of ≤3 dB are added

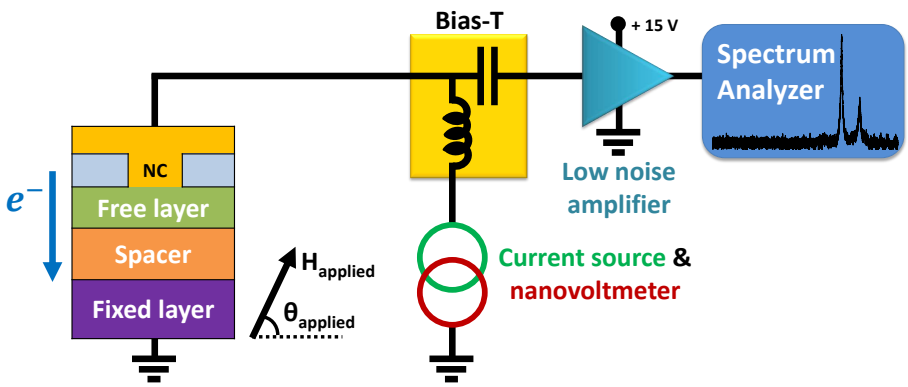

Figure 3.6: Schematic of the microwave measurement set-up for characterization of the manufactured NC-STNOs and SHNOs up to 40 GHz. The applied dc bias current results in auto-oscillation signals captured at the rf port of the bias-T and amplified by a low noise amplifier to raise their levels above the noise floor of the spectrum analyzer. The external field can be applied using an electromagnet or a permanent magnet in various in-plane and out-of-plane directions. The illustrated device is a NC-STNO.

to increase the power of the signals above the noise level of the spectrum analyzer so as to be able to detect them. The spectrum analyzer used to measure amplified signals throughout this thesis is a Rohde & Schwarz FSU-46 and FSU-67, generally operated in frequency-sweep mode with a resolution bandwidth (RBW) of 1 MHz and a video bandwidth (VBW) of 10 kHz. For the dc current source and electrical measurements (resistance), the combination of a Keithley 6221 current source and a Keithley 2182A nanovoltmeter is used with the measurement set-up. A stand-alone Keithley 2400 source meter has also been successfully employed. Furthermore, an external magnetic field with variable magnitude up to 1.8 T was applied at the desired angle.

In our actual measurement set-up, to probe our fabricated devices, we constructed a transmission line consisting of high-frequency components (Figure 3.7). In all the measurements, the positive current is defined by electrons entering the device through the ground–signal–ground (GSG) microwave probe (GGB Industries) and cables for high-frequency measurements (up to 40 GHz). Using a bias-T, direct dc current was applied only to the device, while allowing the generated microwave signal to pass through to a Miteq low-noise amplifier (gain 41 dB; bandwidth 0.1–40 GHz) for final detection using a spectrum analyzer.

For controlling the measurements, a platform in LabVIEW™ was used to set the desired values for dc current and magnetic field amplitude, as well as magnetic field angle, and to continuously run a large set of measurements automatically. This platform also stores the data systematically and has the ability to subtract background noise from the obtained spectra. To characterize the spectra acquired in the frequency domain, a dedicated MATLAB program postprocessed the data.

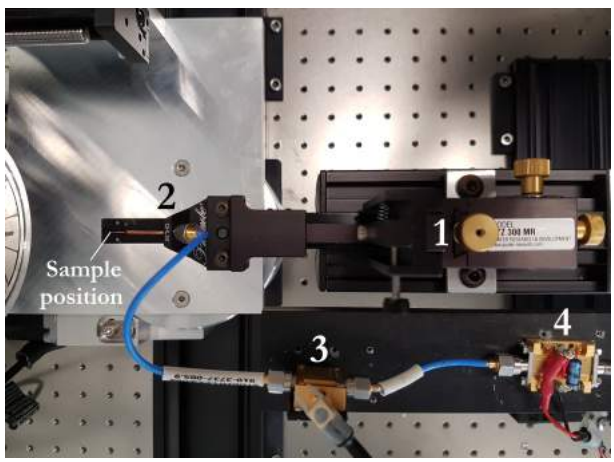

Figure 3.7: Transmission line for microwave measurements consists of 1) micromanipulator, 2) GSG microwave probe, 3) bias-T, and 4) low noise amplifier.

The data was first corrected for amplifier gain and for losses from the impedance mismatch of the fixed 50 Ω in the measurement transmission line, associated with the variation in device resistance. The properties of the auto-oscillation that occur in the spectra were extracted by fitting the data with a symmetric Lorentzian function to collect the linewidths and the integrated output powers.

3.3 Developed Measurement and Characterization Systems

After fabrication, all the nanodevices are characterized by their electrical and microwave responses in the presence of an external magnetic field under application of dc or rf currents. Here, two newly developed autonomous measurement systems are introduced; one is capable of full 3D control of the direction of the external magnetic field (See Paper I) [73]. The general techniques for characterizing devices using these systems, as well as a new method of probing an operational nanodevice using magnetic force microscopy (MFM) (See Paper II), will now be presented.

Since anisotropic magnetic materials and the spin-torque effect are angle-dependent, in studying magnetic films and devices for room-temperature applications, it is essential to use a probe station equipped with high-frequency tools capable of altering the magnetic field's direction with respect to the sample plane, so that theoretical results may be validated. We here demonstrate two newly developed microwave probe stations with motorized rotary stages for adjusting the magnitude and angle of the applied magnetic field. In the first system, the magnetic field is provided by an electromagnet and can be adjusted from 0 to ~ 1.4 T, while the polar angle (θ) with respect to the sample plane can be varied from 0° to 360°. In the second system, the magnetic field is provided by a Halbach array permanent magnet which can be rotated and translated to cover the full range of polar (θ) and azimuthal (φ) angles (field angle within the sample plane) with a tunable magnitude of up to ~ 1 T. Both systems are equipped with microwave probes and high-frequency instruments to allow for microwave characterization up to 40 GHz. Software programs also are developed to automatically perform continuous large sets of electrical and microwave measurements.

Unfortunately, only a few probe stations with rotational fields are commercially available. To rotate the magnetic field, either the magnet or the sample may be rotated. Typically in homemade stations, the field is positioned at different angles by rotating the sample [74]; however, this is inevitably accompanied by vibrations that negatively affect measurement performance and signal stability, by the device to be measured being damaged by the probe, or by connectivity between the device and the probe contact wedge being lost. Moreover, because of the manual mounting of the probe and centering of the samples, the results may not be reproducible with respect to the magnetic field angle after remounting, recentring, and repeating measurements. Even in probe stations with a rotational field, such as a projected field electromagnet (for example, from GMW Associates) [75] or a homemade vector

magnet [76] the field uniformity is poor and the field magnitude is usually limited to a few kOe. Such probe stations typically use a complex and expensive PID controller to apply the variable magnetic field. Further, since angular field dependence of magnetic films and devices is expected, it would be useful to have a system that can automatically adjust the desired range of the angle and magnitude of the field in order to fully characterize the sample; however, this capability is not commonly available.

To overcome these problems and allow the addition of new capabilities, we have designed new systems to rotate an electromagnet and a permanent magnet, instead of the sample. In commonly used high-field measurement systems [77], when out-of-plane fields are to be applied, the sample holder is generally positioned horizontally between the poles of an electromagnet to allow the sample to be placed on the holder. In order to adjust the field angle, the sample holder is then rotated with a controllable stepper motor around the horizontal axis, leading to the problems mentioned above. To avoid such problems and have the sample in a fixed position, the magnet should be rotated. However, due to the size and weight of high-field electromagnets, it is necessary to employ an efficient design. Here we demonstrate autonomous microwave probe stations with a rotary stage that adjust the magnitude and angle of the magnetic field by rotating the electromagnet. In this system, the magnetic field from the electromagnet can be adjusted using the output voltage from a power supply and the gap size between the poles from 0 to ~ 1.4 T, using which the full 360° out-of-plane rotation with respect to the sample plane (θ) from 0° to 360° is achievable. Moreover, in characterizing devices, it is valuable to have the freedom to apply the magnetic field in any direction. To this end, a system with full motion control has been designed and built; this applies the magnetic field in three-dimensional space (polar angle) relative to the sample plane. This novel system has been designed to orient the direction of the magnetic field using a permanent Halbach array of magnets. This system is not only capable of covering the pure polar (θ) and azimuthal (φ) angles both from 0° to 360° independently, but can also cover the full range of angles in three-dimensional space (all combinations of θ and φ) with a tunable magnetic field up to ~ 1 T. Furthermore, the homemade nonmagnetic sample holders in both systems are equipped with microwave probe and cables and use high-frequency instruments, allowing the operational frequencies of the sample to be studied up to 40 GHz. Also, the specially designed software programs can automatically run these apparatuses based on a user-defined range of magnitudes and angles of the magnetic field, thus avoiding time-consuming and unreliable experiments. In addition, some of the experimental results presented in this thesis show the capability of these autonomous systems. For example, spin-transfer torque ferromagnetic resonance (ST-FMR) measurement of nanocontact spin-torque nano-oscillators (NC-STNO), and study of angular field dependence of high-frequency responses in NC-STNOs, as well as the angular dependence of anisotropic magnetoresistance (AMR) in a nanogap spin-Hall nano-oscillator (SHNO). The following sections explain all the steps employed in the modeling,

optimization, and production of these autonomous systems and sample tests which also were presented in Paper I [73].

3.3.1 Field Rotational Microwave Probe Station

The proposed high-frequency (up to 40 GHz) measurement system has been designed based on the rotation of an electromagnet that applies a large magnetic field (up to ~ 1.4 T). In this system, where the probe position does not move and the sample is centered in a reproducible manner, the precise angles needed for measurement and reproducible sample centering can be obtained. Furthermore, since the field and not the sample rotates, there is less vibration. This system can improve measurement performance to obtain high-frequency responses from magnetic films and devices with high accuracy. It is clearly not reasonable to rotate such a large electromagnet around the horizontal axis (X axis). Instead, the optimum approach is to mount the sample holder along the vertical axis (Z axis) and then to rotate the magnet around the Z axis (Figure 3.8). In the field rotational probe station, in order to rotate the electromagnet, a stepper motor was used to apply uniform out-of-plane magnetic fields at any angle relative to sample plane (θ). To apply the magnetic field at angles in three-dimensional space, the desired φ angle (the in-plane angle with respect to the flowing current direction) can be adjusted by misaligning the contact pads of the device with respect to the probe. Based on the design of the fabricated devices tested using this probe station, φ can vary from −30° to 30° (in total 60°). The contact pads could also be designed so as to allow coverage of the full range of φ. All components were mounted on a heavy optical table so that measurements could be performed without transferring even small vibrations to the sample.

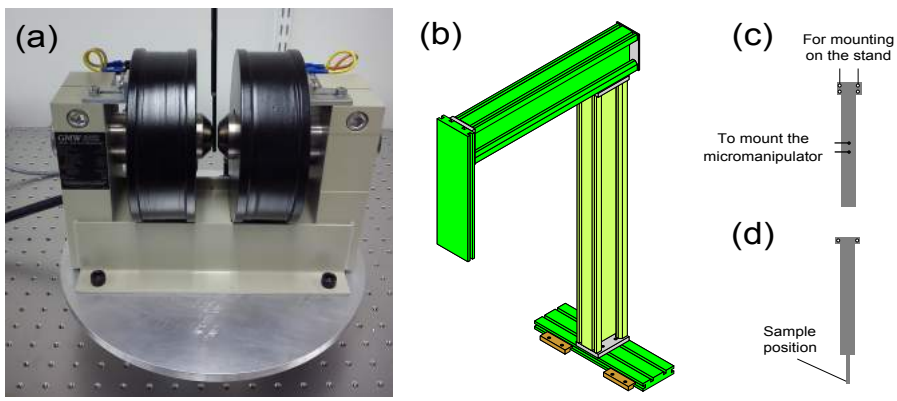

Figure 3.8: (a) Rotary stage with mounted electromagnet. Schematics of (b) adjustable stand for sample holder, (c) holder for micromanipulator, and (d) sample holder for the field rotational measurement system.

The electromagnet rotary stage

We designed and built a rotary stage for the electromagnet using a B4872TS rotary table from Velmex mounted on an optical table. A thick circular aluminum plate was then attached to the table as a holder for the electromagnet. Finally, a 3470 c-frame electromagnet from GMW Associates, with reversible plane cylindrical 40 mm and tapered 20 mm face diameter poles, was mounted on top of the holder [78]. The gap between the poles in the electromagnet can be adjusted from 0 to 75 mm with a good field uniformity which detailed information is available on Reference [79]. The assembled rotational electromagnet is illustrated in Figure 3.8(a). We also purchased a BOP50-8ML power supply from KEPCO with maximum 8 A input current and a stability of 0.02% over eight hours, equipped with water tubes to cool the electromagnet. In this configuration, the stage can orient the magnetic field with an accuracy of 0.02°.

Sample holder stage

Since it is difficult to position the sample on the sample holder while it is in the vertical position, we designed a flexible sample holder that could be displaced into the horizontal position to allow the sample to be affixed before being returned to the vertical position between the poles of the electromagnet. However, such a design is difficult, since the microwave probe is located very close to the sample location, and it is necessary to avoid moving it. Besides, it is also important to locate the sample centrally between the two poles. After sketching different possibilities, we modeled the sample holder in the following way:

(a) The stand of the sample holder (Figure 3.8(b)) uses I-Beam BiSlide bases and T-Slot plates from Velmex. This stand is manually controllable in the X, Y, and Z directions so that the sample can be positioned in the center between the poles of the electromagnet.

(b) The end of the holder, which should be made of a nonmagnetic material, consists of two parts mounted vertically on the stand using nuts and screws. In the upper part (Figure 3.8(c)), we assembled a nonmagnetic XYZ micromanipulator (Quater Research and Development) for the microwave probe on an aluminum plate, which has a travel distance of 0.762 cm along each axis with a resolution of 635 μm per turn continuous. The lower plate (Figure 3.8(d)) can be easily displaced by using plastic-head thumb screws. This plate can thus be replaced, allowing the sample to be attached using double-sided tape at its 8 mm end. It can then be mounted in the fixed position by two screws.

For the rf measurements of nanoscale devices, we used a customized nonmagnetic GSG microwave probe with an extended arm from GGB Industries, as well as cables suitable for high-frequency measurement. A microscope was also needed to precisely

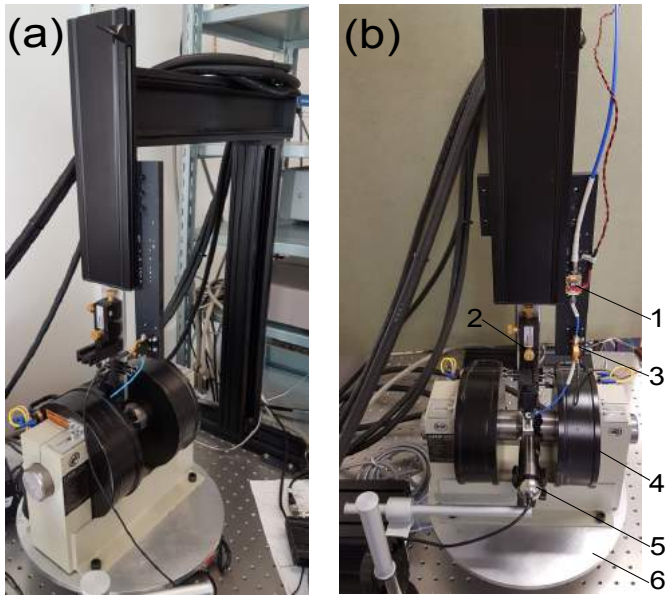

Figure 3.9: (a) Finished field rotational microwave probe station. (b) Final field rotational microwave probe station consists of 1) amplifier, 2) micromanipulator, 3) bias-T, 4) electromagnet, 5) microscope camera, and 6) circular aluminum plate which has been mounted on top of the stepper motor.

define the contact between the microwave probe and the sample. For the vision part of the sample holder, we employed a Dino-Lite AD7013MZT digital handheld microscope camera with a 5 megapixel sensor and an adjustable polarizer with up to 240x magnification on a fine-focus adjustment stand. The final field rotational microwave probe station is illustrated in Figure 3.9.

Autonomous control of measurements

To perform measurements with this field rotational measurement system, user-friendly controller software is a necessity. In this system, all of the measurement instruments are controllable using customized programs in LabVIEW™ (National Instruments) with defined connections to the controller hardware. To be able to control the rotary system in LabVIEW, controller hardware compatible with the software is needed. We used a VXM™ controller system from Velmex, which can be programmed by LabVIEW to drive the Velmex rotary table. Using the controller's command sheet, we executed a subprogram in LabVIEW to govern the angle of the magnetic field from the electromagnet by adjusting the angle of the rotary table. To control the output magnetic field of the electromagnet, we employed a control

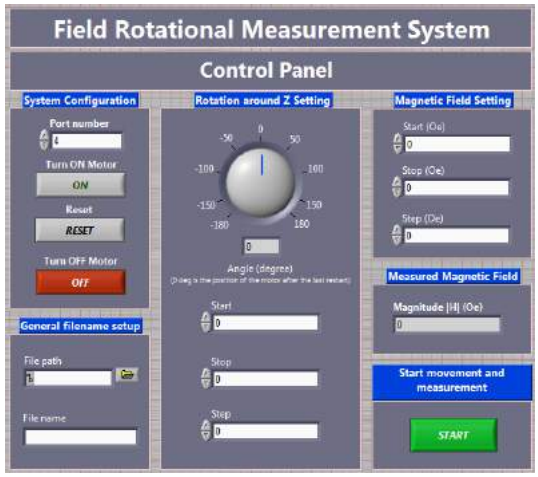

Figure 3.10: Developed control panel of the autonomous field rotational microwave probe station.

program in LabVIEW, rather than a PID controller. We attached a transverse Hall sensor from Lake Shore Cryotronics to one of the poles of the electromagnet. We then used its output voltage as feedback to calculate the actual magnetic field, and thus controlled the output of the power supply. Finally, using the main control panel in LabVIEW, it is possible to set the desired starting angle (magnitude) and the steps by which the angle (magnitude) should change to reach the final angle (magnitude) of the magnetic field in a stepwise manner (Figure 3.10). In this way, the whole of the measurement process is automatically controlled by the program and the data extracted from each step of the measurement is immediately stored.

3.3.2 Full 3D Field Microwave Probe Station

In characterizing nanoscale magnetic samples, it is valuable to have the freedom to apply the magnetic field in any direction, since the effect of spin-torque is angle-dependent. Our aim was thus to design a novel microwave probe station to give better angular control of the magnetic field. On the other hand, it would be worth applying a high magnetic field at 3D angles relative to the sample plane using a rotatable or tiltable system. Low-field 3D fields are routinely applied using Helmholtz coils [80], but 3D control of 1 T fields is entirely different. Magnets capable of producing magnetic fields in three dimensions have been proposed [81, 82]. For example, Lawrence Berkeley National Laboratory, USA possesses an operational 0.9 T octupole magnet with complete 3D freedom [83]. However, this kind of magnet is relatively expensive in terms of manufacturing cost, development time, and power consumption.

We designed and built a compact system with full motion control and the capability of applying high magnetic fields (up to ~ 1 T) at desired polar angles relative to the sample plane. The proposed high-frequency (up to 40 GHz) measurement system has been designed based on permanent magnets in a Halbach array (Figure 3.11(b)). This magnet is a magnetized cylinder that consists of a special arrangement of permanent magnets that exerts an intense magnetic field (in our magnet, ~ 1 T) confined almost entirely within the cylinder.

This autonomous system offers full automatic control of the horizontal (X axis) and vertical (Z axis) translation of the magnet to alter the magnitude of the magnetic field, as well as its rotation around these axes (θ and φ). In addition, it offers real-time 3D magnetic field measurement as close as possible to the sample location where the controlled magnetic field is applied.

In this system, the sample is mounted at the center of a fixed holder tip so that the sample centering is reproducible and so that the precise angle of the magnetic field can be achieved by rotating the magnet. Also, as only the magnet rotates to change the angle of the field, no destructive vibrations will be transferred to the sample. This system can thus improve measurement performance in the characterization of high-frequency responses of magnetic films and devices by applying 3D fields with high accuracy.

Full 3D rotary stage of permanent magnet

The rotary stage of this system has been designed with full motion control so that the magnet applies magnetic fields—both pure in-plane and out-of-plane independently, as well as through polar angles—of up to ~ 1 Tesla relative to the sample plane. The schematic of the rotary stage of this system is shown in Figure 3.11(a). This stage has the following motion capabilities and uses the described Velmex components:

- Motorized rotation around Z (φ): B4872TS rotary table (RT1); the other parts of the stage have been mounted on RT1 using an L-shape aluminum plate.
- Motorized translation along Y: XN10 XSlide motorized linear stage with a travel distance of 4 inches (XS1).
- Motorized translation along Z: XN10 XSlide motorized linear stage with a travel distance of 2 inches (XS2).
- Manual translation along X: XGST XSlide Gusset with a travel distance of 2 inches.
- Motorized rotation around Y (θ): B5990TS rotary table (RT2).

The final system is assembled in the following two configurations:

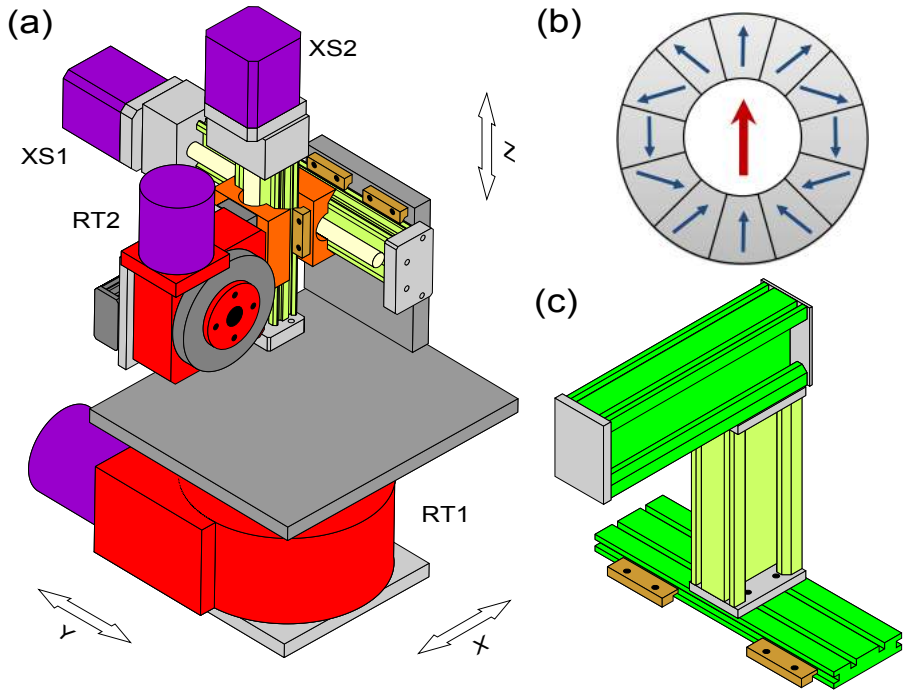

Figure 3.11: Schematics of (a) the motorized stage of the autonomous 3D field rotational microwave probe station, (b) the cylindrical Halbach array of permanent magnets, and (c) the adjustable stand for the sample holder.

(a) Config1: In this configuration (Figure 3.12(a)), the RT1 is mounted on a horizontal stage fixed to the optical table. The system can then apply a maximum magnetic field of 0.95 T over the full range of out-of-plane angles of θ from 0° to 360° and φ from −24° to 24°, and from −156° to 156° (total range 96°). The limited range of φ is due to the small size of the opening in the Halbach array; for larger angles, the magnet would contact the sample holder. However, for lower magnetic fields, such as 0.5 T, where the magnet would be slightly too far from the sample when moving the magnet using XS1, we can cover 300° of φ. Further, if it is necessary to employ the full range of 360°, this can be done by rotating the sample.

(b) Config2: In the second configuration (Figure 3.12(b)), RT1 is mounted on a vertical stage, and the system can thus apply a maximum magnetic field of 0.75 T at a full in-plane angle of φ from 0° to 360° and of θ from -180° to 130° (total range 310°).

With these two configurations, we can access combinations of θ and φ that provide

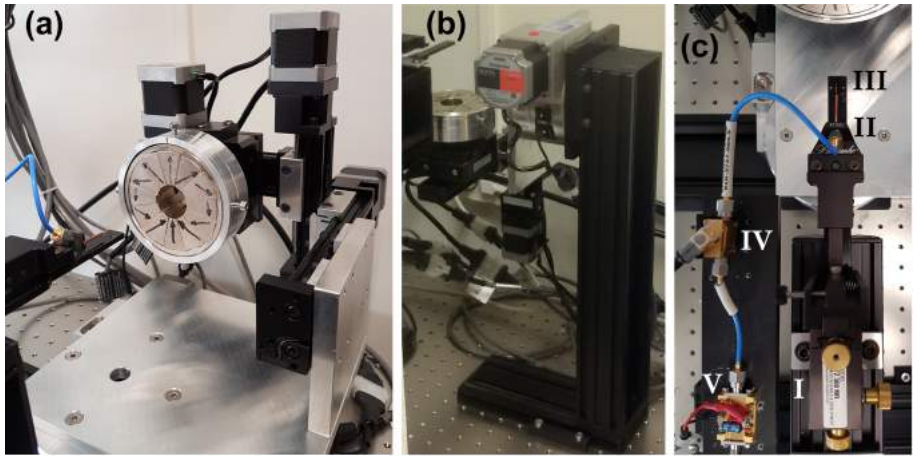

Figure 3.12: Final autonomous 3D field rotational probe station based on (a) Config1 and (b) Config2, as explained in the text; (c) top view of sample holder consists of I: micromanipulator, II: microwave probe, III: sample position where the Senis Hall sensor located on its bottom, IV: bias-T, and V: amplifier for high-frequency measurements.

full three-dimensional control over the polar angles of the magnetic field relative to the sample plane with an accuracy of 0.02° (0.07 mm), and with repeatability of 0.0002° (0.002 mm) for each rotary (transnational) stepper motor.

Sample holder stage

Figure 3.11(c) shows the adjustable stand for the sample holder; this uses I-Beam BiSlide bases and a T-Slot plate from Velmex and can be manually controlled in the X and Y directions. As shown in Figure 3.12(c), this is almost the same sample holder as in the case of the field rotational system, with a micromanipulator (Quater Research and Development) and microwave probe (GGB), but also we have a Senis F3A three-axis magnetic field transducer [84] located 0.5 mm under the sample position inside an 11-mm-wide nonmagnetic holder from GMW [85]; this measures the elements of the magnetic field in order to determine the real magnitude and angle of the magnetic field. The holder is mounted on top of the stand using clamps, nuts, and screws so the sample can be located precisely on top of the center of the Hall sensor and, for accuracy, we consider the gap between the sensor and sample in our calculations. In order to achieve accurate magnetic field angles θ and φ, it is important to have the sensor and sample exactly on top of the center of RT1 along the Z axis, which can be achieved by calibrating the system based on the elements of magnetic field measured using the 3D transducer.

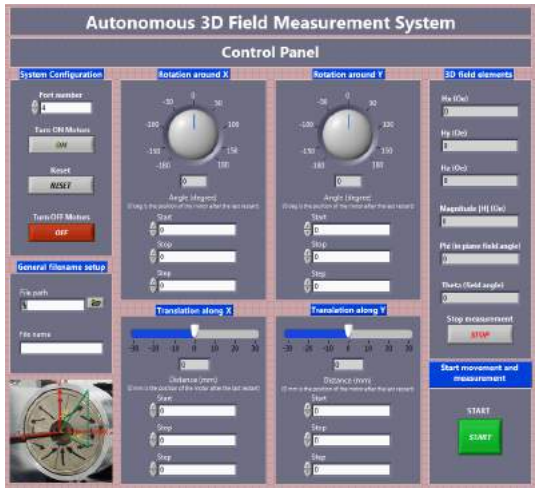

Figure 3.13: Control panel of the autonomous 3D field rotational microwave probe station.

Autonomous control of the measurements

As mentioned, all the measurement instruments can be controlled using customized subprograms in LabVIEW™. For convenient measurements with this 3D field measurement system, it is thus also necessary to control it in LabVIEW. As with the field rotational probe station, we used a Velmex VXM™ controller. To control the motion along multiple axes using four stepper motors, we purchased two sets of integrated VXM controllers, each to control two motors. Using the controller's command sheet, we designed a control panel in LabVIEW to give full control over the motorized translation and rotation in four directions and to automatically carry out sets of measurements, which can be defined in the control panel (Figure 3.13). In addition, this program uses readings from the Senis Hall sensor to calculate and display the 3D elements of the magnetic field; this data is stored in a file. The detailed procedure for using this control panel will be explained in the next section.

Magnetic field characterization

To demonstrate the performance of our system, we have characterized a sample magnetic field range that can be controlled and applied to nanodevices. To determine the direction of the field on the sample, the real-time 3D magnetic field measurement needs to be as close as possible to the sample position. For this purpose, we used a Senis F3A three-axis magnetic field transducer. This has a fully integrated CMOS three-axis (B_x, B_y, B_z) Hall probe with very high spatial resolution and high angular accuracy (the orthogonality error is less than 0.1°) [84]. The coordinate system of the probe station is shown in the inset to Figure 3.14(a). In line with the definition

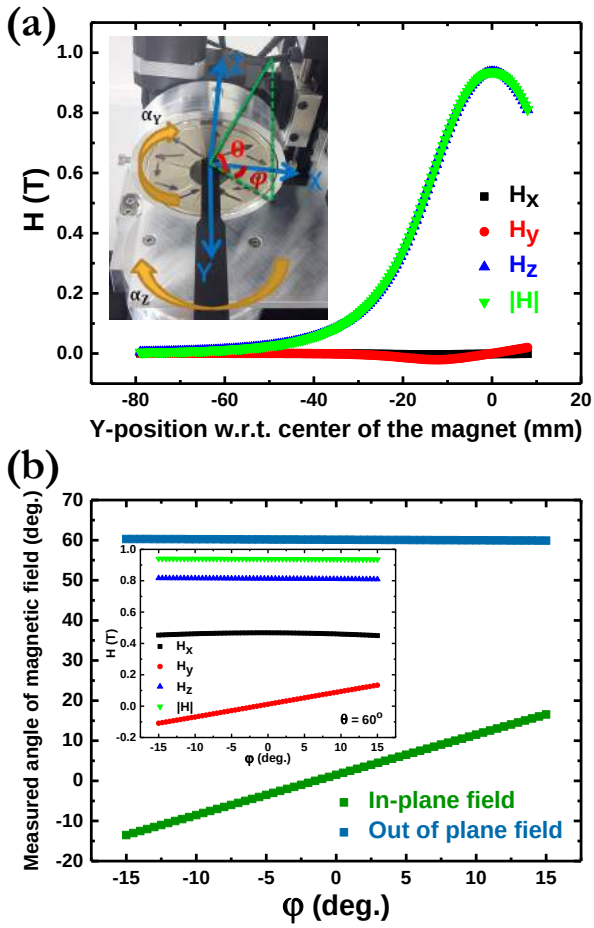

Figure 3.14: Mapping with 3D Hall elements while the magnet (a) translates along the Y axis (the inset shows the axes and angles) and (b) rotates with $\theta = 60°$ and φ from −15 to 15 at Y = 0 (the inset shows the measured x, y, and z elements of the magnetic field).

of the X, Y, and Z axes, θ is the polar angle between the magnetic field direction and the position of the sample plane (XY plane) in an out-of-plane rotation, while φ corresponds to the angle between the magnetic field direction and the X axis in an in-plane rotation (or in-plane angle with respect to the flowing current direction).

Figure 3.14 illustrates the mapping of the 3D Hall elements based on the coordinate system. Figure 3.14(a) shows the result when the magnet translates along the Y axis, while Figure 3.14(b) shows it rotating with $\theta = 60°$ and φ from $-15°$ to $15°$ at Y = 0, where the maximum field is obtained from the magnet. The

inset shows the detailed x, y, and z elements of the magnetic field. To achieve these results, we simply set the start and stop points (angles) with preferred steps for translation along (rotation around) each axis in our LabVIEW program, and the system automatically performs the characterizations.

To conclude, we developed and built two compact automatic measurement systems capable of adjusting the magnetic field orientation with high accuracy in order to characterize nanomagnetic devices. These systems are cost-effective and have user-friendly designs for both the hardware and software in comparison with commercially available systems with similar functions. The sample holders in both systems are in fixed positions, which is crucial for the accuracy, signal stability, and reproducibility of measurements. The magnets instead rotate to change the magnetic field angle with respect to the sample plane. By rotating the electromagnet, the field rotational probe station can cover the full range of θ from 0° to 360°; by manually rotating the sample, a limited range of φ can also be covered. Also, the 3D field probe station (using two different configurations) can orient the field over the full range of the combined θ and φ. Further, in both systems, the magnitude of the magnetic field is also adjustable based on specifications of the magnets, and large classes of measurement conditions can be defined in the control panel software for automatic execution. We can now be more confident about the results of our measurements. The design and production of a system with the ability to apply a 3D field relative to the sample plane (or flowing current direction) represents a breakthrough in 3D high-field measurement systems. To demonstrate the ability and performance of these autonomous systems, in our first tests, we employed dc and rf techniques to measure two types of spintronic devices. The NC-STNO was characterized using the ST-FMR method (Section 4.2), and we also studied the dependence of this device's microwave response on the direction of the external magnetic field (Section 4.5). Further, we measured the AMR curves of a nanogap SHNO (Section 5.1). In addition, both the field rotational probe station [72, 86] and the 3D field probe stations [87, 66] have been employed in some of our published studies. We expect these probe stations will help us to determine new effects, concepts, and phenomena in nanomagnetic and spintronic devices.

3.3.3 Magnetic Force Microscopy of Operational Nanodevices

We have fabricated a range of STNOs and SHNOs with different characteristics. Our rf measurements show the expected auto-oscillations outputs from our devices; however, for real applications, maps of these devices in the operational state would be useful. We present here a new method of probing the spatial profile of an operational device using magnetic force microscopy (MFM). We used a very high resolution MFM system with extremely sharp MFM tips [88] to observe operational nanomagnetic devices.

Figure 3.15 shows our MFM system, a MFP-3D-SA [89] from Asylum Research (an Oxford Instruments company), which we developed by adding a microwave probe station to allow electrical and microwave access to the devices. Due to space limitations, especially between the MFM head and the sample for scanning, it is difficult to gain electrical access to the device and to design a stable connection for transferring the microwave signals generated from the devices to the spectrum analyzer for measurement.

We first designed and built a holder for the XYZ micromanipulator and mounted it on the L-shape slider of the MFM stage. We then connected a GR-style nonmagnetic microwave probe from GGB to the micro-manipulator. Figure 3.16 shows a customized version of this probe with an extended co-ax to reach the waveguides

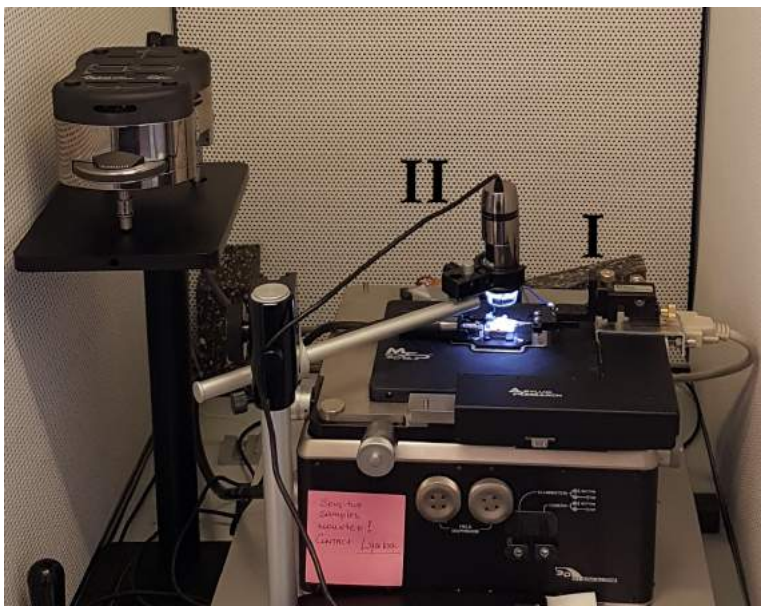

Figure 3.15: MFM set-up with mounted I: microwave probe station and II: microscope camera.

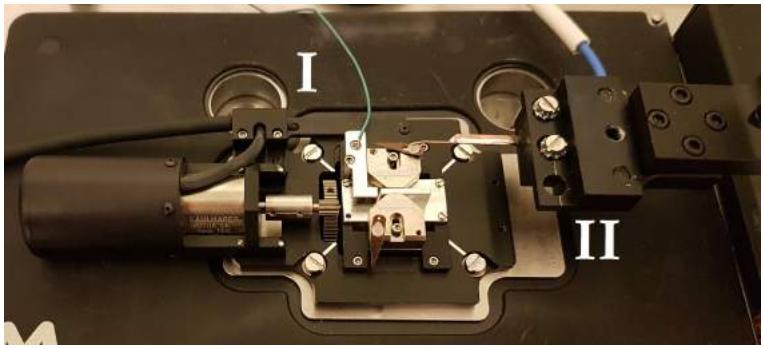

Figure 3.16: MFM stage with I: variable field module 2 (VFM2) and II: microwave probe connected to the micro-manipulator.

of the device that we want to measure and scan it simultaneously. In the design of this probe, we aimed for minimum thickness and height so that the probe and its rf cable connection port would fit in the limited space under the head of the MFM, without making contact or interrupting the scanning process. Outside of this limited region, we then connected the transmission line for the microwave measurements, as described in Section 3.2.2.

Since we are using MFM and our samples have dependencies on the applied magnetic field, we added a variable field module 2 (VFM2) [90] to the stage (Figure 3.16); this extra accessory is compatible with the system and can be purchased separately. The VFM2 uses permanent magnets to avoid heating and associated drift, and can apply in-plane magnetic fields of more than ±0.8 Tesla (8000 G) at a field resolution of ≈1 G. The sample is mounted on top of this module, between the poles, in order to fall within the in-plane field. For the vision part, we used the same microscope camera described in the previous section (Figure 3.15). For the MFM process, we fabricated a customized high-resolution MFM probe as described in Reference [88]. Section 5.5 will present the experimental results of carrying out MFM on nanoconstriction-based SHNOs. The detailed results were presented in Paper II.

Chapter 4

Spin-Torque Nano-Oscillators

Spin-torque nano-oscillators [30] (STNO) are nanoscale electrical devices with broad current and field tunability and the ability to generate microwave signals at GHz frequencies. In STNOs, spin-transfer torque (STT) [35, 36, 37] from a direct spin-polarized current drives and controls the auto-oscillation of the local free layer magnetization which, through its oscillating magnetoresistance, transforms the direct input current to a tunable microwave voltage in the output. These devices are highly promising for applications in next generation of wideband microwave frequency generators, multifunctional microwave components, and ultrafast microwave sensors for the telecommunications, aerospace, and medical equipment industries. Their advantages include compatibility with semiconductor technology [5, 19, 21, 32], large frequency tuning ranges [91, 87, 56, 92], and very high modulation rates [93, 94, 95, 96, 97, 98, 99]. Nanocontact (NC) STNOs [27, 29, 100] have the additional advantage that they can generate a wide range of highly nonlinear localized and propagating spin-wave modes [101, 102, 103, 104, 105, 106, 107, 108, 109] for use in magnonics [41, 110, 111].

Depending on geometry, material properties, and experimental conditions, different kinds of magnetization dynamics can be derived in STNO devices [112, 91, 106]. In addition, to reach high levels of spin-transfer torque, it is important to determine the relationship between the key design parameters and the threshold current [113, 114, 115, 116], linewidth [114, 117, 118, 119, 107, 109], spin-transfer torque efficiency [35, 115, 120, 121], roughness [114], and microwave power [122, 116]. To fulfill the requirements for practical applications, we need to optimize linewidth and output power of the STNOs with lower operational currents.

In this chapter, the first remarkable improvements in the performance and applicability of spin-torque nano-oscillators will be described with the support of experimental results and simulations [66]. I will describe the auto-oscillation dynamic properties of NC-STNOs built from a conventional spin-valve stack, but with thicker Cu bottom electrodes. This means demonstrating auto-oscillations with higher frequencies at lower threshold currents, and at higher output powers. Then, using

ST-FMR studies and numerical simulations, I show that the use of a thicker copper layer in the bottom electrode helps to tune spin-wave resonance using lateral current spread in these NC-STNO devices. In the next section, with help of numerical simulations, I will show a reduction in Joule heating with a consequent improvement in microwave output stability, achieved by increasing the Cu thickness of the bottom layer. Using an NC-STNO device, I describe the derived dependency of the device's output on the angle of external magnetic field by experimental high frequency characterization. In addition, I present observations of droplet dynamics [106] in NC-STNOs at oblique magnetic fields using micromagnetic simulations. At the end of this chapter, I demonstrate ultra-high frequency tunability at low threshold currents in STNOs based on perpendicular magnetic tunnel junctions (p-MTJs).

4.1 Improvement of NC-STNO Performance

The extended layout in NC-STNOs, in contrast to nanopillar STNOs, allows for spin-wave (SW) propagation and interaction over large distances. However, NC-STNOs are limited in how well the spin-polarized current can be focused into the auto-oscillating region under the NC. The perpendicular component of the current density generates useful interlayer STT at the free layer, but the extended layout and the low resistance of the GMR spacer compared to the two free and fixed ferromagnetic layers, lead to a substantial lateral current spread and a lower perpendicular current density. This leads to a loss of STT, and thus an unnecessary increase in the auto-oscillating threshold current. There are a few different possibilities for reducing this current spread, such as reducing the GMR spacer thickness. However, it has been shown that a thinner Cu spacer rapidly increases the interlayer coupling, which reduces the magnetoresistance [123] and also increases damping [124]. Here we have instead studied the impact of increasing the Cu underlayer thickness (t_{Cu}) of NC-STNOs on both the auto-oscillation threshold current (I_c) and the general microwave signal properties. This impact has been studied more extensively in [66] (Paper III), and the materials and data in this section and appended paper are reproduced with the permission of the Royal Society of Chemistry.

We showed that increasing the thickness of the bottom Cu electrode forces more of the current to flow perpendicularly through the ferromagnetic layers, down to the low resistance bottom electrode, before spreading out laterally. We fabricated a large set of differently sized NC-STNOs with bottom Cu electrodes ranging from 10 to 70 nm, and investigated their static and microwave properties. Using numerical simulations, we predicted a ~50% increase in the perpendicular current density at the ferromagnetic layers as the Cu bottom electrode thickness increases from 10 to 70 nm; this could potentially reduce the threshold current (I_c) by ~30%. In our experiments, an increase in t_{Cu} from 10 to 70 nm led to a reduction in threshold current by as much as 40%. In addition, we found that a thicker bottom electrode increases the microwave output power by an order of magnitude, which further demonstrates that NC-STNO performance can be greatly improved by increasing

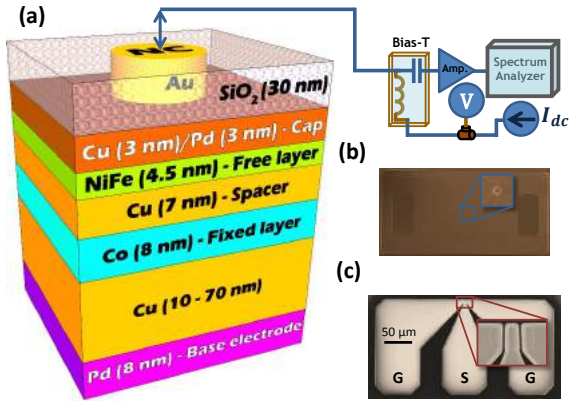

Figure 4.1: (a) Schematics of the device structure and the transmission line for electrical and microwave measurements. (b) Scanning electron microscopy image of the NC with d_{NC}=200nm. (c) Optical microscopy image of the final device and the top contact coplanar waveguides which provide electrical access to the NC.

the thickness and sheet conductance of the bottom electrode.

The samples are single NC-STNOs [125, 126, 56, 127, 128, 129] with the following layer structures: Substrate/Pd(8)/Cu(t_{Cu})/Co(8)/Cu(7)/NiFe(4.5)/Cu(3)/Pd(3) (all thicknesses given in nm) where t_{Cu} = 0, 10, 30, 50, 70 nm and the nominal NC diameters are d_{NC} = 60, 80, 100, 120, 130, 150, 170, 200, 250, 300, 350, 400, 500 nm; the bottom Co layer is the fixed layer and the top NiFe layer is the free layer. The schematic of the device structure and the transmission line for dc and microwave characterization of the STNOs used in the present work are shown in Figure 4.1.

Due to natural variation in the NC-STNO fabrication process, there is generally a difference between the nominal and actual size of the NC. We can obtain the actual NC size, as well as the total NC-STNO resistance (R), from the Sharvin–Maxwell (SM) equation [130, 131]. In this method the relationship between R and the nominal size of the NC is defined by

$$R = \frac{a}{(d_{\mathrm{NC}} + \delta)^2} + R_{\mathrm{mesa}}(t_{\mathrm{Cu}}), \tag{4.1}$$

where a is a coefficient and δ is a constant offset from the nominal NC diameter, both independent of d_{NC} and t_{Cu}, and R_{mesa} is the resistance of the two half-mesas in parallel (Figure 4.2(a)), which depends on the bottom Cu layer thickness. Figure 4.2(b) shows the average resistance of nine identical measured NC-STNOs (R) versus d_{NC}, together with fits based on Equation 4.1. Since all of the NC-STNOs had a similar fabrication process, it is more reasonable to find the fitting parameter δ by applying the fitting function to all the data. From the fits, we find δ = -1.9

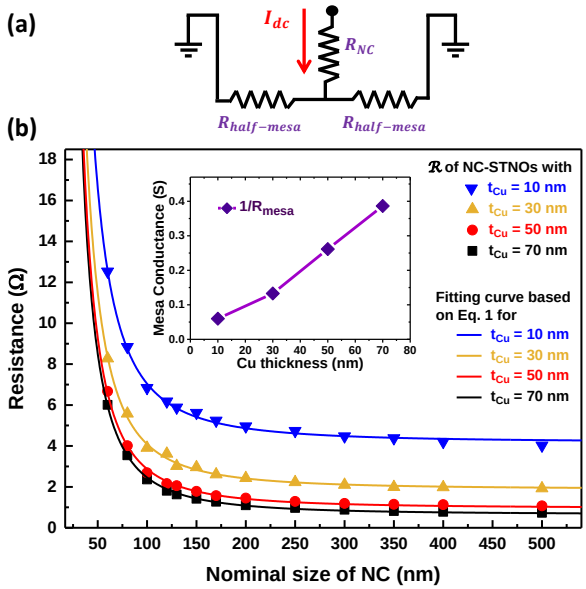

Figure 4.2: (a) General electrical structure of the NC-STNO devices, (b) their resistances for t_{Cu}= 10, 30, 50, and 70 nm, and d_{NC}= 60, 80,100, 120, 130, 150, 170, 200, 250, 300, 350, 400 and 500 nm, and fits based on Eq. 4.1. The inset shows the conductance of the mesa versus t_{Cu}. All results were obtained as averages over nine devices and the error-bars are smaller than the size of the symbols.

nm, which means that altogether, the actual NC diameters are only slightly smaller than the nominal values. The agreement is quite good over a very wide range of NC diameters and for all Cu thicknesses used. An obvious and expected result is that the resistance decreases with increasing NC size and increasing Cu thickness. A less obvious, though still plausible, result is that an increase in Cu thickness simply reduces the device resistance by almost a constant value, regardless of NC size. We expect this behavior will help to reduce the current spread in our devices for all NC sizes, leading to stronger current perpendicular to the plane (CPP) from the top of the NC down through the mesa. Further, from plotting $1/R_{\mathrm{mesa}}$ against t_{Cu} (inset of Figure 4.2(b)), we can also conclude that the sheet conductance of the mesa increases linearly with t_{Cu}.

To investigate how the current is distributed and to ensure that the threshold current I_c can be controlled and reduced in these devices, the current flow in each layer of the NC-STNOs with bottom electrode thicknesses t_{Cu} = 10, 30, 50, and 70 nm and d_{NC} = 200 nm were calculated using COMSOL Multiphysics® simulation software using a detailed three-dimensional finite-element model of NC-STNO devices. In COMSOL, we first designed the structures of the NC-STNOs, following

the schematic shown in Figure 4.1(a), and the material characteristics were assigned to each layer. Afterwards, the input sources (e.g., dc current and ground) and other initial conditions were added and the software simulated and calculated the detailed profiles of the current density inside all layers of the devices.

Generally, the results (Figure 4.3) show that current from the top contact begins to crowd along the sides of the NC and then in the Cu cap and Cu spacer layers (Figure 4.3(a)). As has been already reported, the current distribution underneath the NC is mainly perpendicular to the film plane [132]. Demonstrating how the current spread changes with Cu thickness, Figure 4.3(b) and (c) present a side view of current density in all layers for $t_{Cu} = 10$ nm and $t_{Cu} = 70$ nm, respectively, normalized by the perpendicular current density in the ideal case. Here, in each of

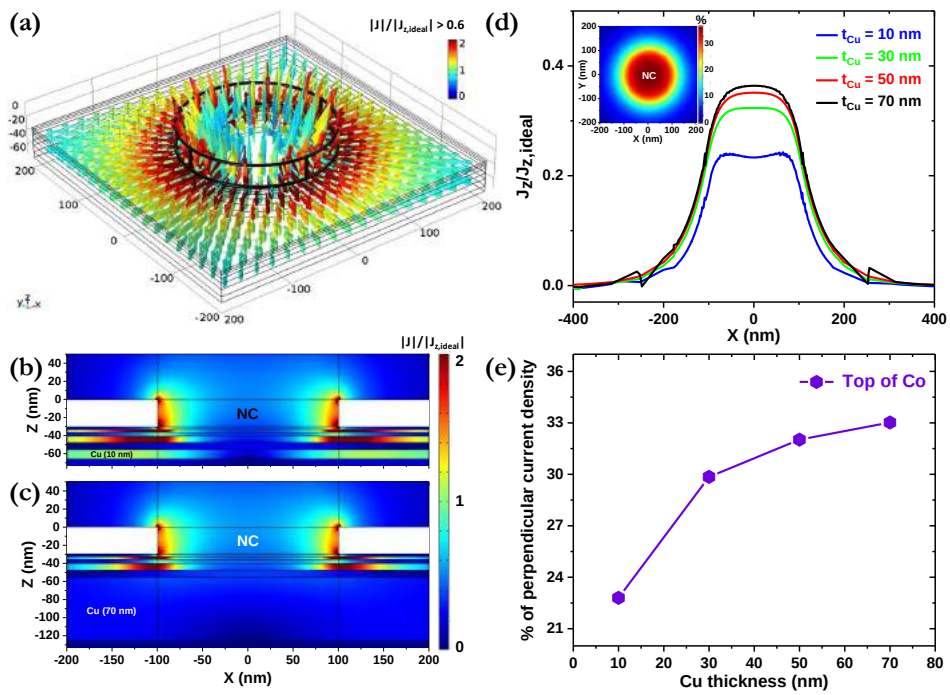

Figure 4.3: Simulations of: (a) 3D schematic of NC-STNO with $t_{Cu} = 10$ nm with representation of current density distribution by colored arrows. Current density in all layers (side view of the NC-STNO) for (b) $t_{Cu} = 10$ nm and (c) $t_{Cu} = 70$ nm, which are all normalized by the perpendicular current density in the ideal case. (d) Current density at the top of the Co layer; the inset shows the top view of the current density at the cross-section of this layer for $t_{Cu} = 70$ nm. (e) Calculated perpendicular current density ratio at the top of Co layer for $t_{Cu} = 10$, 30, 50, and 70 nm. All results are for NCs with $d_{NC} = 200$ nm.

these two figures, the effect of t_{Cu} on perpendicular current density can be seen. In comparing Figure 4.3(b) and (c), we can clearly see that, in a device with $t_{\mathrm{Cu}} = 10$ nm, most of the input current spreads along the space underneath the NC, meaning that there will be less CPP reaching the ferromagnetic layers. However, in $t_{\mathrm{Cu}} = 70$ nm, it is clear that we have a significant reduction of the current spread above the fixed and free layers, which helps to reduce the threshold current (I_c) and excite the free layer, resulting in more efficient microwave dynamics. Figure 4.3(d) shows how increasing t_{Cu} has a direct impact on the CPP density at top of the Co layer (J_z^{Co}). Figure 4.3(e) also highlighted this improvement and shows the calculated perpendicular current density ratio at the center of the NC on top of the Co layer J_z^{Co}, normalized by the average current density through the NC ($J_{z,\mathrm{avg}}^{\mathrm{Co}}$) for $t_{\mathrm{Cu}} = 10$, 30, 50, and 70 nm; the increase in this ratio is clear. As NC-STNO auto-oscillations are driven by the spin current generated by electrons reflecting against the fixed layer, it is reasonable to assume that I_c should scale with J_z^{Co}. We thus expect a thicker t_{Cu} to lead to reduced I_c.

To experimentally identify the effects of t_{Cu} on the threshold current and on the linewidth and power generated, we performed microwave measurements of the fabricated NC-STNOs. All measurements were performed at room temperature using a full 3D field microwave probe station described in section 3.3.2 (Config1), with which the magnetization dynamics are excited by applying a dc bias current and electrically measured using a homemade probe station with a fixed and uniform out-of-plane external magnetic field set by a Halbach array of permanent magnet with strength of $\mu_o H = 0.94$ T at $\theta = 80°$ with respect to the NC plane. The dynamics are then separated from the dc current using a 0.1 to 40 GHz bias-T and converted to the frequency domain by a Rohde & Schwarz FSU 46 spectrum analyzer, after having passed through a 45 dB gain amplifier with a bandwidth of 0.1–40 GHz (Figure 4.1(a)). Figure 4.4 shows the measured power spectral density (PSD) as a function of the dc current for NC-STNOs with $t_{\mathrm{Cu}} = 10$, 30, 50, and 70 nm and for currents between 10 and 40 mA. At each current, each spectrum was averaged five times with a video bandwidth of 10 kHz in order to minimize the noise. First observations indicates that the thicker the Cu underlayer, the earlier the onset of auto-oscillations. To extract I_c from the experimental results, we plot the inverse integrated power versus current (inset of Figure 4.5(a)) and extrapolate the initial linear dependence to an intercept on the current axis [122, 133]. The average result from three devices for each t_{Cu} (Figure 4.5(a)) shows a clear reduction of I_c as t_{Cu} increases.

Figure 4.5(b) shows the extracted I_c versus t_{Cu}, where I_c has been normalized to the value for $t_{\mathrm{Cu}} = 10$ nm. We can see a substantial reduction of about 40% in I_c when t_{Cu} increases from 10 nm to 70 nm. We also plot the predicted improvement based on our NC-STNO simulations (Figure 4.3(d)), assuming that J_z^{Co} drives the auto-oscillations. The agreement is essentially perfect for $t_{\mathrm{Cu}} = 10$ and 30 nm, and is very good for thicker Cu. We plot the extracted mesa resistance, which shows both simulation and experimental results with a low discrepancy, making it clear

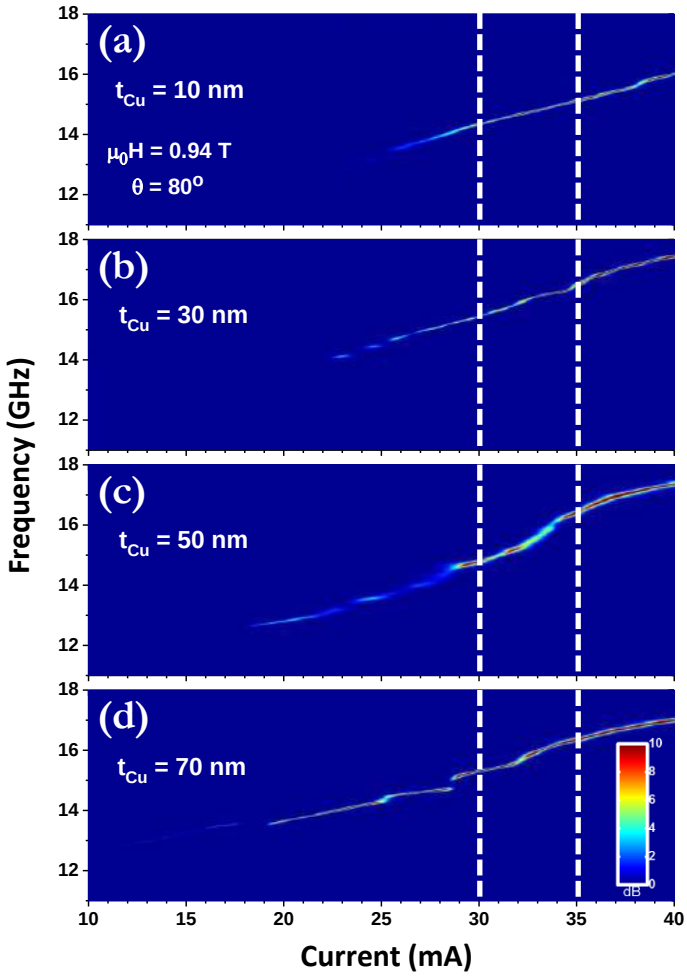

Figure 4.4: Color plot of the power spectral density as a function of current for (a) $t_{\mathrm{Cu}} = 10$ nm, (b) $t_{\mathrm{Cu}} = 30$ nm, (c) $t_{\mathrm{Cu}} = 50$ nm, and (d) $t_{\mathrm{Cu}}= 70$ nm. The vertical dashed white lines indicate a limited range of 30 to 35 mA, where all devices have stable oscillations.

that they are tracing the same trend as the resistances of the NC-STNOs.

In Figure 4.6, we plot the integrated power and power conversion efficiency for $t_{\mathrm{Cu}} = 10$, 30, 50, and 70 nm, both averaged over three devices for each value of t_{Cu}, and over the current range of 30 to 35 mA (as indicated in Figure 4.4) with a step of 0.1 mA (measured for 51 different input currents), where all devices have stable oscillations. We focused on this stable region to avoid the nonlinear dynamics of

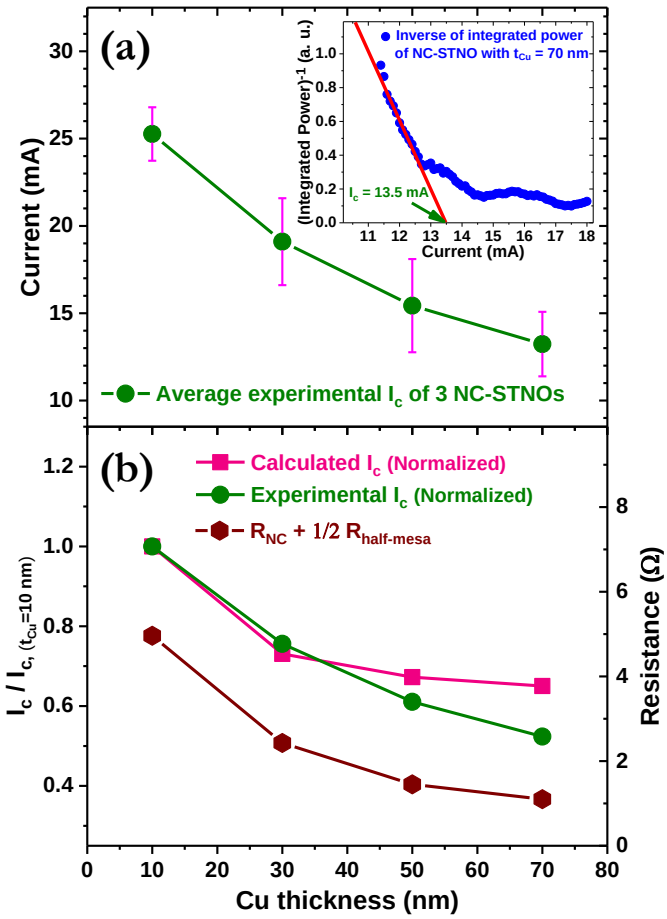

Figure 4.5: (a) Threshold current (I_c) versus Cu underlayer thickness averaged over three STNOs with $d_{\mathrm{NC}} = 200$ nm. Inset shows a linear fit of the inverse integrated power of NC-STNO with $t_{\mathrm{Cu}} = 70$ nm from which $I_{c,(t_{\mathrm{Cu}}=70\mathrm{nm})} = 13.5$ mA was determined. (b) Calculated and measured I_c (left axis) of NC-STNOs normalized by $I_{c,(t_{\mathrm{Cu}}=10\mathrm{nm})}$ for the same devices with corresponding resistances (R) (right axis) of different t_{Cu} (average of nine devices). The experimental results of I_c are averaged over three devices.

mode changes, since this approach is crucial for STNO applications. We observed a rather dramatic increase in the output microwave power for $t_{\mathrm{Cu}} > 30$ nm, such that the power at $t_{\mathrm{Cu}} = 70$ nm is an order of magnitude greater than at $t_{\mathrm{Cu}} =$ 10–30 nm. In addition, since the direct current losses (proportional to the STNO resistance) also decrease with increasing t_{Cu}, the power conversion efficiency, which is critical for reducing the energy consumption, improves by almost two orders of

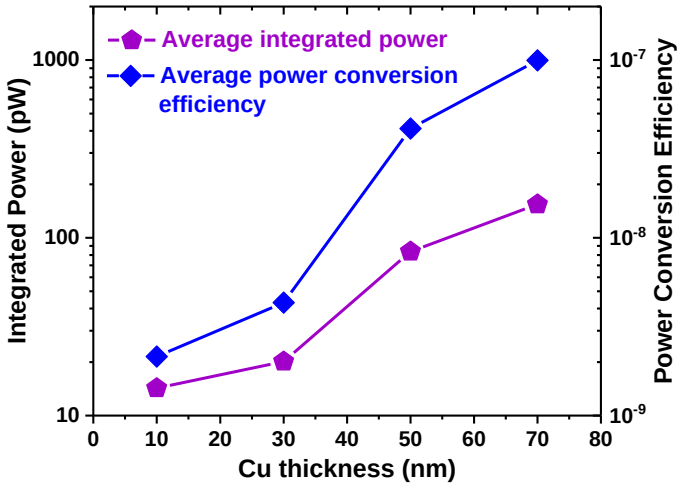

Figure 4.6: Integrated power (left axis) and power conversion efficiency (right axis) averaged over three identical NC-STNOs, each with $t_{\mathrm{Cu}} = 10$, 30, 50, and 70 nm and $d_{\mathrm{NC}} = 200$ nm, and over the current range 30–35 mA, indicated in Figure 4.4 with a step of 0.1 mA.

magnitude. These remarkable improvements clearly demonstrate that NC-STNO performance benefits greatly from an increase in perpendicular current density, and they provide a direct means of improving the usability of these devices as microwave signal generators.

4.2 Spin-Transfer Torque Ferromagnetic Resonance of NC-STNOs

NC-STNOs are based on the phenomenon of spin momentum transfer, and exhibit very rich magnetodynamics that depend on device geometry, material properties, and experimental conditions [112, 91, 134]. To better understand these phenomena and to further optimize these devices, it is essential to investigate STNO behavior under different conditions. Here we employed the spin-transfer torque ferromagnetic resonance (ST-FMR) technique [135, 136], described in Section 3.2.1, to characterize an NC-STNO device using the field rotational system (Section 3.3.1) in a range of external out-of-plane magnetic fields $\mu_0 H_{\text{ext}}$ at an angle of 75°. The device we used had t_{Cu}= 50 nm and d_{NC} = 100 nm with the same structure as described in the previous section.

ST-FMR measurements using homodyne detection are performed by passing a pulse-modulated microwave signal of 313 Hz from an rf signal generator via a bias-T to the NC-STNO device [69, 137, 124]. For each field strength from 0 to 0.5 T, in steps of 100 Oe, the microwave frequency f is swept from 2 to 15 GHz while the microwave power is held constant at −15 pW and I_{dc} = −0.1 mA. The same bias-T is used to transfer the device response of dc voltage (V_{dc}) modulated at 313 Hz to measure it in a phase-sensitive manner using a lock-in amplifier, which also provides a 313 Hz reference for the pulse modulation. Figure 4.7 shows the color map of acquired homodyne-detected ST-FMR spectra gained from all frequency scans at each magnetic field. This figure shows different resonance peaks from the ferromagnetic layers of the NC-STNO device. The inset illustrates an example of ST-FMR spectra at a magnetic field of 0.15 T. These results have been presented in Paper I.

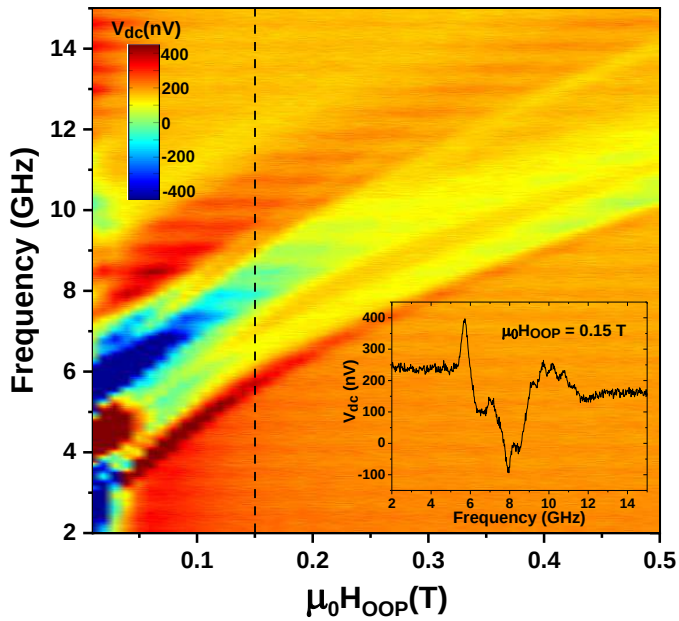

Figure 4.7: Color map of homodyne-detected ST-FMR spectra V_{dc} as a function of out-of-plane fields of $\mu_0 H_{\text{ext}}$ at $\theta = 75^\circ$ and rf frequency f, where $I_{dc} = -0.1$ mA, which shows different resonance peaks from the NC-STNO device. The inset shows ST-FMR spectra for the selected field value of 0.15 T as indicated by the vertical dashed line in the main Figure.

4.3 Tuning Spin-Wave Resonance in NC-STNOs

These results have been presented in Paper IV.

In the previous work [66] described in Section 4.1, we showed how the current distribution depends on the Cu thickness of the bottom electrode (t_{Cu}) in NC-STNOs based on Co/Cu/NiFe stacks. We found that increasing t_{Cu} from 10 to 70 nm results in a 40% reduction in the threshold current, an order of magnitude higher microwave output power, and close to two orders of magnitude better power conversion efficiency. A detailed study is presented in Section 4.1. Here, we apply the theory of this paper [124] to tune the spinwave resonance mode by modulating the current distribution and thus the distribution of the Oersted field (H_{Oe}). We use the same devices as described in Section 4.1 and investigate the effect of the bottom electrode thickness. We measure the rectified spectra of devices with d_{NC} = 250 nm using the ST-FMR technique (described in section 3.2.1) in an in-plane magnetic field, and compare the results with numerical simulations.

In the ST-FMR measurement set-up, the rf power was maintained at a low constant value of -10 dBm to ensure that the excited magnetodynamics would be in the linear regime. The measurements were performed at a fixed excitation frequency

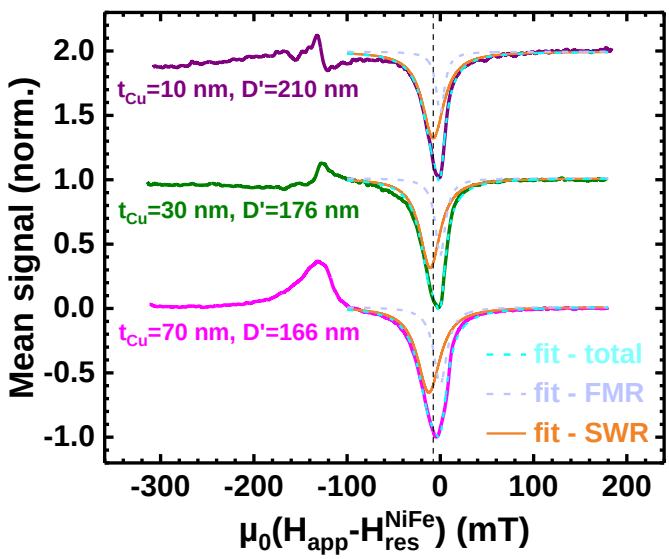

Figure 4.8: ST-FMR spectrum of NC-STNO devices with t_{Cu} = 10, 30, and 70 nm and D = 250 nm, taken at f = 18 GHz and P= -10 dBm, together with a fit (solid line) based on two Lorentzians, as described in Reference [124]. The vertical dashed line indicates the position of the SWR peak in the NiFe spectra for the sample with t_{Cu} = 10 nm.

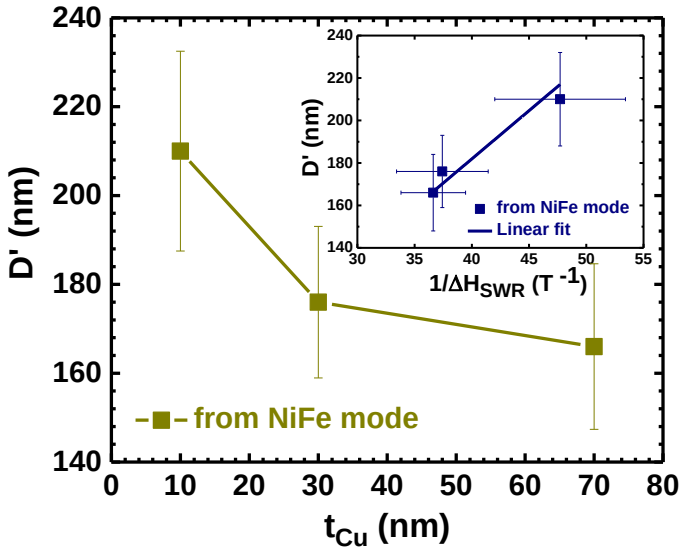

Figure 4.9: Mean value of effective diameter (D') versus thickness of Cu bottom layer. Inset: Plot of mean value of effective diameter (D') versus inverse of mean linewidth of the SWR mode extracted from the measurement of 5 NC-STNO devices.

of $f = 18$ GHz, while the in-plane applied field was swept from 0 to 0.5 T. In Figure 4.8, we present the results of measurements on five nominally similar devices, showing the normalized mean value of the spectra extracted from each of the three samples with $t_{\mathrm{Cu}} = 10$, 30, and 70 nm. Here the solid lines are fits of two symmetric Lorentzians to the NiFe peak at higher fields. The shift in the SWR position is distinct.

Based on Reference [124], the effective diameter (D') can be estimated using the dispersion relation. As a result, the extracted effective diameters from the fit for the free layer (NiFe) mode of each sample with $t_{\mathrm{Cu}} = 10$, 30, and 70 nm are calculated and presented in Figure 4.9. The results clearly show that, by increasing t_{Cu}, the mean effective diameter decreases monotonically and is inversely proportional to the mean linewidth (inset of Figure 4.9). Further, Reference [124] shows that the bandwidth of the SW package is proportional to the effective diameter.

The theory from our earlier study predicts that the effective diameter is determined by the Oersted field (H_{Oe}). To test this hypothesis, we investigated how the current redistributes and induces H_{Oe}. We used COMSOL Multiphysics® simulation software with a detailed three-dimensional finite-element model of the NC-STNOs to calculate the current flow and H_{Oe} in each layer of the device. In COMSOL, we first designed the structures of the NC-STNOs, following the schematic shown in Figure 4.1(a), and the material characteristics were assigned to each layer. Afterwards,

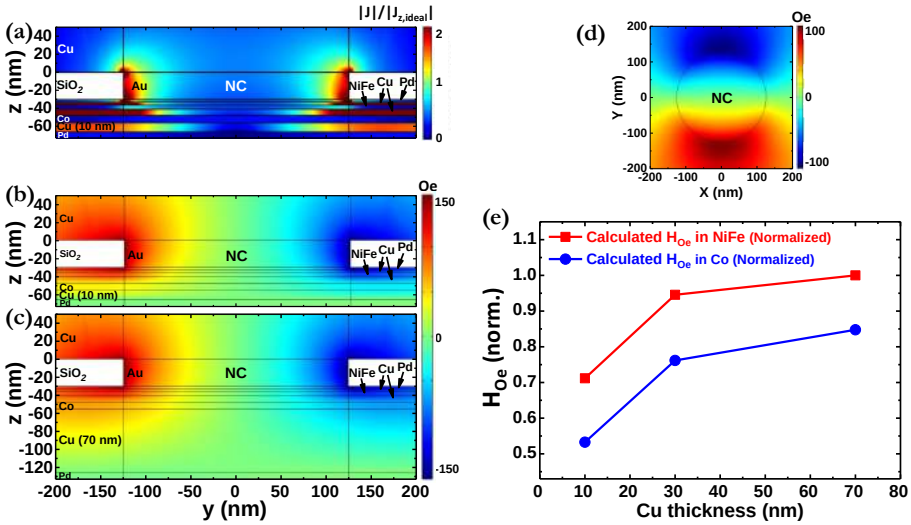

Figure 4.10: (a) Detailed current density in all layers for $t_{\mathrm{Cu}} = 10$ nm, normalized by the average perpendicular current density over the NC. (b) Detailed x component of H_{Oe} induced by perpendicular current in all layers for $t_{\mathrm{Cu}} = 10$ nm. (c) The same for $t_{\mathrm{Cu}} = 70$ nm. (d) The top view of the middle of the NiFe layer; the colored map shows the x component of H_{Oe} for $t_{\mathrm{Cu}} = 70$ nm. (e) Calculated average strength of H_{Oe} induced by perpendicular current under the NC in the middle of NiFe and Co layers normalized by $H^{\mathrm{NiFe}}_{\mathrm{Oe},(t_{\mathrm{Cu}}=70\ \mathrm{nm})}$. All results are for $D = 250$ nm.

the input sources (e.g., dc current and ground) and other initial conditions were added and the software simulated and calculated the specified parameters inside all layers of the devices.The input values of the nanocontact size and Cu thickness were D = 250 nm and t_{Cu} = 10, 30, and 70 nm, respectively. Figure 4.10 shows the results of calculations.

Our previous results [66] show that the current from the top contact first crowds along the perimeter of the NC before spreading out laterally (Figure 4.10(a)) and that, by increasing t_{Cu}, we can strongly reduce the lateral current spread. Accordingly, Figure 4.10(b) and (c) show that the Oersted field induced by perpendicular current underneath the NC increases with thicker t_{Cu} as a result of the current spread reduction. In Figure 4.10(e), we highlight this amplification in both free and fixed layers by plotting the average strength of H_{Oe} in the middle of the NiFe ($H^{\mathrm{NiFe}}_{\mathrm{Oe}}$) and Co ($H^{\mathrm{Co}}_{\mathrm{Oe}}$) layers under the NC geometry, normalized by $H^{\mathrm{NiFe}}_{\mathrm{Oe},(t_{\mathrm{Cu}}=70\ nm)}$.

The results show that, when t_{Cu} is increased from 10 to 70 nm, the values of $H^{\mathrm{NiFe}}_{\mathrm{Oe}}$ and $H^{\mathrm{Co}}_{\mathrm{Oe}}$ undergo remarkable increases of ~30% and ~60%, respectively, underneath the NC geometry. This dramatic increase in the Oe field is caused by lower lateral current spread in NC-STNOs with thicker bottom electrode. There will

thus be a larger perpendicular current density under the NC geometry, resulting in higher Oersted field in devices with thicker t_{Cu}. The Oersted field plays a key role in exciting the dynamics and decreasing the effective diameter with increasing Cu thickness, as illustrated in Figure 4.9. We can therefore conclude that it is possible to tune the SWR by tailoring the lateral current.

Finally, we used ST-FMR technique to study magnetodynamics excited by the Oersted-field in NC-STNOs. We controlled the current distribution, and thereby the H_{Oe} distribution, by varying the bottom Cu layer thickness. The results show that changing Cu thickness is an efficient method to tune propagating spin waves. The main wave-vector ($k = \pi/D^{'}$) of the SWs also increases for thicker Cu layers. Simulations show that the current distribution governs the strength of the Oersted-field which has a direct impact on the characteristics of the spin waves.

4.4 Control of Thermal Budget in NC-STNOs

Following our previous work [66], described in Section 4.1, we here use the same multilayer devices to investigate the effect of bottom Cu electrode thickness (t_{Cu}) in NC-STNOs based on Co/Cu/NiFe GMR stacks on the Joule heating induced by current flow inside of the devices. We carried out modeling of Joule heating using COMSOL Multiphysics® simulation software with a detailed three-dimensional finite-element model of these NC-STNOs. We simulated the devices with Cu bottom layer thicknesses of t_{Cu} = 10, 30, and 70 nm and with NC diameter d_{NC} = 100 nm. In COMSOL, we first designed the structures of the NC-STNOs, following the schematic shown in Figure 4.1(a), and the material characteristics were assigned to each layer. Afterwards, the input sources (e.g., dc current and ground) and other initial conditions were added and the software simulated and calculated the detailed profiles of the current density and Joule heating inside all layers of the devices.

Figure 4.11 shows the simulation results. Figure 4.11(a) depicts current density of the NC-STNO with t_{Cu} = 10 nm. Figure 4.11(b) and (c) illustrate simulations of Joule heating in all layers with detailed results of the magnetically active region and a top view of the NiFe layer, respectively, for the NC-STNO with t_{Cu} = 10 nm. Figure 4.12 also shows the calculated temperature at specific levels in the layer structure of NC-STNO devices, and the inset shows the simulation of Joule heating from the side view of NC-STNO with t_{Cu} = 10 nm.

In Figure 4.13, we compared the simulation results for devices with t_{Cu} = 10, 30, 50, and 70 nm. Based on the calculated average temperature of the NC, as well as the NiFe and Co layers underneath the NC, we found that increasing Cu bottom layer thickness from 10 nm to 70 nm reduces the temperature in both the NiFe and Co layers by around 47%. For example, the average temperature of the Co layer under the NC geometry reduces from 343.65 K to 319.77 K, which is a ~ 24 K reduction in temperature (room temperature was taken as 293.15 K). Finally, we can suggest a modification to NC-STNO structure which to reduce temperature in such devices. Based on the previous studies, this heating reduction directly improves the spin-torque efficiency and stability of the output microwave signal [138]. These results have been presented in Paper V.

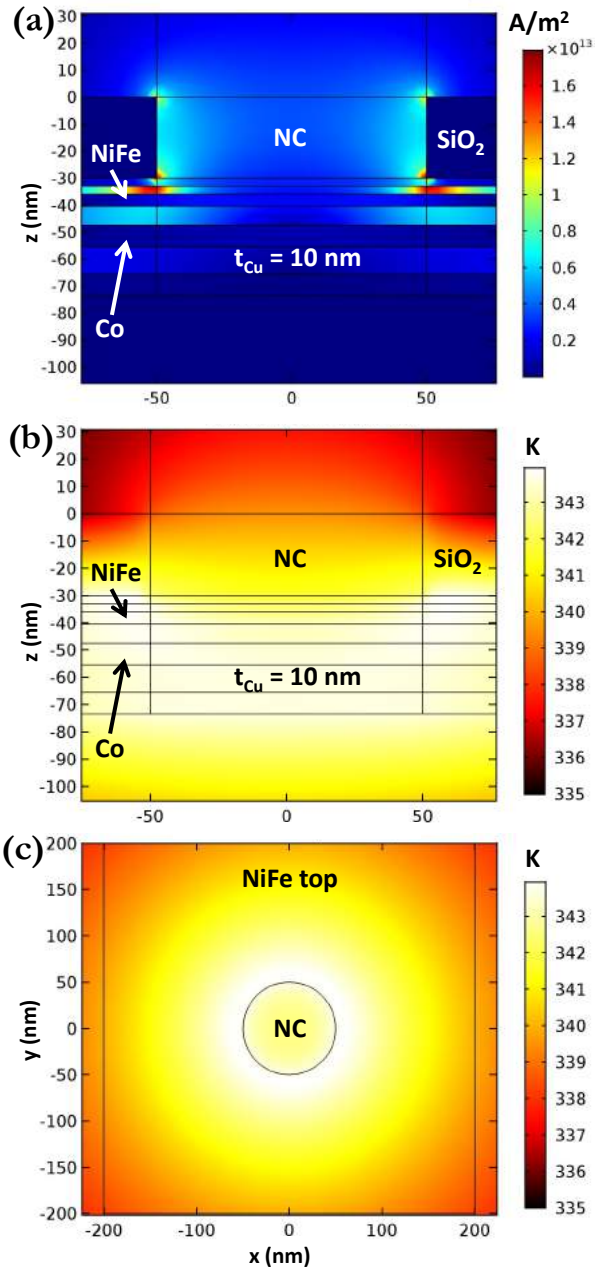

Figure 4.11: Simulations of (a) current density and Joule heating in (b) all layers (detailed results of magnetically active region), and (c) top view of NiFe layer. All results are for $t_{\mathrm{Cu}} = 10$ nm and $d_{\mathrm{NC}} = 100$ nm.

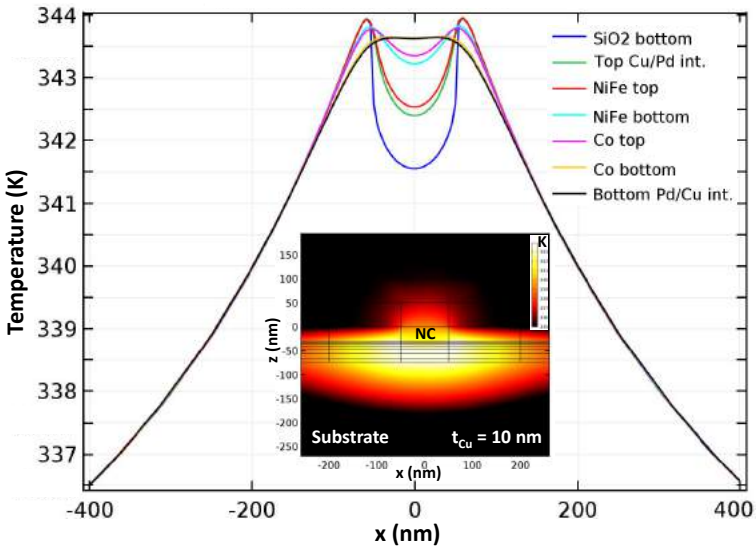

Figure 4.12: Calculated temperature of all layers of the device. Inset: Simulation of Joule heating in all layers of NC-STNO. All results are for $t_{\mathrm{Cu}} = 10$ nm and $d_{\mathrm{NC}} = 100$ nm.

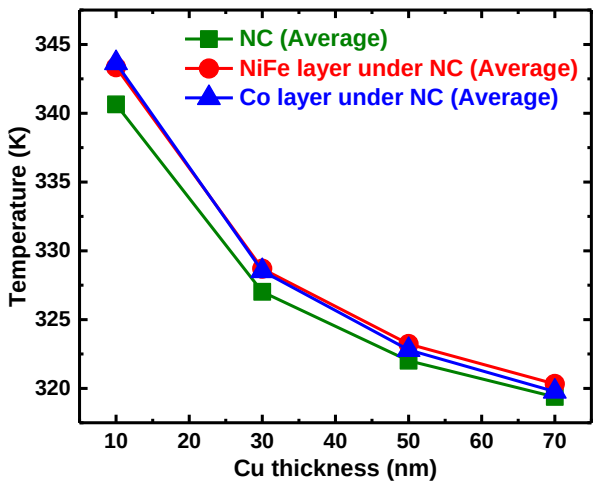

Figure 4.13: Comparing the calculated average temperatures of the NC, as well as the NiFe and Co layers underneath the NC devices with $t_{\mathrm{Cu}} = 10$, 30, 50, and 70 nm and $d_{\mathrm{NC}} = 100$ nm. Room temperature = 293.15 K.

4.5 NC-STNO in Oblique Magnetic Fields: Characterization of High Frequency Responses

In this part, we measured the spin-torque-driven oscillations in the NC-STNO as a function of field angle. We investigate how, for a given out-of-plane magnetic field angle and magnitude, merely changing the field polarity and azimuthal angle can significantly alter the device's output. In our experiments, the sample is a single NC-STNO with the following layer structure: Pd(8)-Cu(50)-Co(8)-Cu(7)-NiFe(4.5)-Cu(3)-Pd(3) (numbers indicate thicknesses in nm) and a nominal NC diameter of 100 nm, whose detailed structure is described in Section 4.1. The schematics of the device and the transmission line for dc and microwave characterization of the device are given in Figure 4.1. In our measurements, the direct dc current was provided to the sample using a Keithley 6221 current source and the sample voltage was monitored using a Keithley 2182 nanovoltmeter. A bias-T was used to apply current directly to the device while passing the generated microwave signal through a low-noise amplifier (gain 41 dB; bandwidth 0.1–40 GHz) from Miteq, and finally detecting the output signal using a Rohde & Schwarz FSU 67 spectrum analyzer. All measurements were performed using a drive current of 20 mA. Using the 3D field system (Config1) described in Section 3.3.2, a magnetic field with a constant magnitude of 0.95 T was applied at three different azimuthal angles (φ=−15°, 0°, and 15°) and its out-of-plane angle was then rotated a full 360°, starting from a parallel orientation (θ=0°), according to the coordinate system shown in the inset of Figure 3.14(a).

Angular dependence of oscillation (out-of-plane angle)

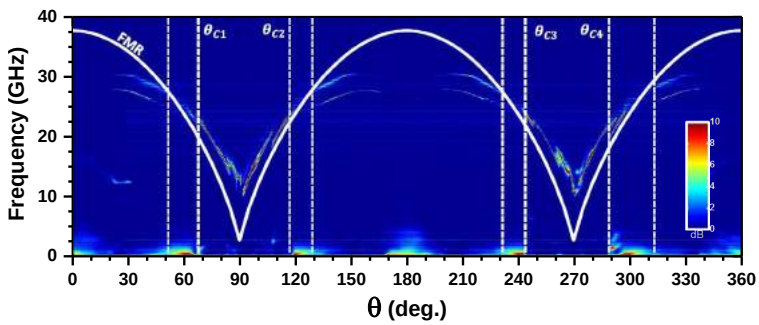

Figure 4.14: Power spectral density of an NC-STNO as a function of the external magnetic field angle θ and oscillation frequency of the measured device with I_{dc} = 20 mA. The vertical dashed white lines represent critical angles (θ_c) which between them, only a single mode with an oscillation frequency above the FMR frequency can be observed. Here, θ is according to the coordinate system shown in the inset of Figure 3.14(a).

Figure 4.14 shows the behavior of the NC-STNO microwave signal versus the out-of-plane angle of the applied magnetic field θ from 0° to 360°. Between the critical angles, only a single mode with an oscillation frequency above the FMR frequency of the NiFe film is observed, and has been attributed to a propagating spin wave (SW) in the NiFe layer [102]. A second mode with a frequency far below the FMR frequency also exists, corresponding to the localized SW bullet [105]. However, the critical angle θ_c and propagating modes are not symmetrical.

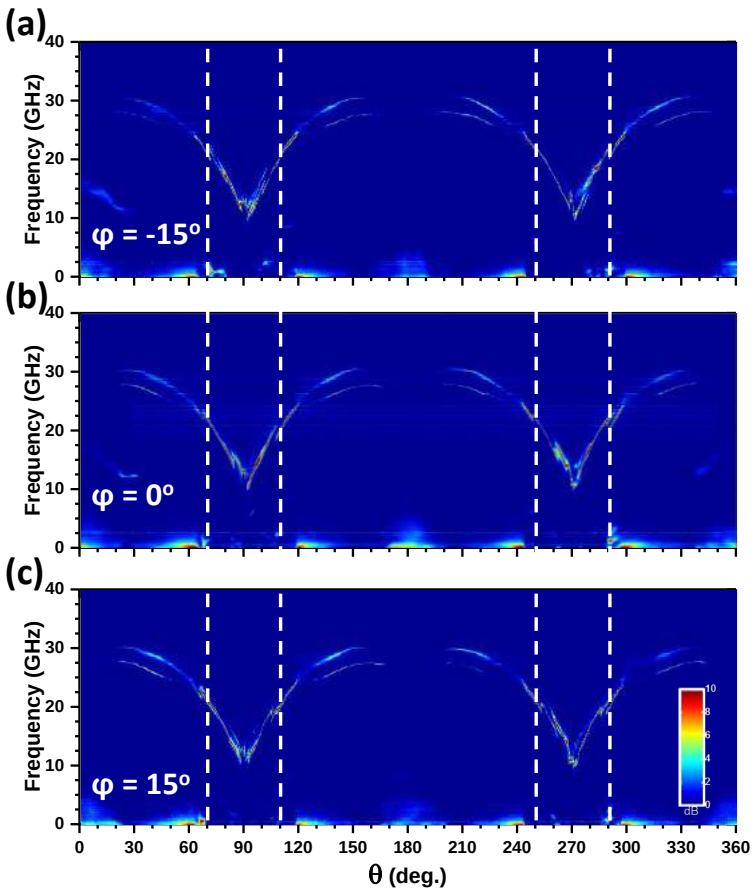

Figure 4.15: Power spectral density of NC-STNO as a function of external magnetic field angle θ and oscillation frequency with I_{dc} = 20 mA at (a) $\varphi = -15°$, (b) $\varphi = 0°$, and (c) $\varphi = 15°$. The vertical dashed white lines indicate twelve symmetric polar angles with respect to the sample plane. Here, θ and φ are according to the coordinate system shown in the inset of Figure 3.14(a).

Angular dependence of oscillation (in-plane angle)

In Figure 4.15, for full θ scans from 0° to 360° with φ= −15°, 0°, and 15°, each plot shows variation in peak frequencies for symmetric polar angles with respect to the sample surface, as well as inconsistencies in mode transitions. Further, in a comparison between plots, we can see variations in peak frequency for same polar angles by changing the azimuthal angle.

Angular dependence of STNO peak frequency, output power, and linewidth

To better understand these behaviors, we extracted some of the microwave properties for twelve symmetric angles with respect to the sample plane; these are the four symmetric polar angles (θ = 70°, 110°, 250°, and 290°) with three different azimuthal angles (φ = −15°, 0°, and 15°), as shown by the vertical dashed white lines in Figure 4.15(a), (b), and (c). As an example, the output spectrum of NC-STNO at θ = 70° and φ = 0° with I_{dc} = 20 mA is plotted in Figure 4.16(a). The NC-STNO peak frequency, output power, and linewidth vary by hundreds of MHz,

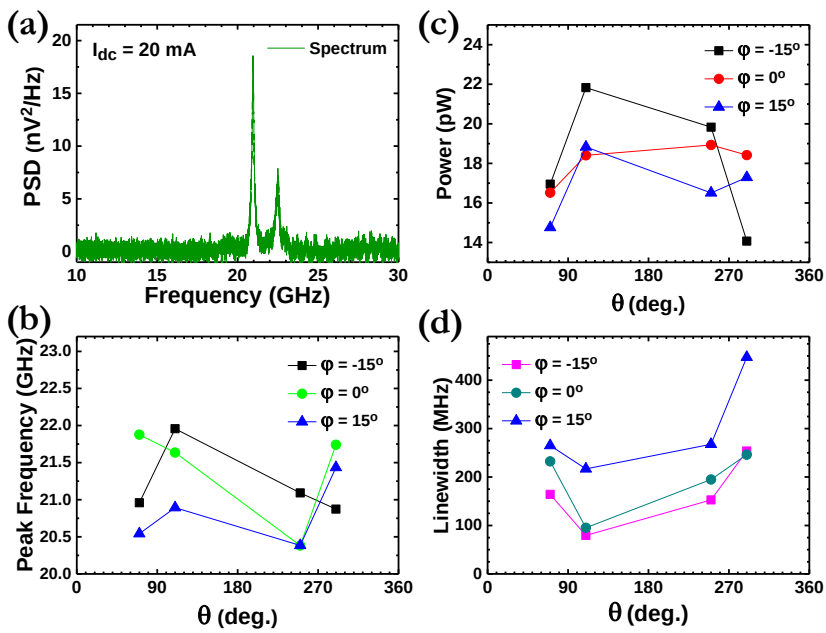

Figure 4.16: (a) Output spectrum of NC-STNO at θ = 70° and φ = 0° with I_{dc} = 20 mA; (b) peak frequency, (c) integrated power, and (d) linewidth of NC-STNO measured at four different symmetric out-of-plane angles, at in-plane angles of φ = −15°, 0°, and 15°.

several pW/MHz, and hundreds of MHz, respectively, as shown by Figure 4.16(b), (c), and (d).

Finally, we studied the microwave properties of NC-STNOs with respect to altitude and azimuth angles of the applied external magnetic field. Our consistent measurements show that there are variations in the linear and nonlinear frequencies and amplitude responses when the polar and azimuthal angles of the magnetic field are rotated. These results suggest some form of inhomogeneity in the material and domain structures, as well as a broken symmetry in the geometry, which causes the oscillation behavior to display a strong dependence on θ and φ. Determining the potential reasons for the anisotropic frequency variation in these oscillators leads to a deeper understanding and optimization of the film growth and fabrication process. These results have been presented in Paper I.

4.6 NC-STNO in Oblique Magnetic Fields: Magnetic Droplet Soliton Nucleation

The evidence of magnetic droplet soliton nucleation in oblique magnetic field has been studied extensively in Paper VI [139], and the materials and data in this section and appended paper are reprinted with permission from [M. Mohseni, M. Hamdi, H. F. Yazdi, S. A. H. Banuazizi, S. R. Sani, S. Chung, J. Åkerman, and M. Mohseni, Physical Review B **97**, 184402 (2018).] Copyright (2018) by the American Physical Society.

It has been shown that NC-STNOs exhibit different types of spin waves, such as propagating waves [35, 55, 140, 141] and magnetic droplet solitons [106, 142, 143, 144]. After the demonstration and observation of the droplets, various rich dynamical aspects of these nanoscale solitons—such as drift resonance instability [145, 146], droplet propagation [147], nucleation boundaries [148], merging [149], and perimeter mode excitation [144] have been studied.

Here we use the 3D field probe station described in Section 3.3.2 as well as another probe station with higher magnetic fields to study the angular dependence of the magnetization dynamics in orthogonal NC-STNOs. We also supported our experiments with micromagnetic simulations and theoretical calculations. We showed that—although droplet soliton nucleation has been previously demonstrated in

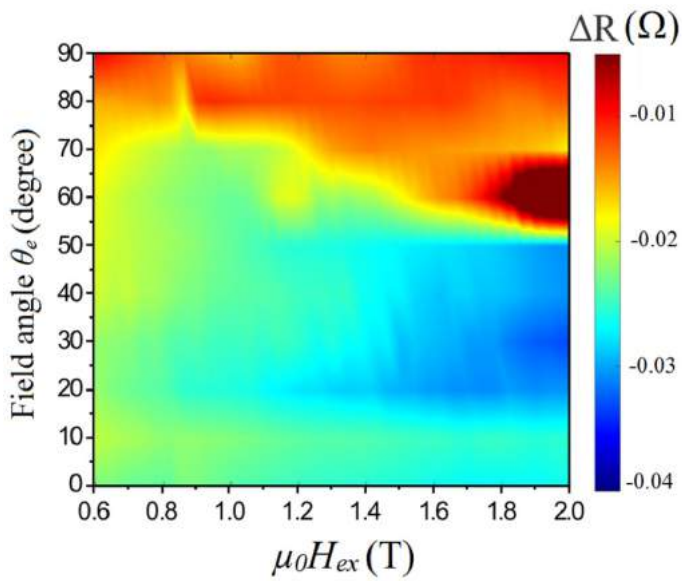

Figure 4.17: Color map of the measured angular field-dependent MR of the NC-STNO at a constant current of $I_{dc} = 20$ mA.

perpendicular fields—the nucleation of droplets is not limited to perpendicular fields, and droplet nucleation in oblique fields at a critical angle can be observed both through magnetoresistance (MR) and NC-STNO dynamics. In perpendicular fields and at out-of-plane (OOP) field angles down to the critical angle, droplet nucleation can be observed. However, for field angles below the critical angle, the droplet gives way to propagating spin waves, in agreement with our micromagnetic simulations and theory.

We employed the same samples as described in References [106, 148]—orthogonal pseudo-spin-valves (PSVs) with Co(8)/Cu(8)/Co(0.3)[Ni(0.8)/Co(0.4)]×4 layers (all thicknesses given in nm) with an NC radius of 50 nm, consisting of fixed, spacer, and free layers, as described in previous sections. All measurements were performed at room temperature using the home-made microwave probe station with an accurate and uniform magnetic field. The dc current was applied to the NCs with a negative polarity and electrons flowing from the free to the fixed layer. In addition, all the micromagnetic simulations were performed using GPU-based MuMax 3.0 [150].

In Figure 4.17 we show a color map of the measured MR versus field at different angles at a constant applied current of $I_{dc} = 20$ mA to demonstrate that the MR starts to increase from certain angles when the system tends to transform from small-angle precession to a droplet. In this figure, it is clear that below $\theta_e \sim 52°$, there is no sign of droplet mode at any field. Figure 4.18(a)-(c) also represent the field-dependent MR of the NC-STNO at different angles of $\theta_e = 20°$, $\theta_e = 60°$, and $\theta_e = 90°$ with a constant current of $I_{dc} = 20$ mA. At $\theta_e = 20°$, the NC-STNO has its expected behaviour in orthogonal PSVs which the MR decreases by increasing the field. However, in $\theta_e = 60°$ and $\theta_e = 90°$, it is clear that the MR first decreases, but at a certain magnetic field, it tends to increase which indicates the formation of a droplet under the NC [106].

Figure 4.19 presents the power spectral density of the angular dependency of the NC-STNO frequency at a constant current of $I_{dc} = 20$ mA and an applied field of $\mu_0 H_{\text{ext}} = 1$ and 1.2 T, as determined both experimentally and from the

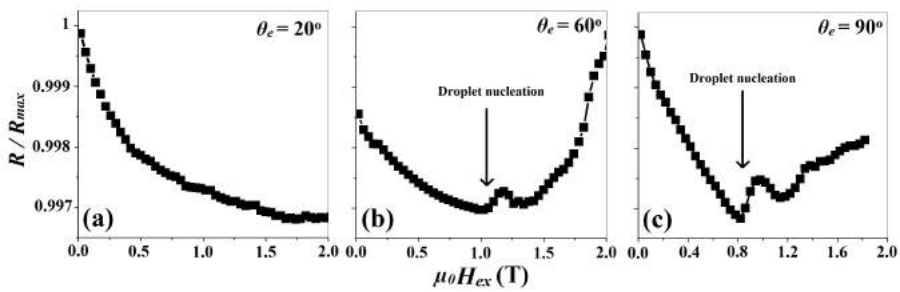

Figure 4.18: Field-magnitude-dependent MR of NC-STNO at $I_{dc} = 20$ mA and (a) $\theta_e = 20°$, (b) $\theta_e = 60°$, (c) $\theta_e = 90°$.

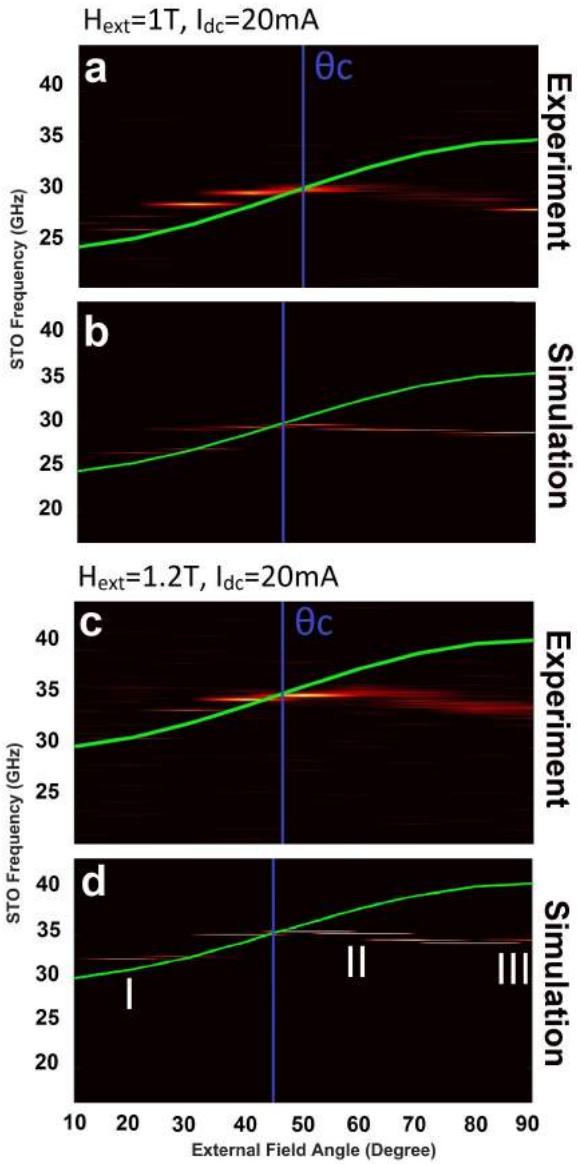

Figure 4.19: Power spectral density of NC-STNO frequency versus applied field angle for an applied current of I_{dc} = 20 mA. (a) and (b) ((c) and (d)) show the experimental and simulation data for external applied field of $\mu_0 H_{\text{ext}}$ = 1 T (1.2 T). The solid green curves show the angular-dependent FMR frequency, while the solid blue lines indicate the critical angle of the droplet nucleation; The labels I, II, and III in (d) indicate θ_e = 20°, θ_e = 60°, and θ_e = 90°, respectively.

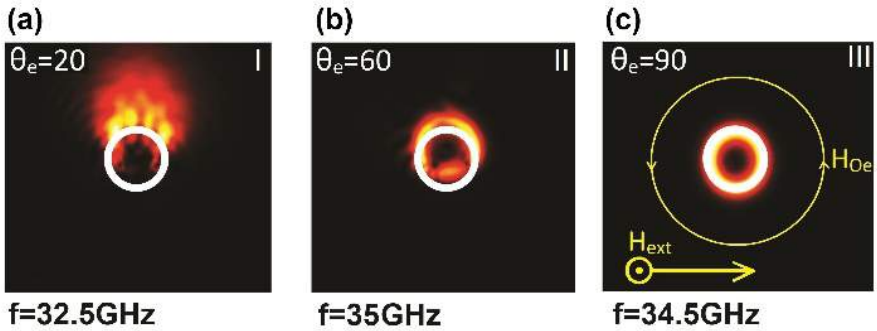

Figure 4.20: Spatial profiles of spin-wave excitations for an applied current of I_{dc} = 20 mA and external applied field of $\mu_0 H_{\text{ext}}$=1.2 T. (a), (b) and (c) show the spatial profiles of the modes at θ_e = 20°, 60°, and 90° respectively, as indicated by I, II, and III in Figure 4.19(d).

simulation. The solid green lines indicate the angular-dependent FMR frequency of the device. The solid blue vertical lines represent the critical angle, θ_c, of the droplet nucleation, which is the angle where the frequency of the system drops below the FMR frequency. Figure 4.20(a)–(c) shows the corresponding simulated spatial profiles of the excited wave with the labels I, II, III in Figure 4.19(d) at angles of θ_e = 20°, 60°, and 90°, respectively.

In Figure 4.20(a), we illustrate the spatial profile of the spin-wave mode at a low angle (θ_e = 20°), which shows a spin-wave beam due to the broken spatial symmetry around the NC induced by the Oersted field of the dc current [151]. As depicted in Figure 4.20(b) for the spatial distribution of the mode at θ_e = 60°, it is clear that the lower frequency mode disappears and a higher frequency mode begins to appear as the applied field angle increases above θ_c. As expected from both the MR and microwave measurements, the droplet is nucleated at this angle. However, the Oersted field of the applied current induces an asymmetric energy landscape around the NC, and the droplet thus tends to drift toward regions with a lower in-plane field above the NC [145]. Figure 4.20(c) also shows that the energy landscape becomes more symmetric when the angle of the external field increases, causing the drift instability to disappear at θ_e = 90° and the spatial profile of droplet to become almost symmetric.

In order to distinguish the presence of the soliton and the propagating spin-wave when the device is obliquely magnetized, we used both experiment and simulation to obtain a field-angle phase diagram for the angular dependency of the magnetization dynamics in our NC-STNOs for a range of applied fields from $\mu_0 H_{\text{ext}}$ = 0.6 to 1.2 T. As indicated in Figure 4.21, for each field strength below θ_c, the spin-wave dynamics of the NC-STNO show a propagating wave; above θ_c, the excited spin waves convert to localized solitonic droplet modes. Furthermore, θ_c increases slightly as the applied

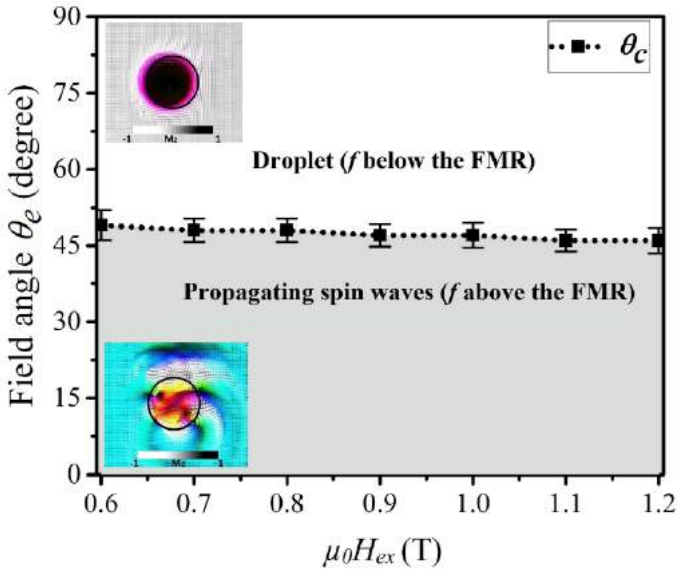

Figure 4.21: Phase diagram of the droplet nucleation critical angles θ_c versus the applied field magnitude and angle in orthogonal NC-STNOs, which separates the localized droplet area (white region) and nonlocalized propagating SW area (gray region).

field magnitude increases.

In conclusion, we have presented evidence of droplet nucleation under oblique fields in orthogonal NC-STNOs. Our results show that droplet nucleation is not limited to perpendicular fields and the angular dependence of spin-wave dynamics shows two fundamentally different modes. The droplets nucleate where the external field is nearly perpendicular in direction, while the propagating spin waves are the dominant mode in oblique fields, where there is an in-plane field component. The transition between these two modes takes place at a determinable angle that can be found using a phase diagram covering solitonic and propagating waves. Our results give us a better understanding of nanoscale solitons and spin-wave dynamics in NC-STNOs.

4.7 Low-Current STNOs Based on Perpendicular Magnetic Tunnel Junctions

Low-current STNOs based on perpendicular magnetic tunnel junctions were studied extensively in Paper VII.

In this study, we demonstrate ultra-high frequency tunability of up to 4.4 GHz/mA and low threshold currents of about -21 μA in STNOs based on magnetic tunnel junctions (MTJs) with a CoFeB/MgO/CoFeB stack in which both free and fixed layers display perpendicular magnetic anisotropy (PMA). According to previous studies, all-perpendicular MTJs (p-MTJs) offer clear advantages for magnetoresistive random access memory in terms of low switching current density [152, 153, 154, 155, 156, 157, 158, 159] and high thermal stability [154]. While nano-oscillator devices such as NC-STNOs can also benefit from materials with perpendicular magnetic anisotropy (PMA), STT-driven microwave generation in this all-perpendicular system has not yet been studied in detail. Using the field rotational microwave probe station described in Section 3.3.1, we here show high-frequency STNO operation in our MTJ devices.

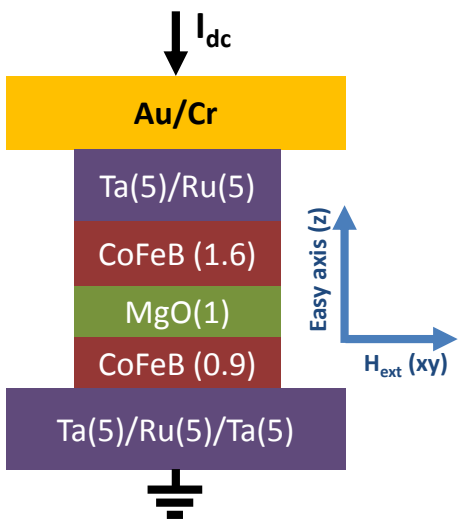

Figure 4.22: Schematic of MTJ-based STNO device structure.

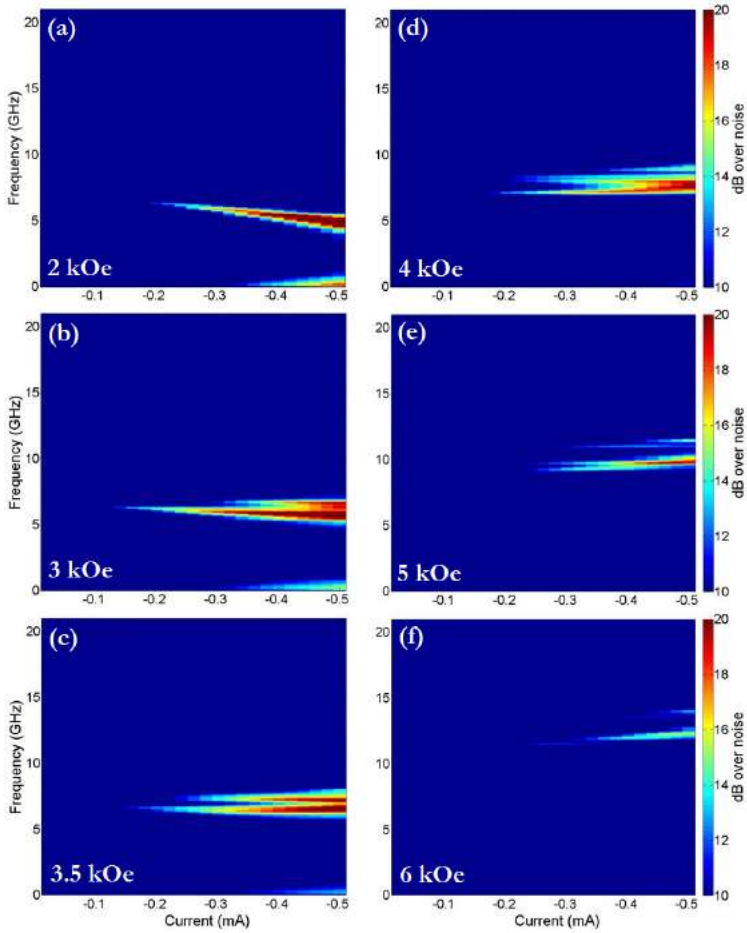

Figure 4.23: Color maps of power spectral density as a function of current generated by MTJ-based STNOs at six applied magnetic field of (a) 2 kOe, (b) 3 kOe, (c) 3.5 kOe, (d) 4 kOe, (e) 5 kOe, and (f) 6 kOe.

Figure 4.22 illustrates a schematic of MTJ-based STNO device structure. In our devices, this stack was sputtered onto a sapphire wafer: Ta(5)/Ru(10)/Ta(5)/Co_{20} Fe_{60} B_{20} (0.9)/MgO(1)/Co_{20} Fe_{60} B_{20} (1.6)/Ta(5)/Ru(5) (all thicknesses in nm) with a nanopillar diameter of 100 nm. We connected the transmission line for microwave measurements as described in Section 3.2.2 and all measurements were carried out at drive current limited to -350 μA. Microwave signal generation was studied as a function of both the drive current and the in-plane (IP) magnetic field.

The results of the microwave measurements are presented in Figure 4.23, where the PSD is shown as a function of current for eight values of applied IP fields ranging

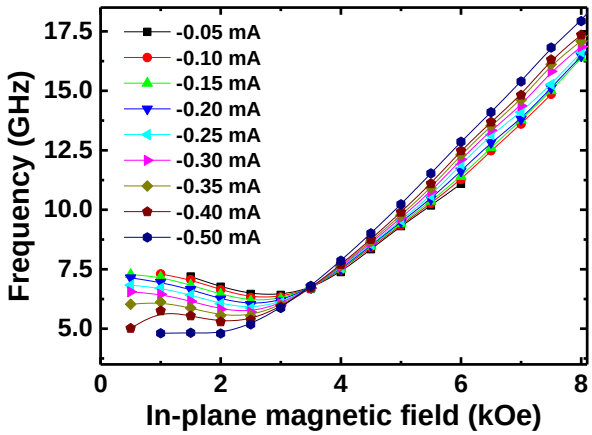

Figure 4.24: Field-magnitude dependency of MTJ-based STNO frequency at different bias currents.

from 2 to 6 kOe. At magnetic fields below 3.5 kOe, we observe a single mode at high frequencies. At 3.5 kOe, a second mode with higher frequency also appears, and at 4.5 kOe a third mode with much lower power can be observed under high current. We also fitted a Lorentzian to the PSD at each current and field value; the extracted peak frequencies are plotted as a function of field magnitude for different currents in Figure 4.24 for fields ranging from 0 to 8 kOe. The results show that the minimum point gradually shifts from 3 to 2 kOe when the current increases from -0.05 to -0.35 mA. This frequencies red-shift is Kittel-like and causes the precession of the magnetization of the free layer to be induced by the STT effect [160]. The microwave signal generated at 5 GHz and above is also the highest of previously reported frequencies in MgO-based MTJ nanopillar STNOs.

Figure 4.25 shows the PSD as a function of applied magnetic field; this also extracted from the Lorentzian fitting of field-sweep spectra at various input currents. The results show that the power increases gradually with applied current. Further, the peak shifts from 3.5 to 2.5 kOe simultaneously with the turning points of the field-dependent oscillation frequency in Figure 4.24. The threshold current of microwave oscillation is given from a linear fitting of the inverse of the integrated power versus current, which is plotted in the inset to Figure 4.25. A threshold current of $I_{c0} = 21\ \mu A$ is extracted from the linear fitting; this equals a critical current density of $J_{c0} \simeq 2.77 \times 10^5 \mathrm{A/cm^2}$. This threshold current is the lowest value reported to date.

In conclusion, we experimentally studied STNOs based on nanopillar MTJs with a 100 nm diameter in which both the free and polarizer layers are PMA CoFeBs. We demonstrated high-frequency STNO oscillation from 5 GHz to over 10 GHz,

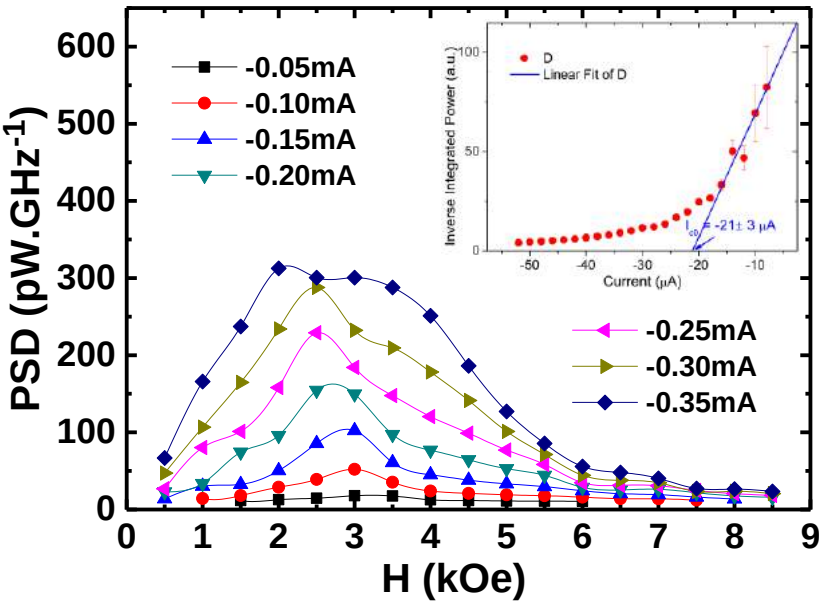

Figure 4.25: Power spectral density of measured MTJ-based STNOs versus applied field at different input currents. Inset: Linear fitting of the inverse of integrated power as a function of current; a threshold current of -21μA was extracted.

which is the highest range reported to date for MgO-based MTJ nanopillar STNOs. Furthermore, high current tunabilities of frequency and extremely low threshold current densities were observed.

Chapter 5

Spin Hall Nano-Oscillators

Spin-wave excitations driven by spin-transfer torque (STT) [35, 36, 161, 55] have become an important area of research during the last decade, both from a fundamental point of view and for their potential in applications using spintronic devices, such as spin torque and spin Hall nano-oscillators [30]. Recent investigations have shown that the spin Hall effect (SHE) in a nonmagnetic film with strong spin-orbit interaction (such as Pt) can induce a pure spin current that can then be used to exert enough STT on an adjacent ferromagnetic thin film to drive spin-wave auto-oscillations. These kinds of oscillators are called spin Hall nano-oscillators (SHNOs) [46, 45, 162, 163, 164, 39] and have great potential for applications in the next generation of signal generators, [165, 33] as these devices are nanosized and have low power consumption; they are also easy to fabricate and have reasonably good emission characteristics.

This chapter describes characterizations of spin Hall nano-oscillator (SHNO) devices based on different structures and materials, using both conventional and novel methods. I first present a detailed study of the current and induced magnetic field and describe the temperature profiles of nanogap SHNOs. In addition, we show the current and in-plane magnetic field dependence of nanoconstriction spin Hall nano-oscillators based on NiFe/Pt and NiFe/W. It has been shown that multiple SHNOs can be serially synchronized, thereby increasing their output power and enhancing the value of these devices in applications. Here we show the synchronization of nanoconstriction SHNOs in low in-plane magnetic fields. Moreover, I present the result of a novel method of probing an operational nanoconstriction-based SHNO using a magnetic force microscope.

5.1 Current, Field, and Temperature Profiles in Nanogap SHNOs

An extensive investigation of nanogap SHNO current, field, and temperature profiles is presented in Paper VIII.

The oscillation frequencies and the spin-wave modes in the SHNOs depend on the applied external magnetic field and the dc current. It is thus crucial to have a clear understanding of the current distribution, which has a direct impact on the auto-oscillating active region. The electric current leads to a temperature increase due to Joule heating, which can cause frequency shifts and also degrades device performance. In addition, an Oersted field (H_{Oe}) induced by dc current modifies the effective field landscape in SHNOs, affecting some of the main properties of their high frequency emissions.

We here investigated the angular dependence of anisotropic magnetoresistance (AMR), together with simulations of current distribution, Joule heating, and H_{Oe} in a nanogap spin-Hall nano-oscillator (SHNO). Figures 5.1(a) and (b) show the schematic of the SHNO device, which is made of a NiFe (5 nm)/Pt (6 nm) bilayer patterned into a 4 μm disc, on top of which we fabricated needle-shaped gold electrodes with a gap of D = 100 nm between them (Figure 5.1(c)). We characterized these devices

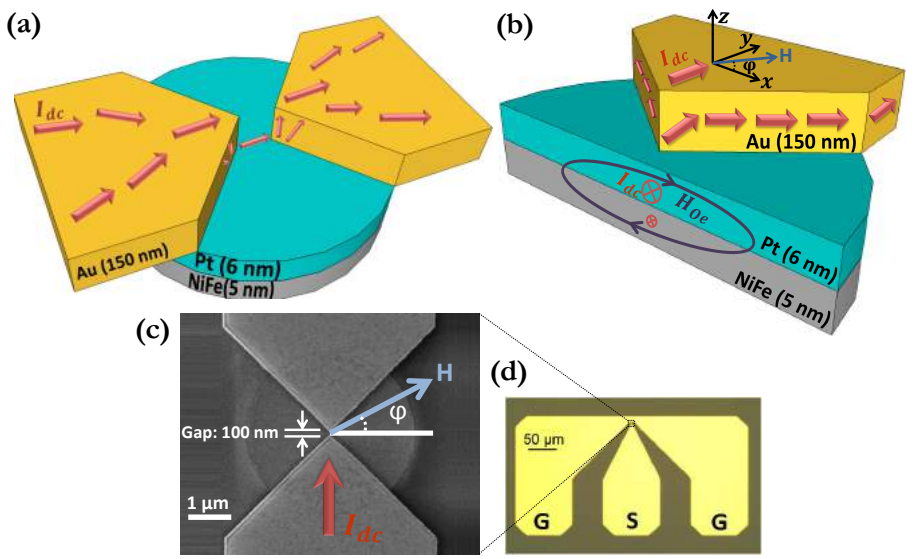

Figure 5.1: (a) Schematic, (b) cross-section, and (c) scanning electron microscopy image of the nanogap SHNO with $d_{\mathrm{disc}} = 4$ μm. (d) Optical microscopy image of the final device and the top contact coplanar waveguides that provide electrical access to the SHNO.

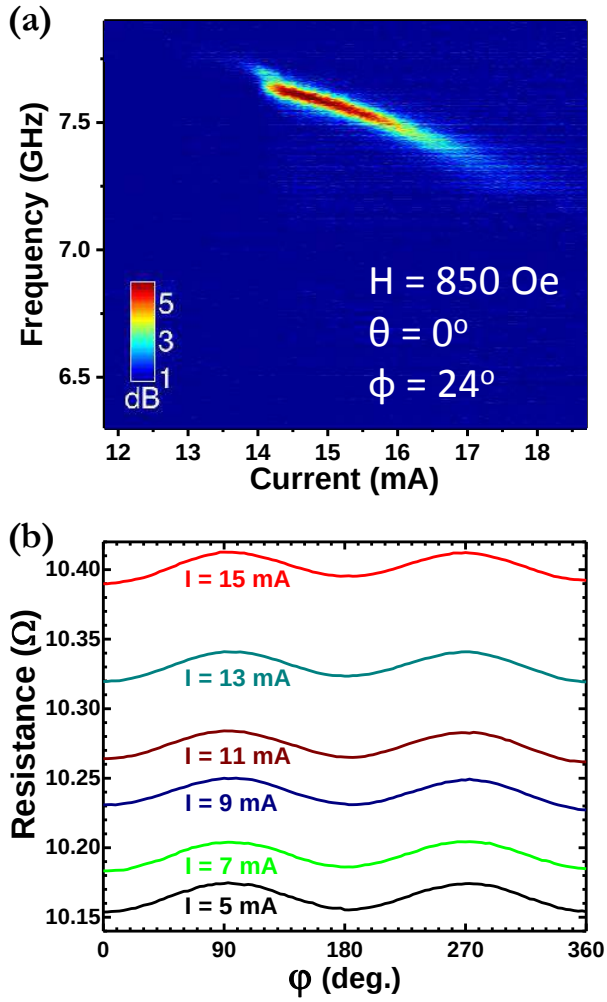

Figure 5.2: (a) Color plot of the power spectral density of auto-oscillation frequency as a function of dc current for a needle-based SHNO device with a gap of D = 100 nm between the needles, with application of an in-plane magnetic field of H_{ext}= 850 Oe at $\theta = 0^{\circ}$ and $\varphi = 24^{\circ}$, and (b) measured AMR curves of the corresponding device for $I_{\text{dc}} = 5$ to 15 mA in steps of 2 mA and an in-plane field of H_{ext}= 5 kOe.

using the full 3D field probe station (Config2) described in Section 3.3.2.

Figure 5.2(a) shows the auto-oscillation frequency output of a needle-based SHNO device with a gap of D = 100 nm between the needles in the form of a color plot of power spectral density as a function of dc current under an in-plane magnetic

field of H_{ext}= 850 Oe at $\theta = 0°$ and $\varphi = 24°$. For AMR measurements, an in-plane magnetic field with a constant magnitude of 0.5 T was applied. Then, by applying a dc current that ranged from 5 mA to 15 mA in steps of 2 mA, we measured the resistance of the device while rotating the magnet (φ) from 0° to 360° in steps of 3°. Figure 5.2(b) illustrates the output curves for the different input currents; the angular dependence is consistent with the AMR effect [166]. The overall resistance increases here with increasing input dc current because of Joule heating, which leads to the material's resistivity increasing with temperature. We also show different

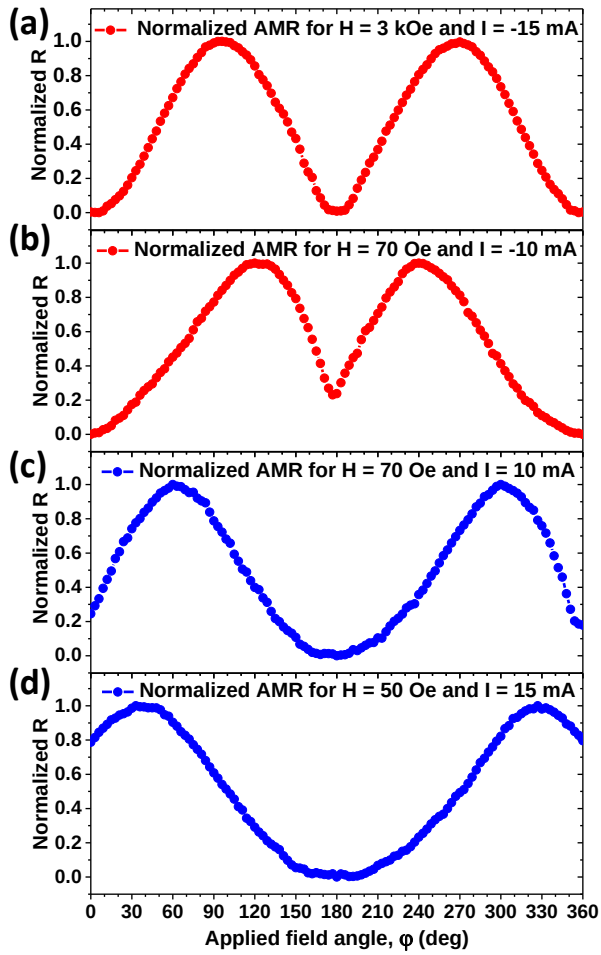

Figure 5.3: Normalized AMR curves for (a) H_{ext} = 3 kOe and I_{dc} = -15 mA, (b) H_{ext} = 70 Oe and I_{dc} = -10 mA, (c) H_{ext} = 70 Oe and I_{dc} = 10 mA, and (d) H_{ext} = 50 Oe and I_{dc} = 15 mA.

value of dc current (I_{dc}) and measure the AMR of the SHNO over a wide range of applied magnetic field, angles, and currents.

Figure 5.3 shows the normalized AMR measurements results with (a) H_{ext} = 3 kOe and I_{dc} = -15 mA, (b) H_{ext} = 70 Oe and I_{dc} = -10 mA, (c) H_{ext} = 70 Oe and I_{dc} = 10 mA, and (d) H_{ext} = 50 Oe and I_{dc} = 15 mA. We interpret the changes in the AMR curves of the lower external fields to be the results of both the Oersted field and heating in the NiFe layer. In the actual AMR data, variation in the magnitude of the field does not have a significant effect on the overall AMR response (e.g., $R_{\parallel}$ and $R_{\perp}$). The changes in the AMR curves of the lower external fields are thus mostly associated with the actual angle of the magnetic field inside the ferromagnetic layer, which is affected by the Oersted field in the NiFe layer, mainly induced by the current in the Pt layer. This is the case because most of the current in the nanogap region flows in the Pt layer (>80%) [38]. At high currents and low external fields, the curves of AMR versus field angle are strongly affected by the induced H_{Oe}, which can be calculated.

To investigate how the current redistributes in the nanogap SHNO device and calculate the associated Joule heating and induced Oersted field, calculations of the current flow in each layer of the SHNO were carried out using COMSOL Multiphysics® simulation software with a detailed three-dimensional finite-element model of the SHNO. In Figure 5.4(a) and (b), we illustrate the temperature map at the top of the NiFe layer and in all layers for I_{dc} = 15 mA, respectively. Figure 5.4(c) also shows the calculated temperature distribution for I_{dc} = 1 to 15 mA in the nanogap SHNO with d_{disc} = 4 μm and a 100-nm gap between the gold needles. Figure 5.5(a) and (b) respectively illustrate the corresponding simulated H_{Oe} at the top of the Pt layer for I_{dc} = 15 mA and the calculated H_{Oe} for I_{dc} = 1 to 15 mA in the middle of the nanogap and top of the NiFe layer of the SHNO with d_{disc} = 4 μm and a 100-nm gap between the gold needles.

In conclusion, we studied the AMR of the nanogap SHNO. We interpreted the changes in the AMR curves of the lower external fields as the result of the actual angle of the magnetic field inside of ferromagnetic layer, as well as of Joule heating induced by the input current. We simulated and calculated the temperature and the Oe field induced by the current flow in the ferromagnetic layer. These results will help us to better understand the dependencies of the spin-wave modes excited in SHNOs.

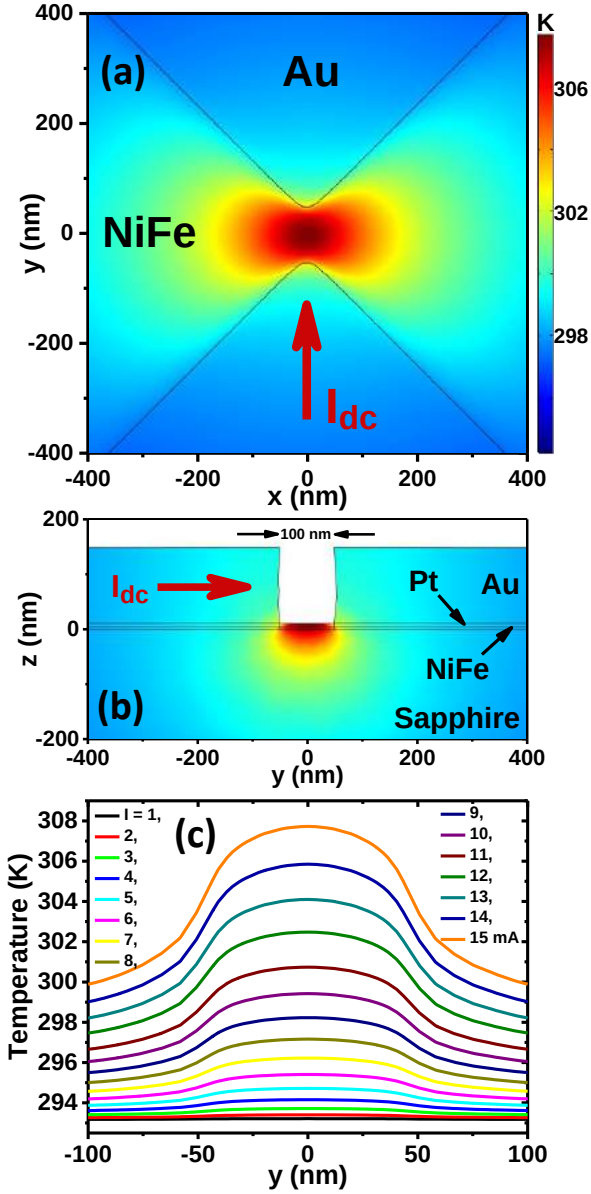

Figure 5.4: Detailed temperature map (a) at the top of NiFe layer, (b) in all layers for $I_{\mathrm{dc}} = 15\ mA$; (c) calculated temperature distribution for $I_{\mathrm{dc}} = 1$ to $15\ mA$ in the nanogap SHNO with $d_{\mathrm{disc}} = 4\ \mu m$ and a 100-nm gap between the gold needles.

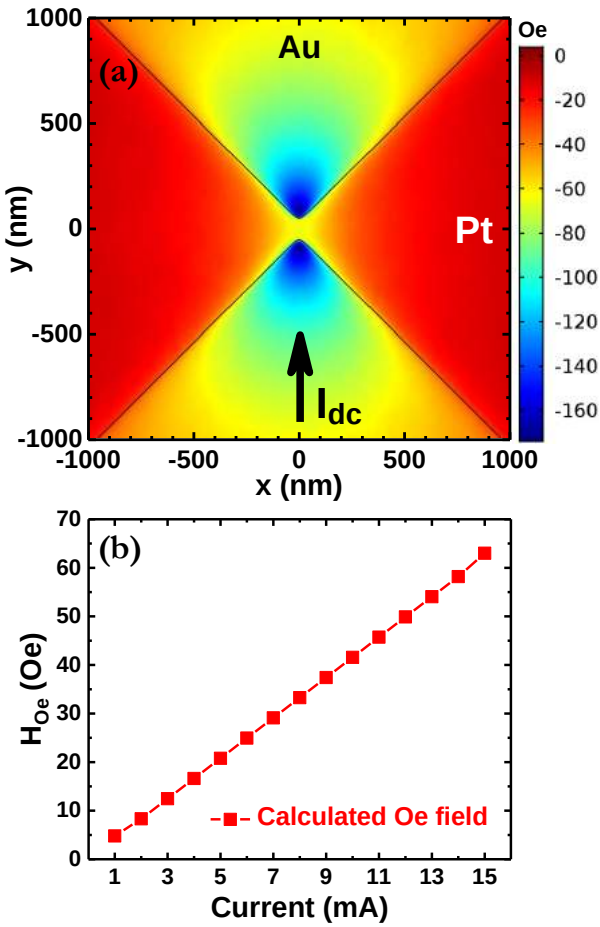

Figure 5.5: (a) Detailed Oe field map at the top of Pt layer for I_{dc} = 15 mA; (b) calculated Oe field for I_{dc} = 1 to 15 mA in the middle of the nanogap SHNO with d_{disc} = 4 μm and D = 100 nm at the middle of the NiFe layer.

5.2 Mapping Out the In-Plane Modes of Nanoconstriction-Based SHNOs

A detailed study of the high-frequency modes of nanoconstriction-based SHNOs under in-plane magnetic fields was presented in Paper IX.

Most recently, a nanoconstriction-based SHNO geometry was demonstrated to have remarkable advantages, such as a much simpler fabrication process and being operational at a lower current than previously described types, such as the needle-based SHNOs described in the previous section [167]. Further, in these nanoconstriction spin Hall oscillators, the mutual synchronization of a chain of multiple SHNOs was demonstrated, which results in a dramatic increase in their output power and a narrower linewidth under the application of approximately 1 T external out-of plane magnetic fields [64]. Furthermore, this type of SHNO is highly promising for future neuromorphic computing devices [12]. The operation of SHNO devices at low fields is desirable in practical applications. In this section, we demonstrate for the first time the different spin-wave modes of nanoconstriction-based SHNOs from experimental microwave signal measurements under a low in-plane magnetic field (H_{IP}), supported by micromagnetic simulation. We investigate the auto-oscillating spin-wave modes in nanoconstriction-based SHNOs as a function of current, external in-plane magnetic field magnitude, and angle.

The stack of NiFe(5nm)/W(5nm) was prepared using dc/rf magnetron sputtering on a rectangular c-plane Sapphire substrate. After patterning an array of mesas using photolithography and Argon ion-milling, the nanoconstrictions with the width of 150 nm were fabricated in the center of the mesas using electron-beam lithography and dry etching. Finally, a conventional ground–signal–ground (GSG) waveguides for electrical access was fabricated by lift-off photolithography and Cu/Au sputtering on top of the nanoconstriction-based SHNO devices.

Figure 5.6(a) shows a schematic of the device structure, the coordinate system,

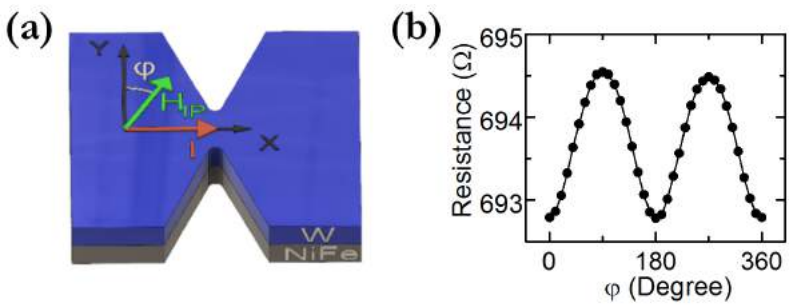

Figure 5.6: (a) Schematic of the nanoconstriction-based SHNO and the configuration of the in-plane field and the current, (b) the angular dependent magnetoresistance of the stack.

and the directions of the applied in-plane field and current. The SHNO's anisotropic magnetoresistance (AMR) is depicted against the in-plane angle of the applied field in Figure 5.6(b). For the microwave measurements, a dc current was injected through the device and passed to the nanoconstriction under the application of a uniform in-plane field. Using the transmission line as described in Section 3.2.2, the output auto-oscillation microwave signal was extracted using a spectrum analyzer after amplification by 35 dB using a low-noise amplifier.

In Figure 5.7(a) we show the power spectral density (PSD) of the SHNO as a function of input dc current and magnetic field at $\varphi = 30°$ under different field

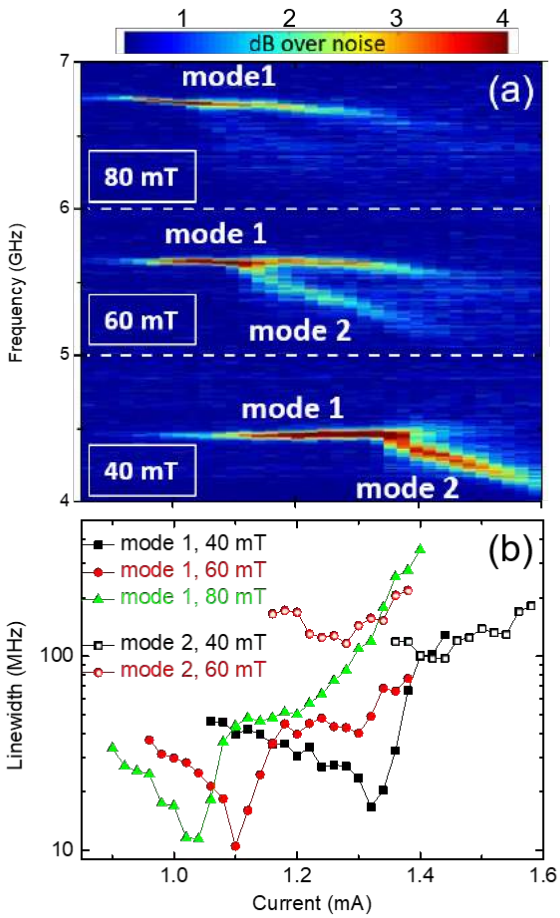

inin

Figure 5.7: (a) Current dependency auto-oscillation PSD at $\varphi = 30°$ for $H_{IP} = 0.04$, 0.06, and 0.08 T and (b) the extracted linewidth. The error bars are smaller than the size of the symbols.

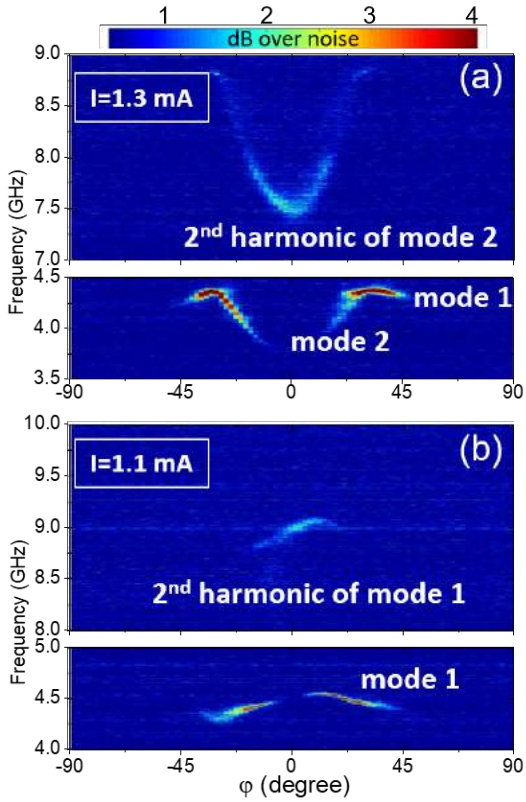

Figure 5.8: PSD map of the fundamental and 2^{nd} harmonic of the modes versus the in-plane angle of the field for $H_{\mathrm{IP}} = 40\ mT$ at (a) I = 1.3 mA, and (b) I = 1.1 mA.

strengths. For $H_{\mathrm{IP}} = 0.08$ T, there is a single spin-wave mode with maximum power around 1 mA which degrades at higher input currents. Decreasing the field to 0.06 T results in the coexistence of a new mode at high currents, the frequency of which depends strongly on the input current. Additionally, decreasing the field lowers both the FMR and auto-oscillation frequencies. Reducing the field further to 0.04 T makes mode 2 dominant at higher currents. Figure 5.7(b) shows the auto-oscillation linewidth of the three spectra extracted by fitting the peaks to Lorentzian function. The linewidth of mode 1 decreases as the current increases until a certain minimum point, where it shows a rapid exponential rise; the linewidth of the second mode is an order of magnitude higher than the first mode for each applied field.

The fundamental and second harmonics of both mode 1 and mode 2, as functions of the in-plane angle with a constant $\mathrm{H_{IP}} = 40$ mT, are plotted in Figure 5.8 (a) and (b) at I = 1.3 mA and 1.1 mA, respectively. Similarly to the PSD maps in Figure 5.7(a), mode 2 was observed at higher currents and disappeared with reduced

current. Unlike mode 1, the frequency of mode 2 strongly depends on the angle and decreases with the angle of the external field. Additionally, the fundamental auto-oscillation modes were not detected electrically around $\varphi = 0°$, because the first derivative of the AMR curve is too small near this angle (Figure 5.6 (b)). However, the second harmonics of both modes have their maximum power around 0°.

In order to investigate the physics behind the dynamical behavior of the SHNOs, a micromagnetic simulation was carried out using MuMax3[168]. The parameters used in the simulations correspond to the stack and include the saturation magnetization and gyromagnetic ratio of NiFe, as well as the spin Hall angle of the tungsten layer, which are the values obtained from the ST-FMR measurement. These parameters

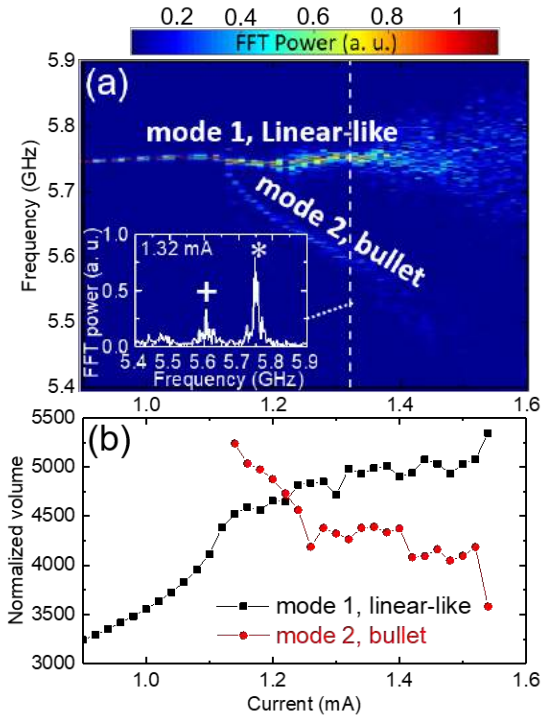

Figure 5.9: (*Simulation*) (a) The FFT power colormap of the total magnetization as a function of frequency and current. Inset: FFT power versus frequency at I = 1.32 mA. Mode 1 and mode 2 are marked with star and plus symbols, respectively. (b) Normalized volume of the linear-like mode (black rectangles) and bullet mode (red circles) versus current. At each current, to obtain the normalized volume as a degree of localization, the FFT amplitude of the local magnetizations in the corresponding mode profile are normalized to one and summed. The error bars are smaller than the size of the symbols.

have been described in Paper IX in detail. The auto-oscillation spectrum and its splitting into two modes can be seen in Figure 5.9(a), in agreement with the experimental observations (Figure 5.7(a)).

We carried out a spatial FFT over the local magnetizations to investigate the type of auto-oscillation modes and determine the spatial distribution of the observed modes. The peak frequency of the FFT curve occurs at $I_{dc} = 1.32$ mA (see inset to Figure 5.9(a)). While mode 1 is more localized on the edges of the nanoconstriction, mode 2 is localized more towards the center (Figure 5.10). Mode 1 is a field-localized linear-like mode confined in the local minima of the internal field (the so-called spin-wave wells) near the edges [167, 169].

To compare the degree of localization of the modes, the FFT amplitudes of the local magnetizations for the corresponding mode profile at each current value are normalized to unity and summed to obtain the normalized volumes of each mode. Following the red doted line in Figure 5.9(b), we see that increasing the current reduces the volume of mode 2, making it more and more localized as we expected. This behavior is observed because the frequency of mode 2 decreases as the current increases (Figure 5.7(a) and Figure 5.9(a)), and so its group velocity and radiation loss reduce. This is the nature of the so-called bullet modes [101, 46, 102, 127], which are nonlinear, nontopological modes localized centrally in a region comparable in size to the nanoconstriction.

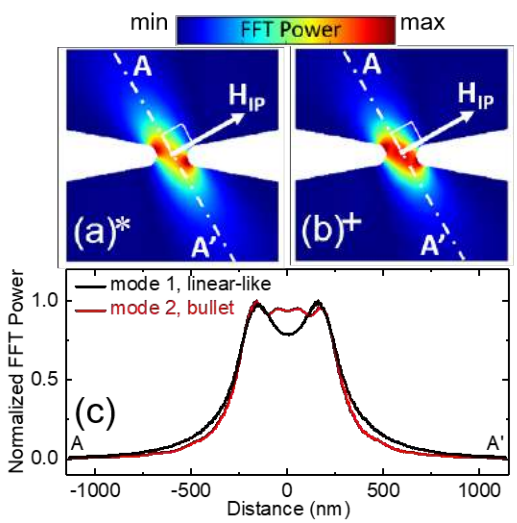

Figure 5.10: (*Simulation*) The mode profile of the FFT peaks is shown in (a) for mode 1 confined at the edges of the nanoconstriction and (b) for mode 2, which is localized more centrally in an area comparable to the constriction size. (c) Mode profiles along the A–A' direction perpendicular to the direction of the external field.

We have presented the dynamic magnetic properties of nanoconstriction-based SHNOs in an in-plane external magnetic field by carrying out microwave measurements and comparing them with the micromagnetic simulation of the structure. We found a linear-like edge mode and a bullet mode confined to the center of the nanoconstriction. Our findings provide a better understanding of the dynamics of nanoconstriction-based SHNOs, which are necessary for subsequent studies of the system to finally use them as nanoscale signal generators.

5.3 In-plane Mutual Synchronization of Nanoconstriction-Based SHNOs

The demonstration of the mutual synchronization of multiple nanoconstriction-based SHNOs is discussed in full in Paper X.

Recently, mutual synchronization of a chain of multiple nanoconstriction-based SHNOs has been demonstrated, resulting in higher output power with improved linewidth [64]. The synchronization was shown to be driven by direct spin-wave (SW) mode overlap, facilitated by the expansion of SW edge modes at large out-of-plane fields close to 1 T. However, such high fields are impractical in most applications. We here demonstrate for the first time the mutual synchronization of SHNOs with in-plane external magnetic fields (H_{IP}) as low as 30 mT.

The SHNO stack, consisting of NiFe(5nm)/Pt(5nm), was prepared and nanoconstrictions with a width of 150 nm were subsequently fabricated. We made different SHNOs with the number of constrictions varying from one to three, with spacing of 300 and 900 nm between the constrictions. Finally, conventional ground–signal–ground (GSG) waveguides for electrical and microwave measurements were fabricated on top of the SHNO nanoconstrictions.

Figure 5.11(a) shows the schematic of a double nanoconstriction-based SHNO from the top view and the configuration of the in-plane external magnetic field (H_{IP}) and the input current. Microwave measurements were carried out using a custom-built setup. A dc current was injected through the nanoconstriction, and the auto-oscillation microwave signal was received by a spectrum analyzer after amplification by 35 dB using a low noise amplifier.

Figure 5.11(b–d) respectively show the auto-oscillation power spectral density (PSD) colormaps against drive current under $\mu_0 H_{IP} = 30$ mT at $\varphi = 38°$, 24°, and 6° from a double nanoconstriction-based SHNO with 150 nm-wide constriction and a spacing of 300 nm. For greater angles, there are two spin-wave modes from the two constrictions (e.g., $\varphi = 38°$ and 24°). However, as shown in Figure 5.11(d), by decreasing the angle, the two modes merge into a single synchronized mode with a power density much higher than in their unsynchronized state. Figure 5.11(e) shows the auto-oscillation linewidth of the three spectra. A clear sign of synchronization is that the linewidth for the smaller angle of $\varphi = 6°$ drops by more than an order of magnitude, as compared to greater angles.

We also investigated the effect of the field direction on the synchronization of the SHNO modes. We measured the angular dependent auto-oscillation PSD of double and triple nanoconstriction-based SHNOs with spacings of 300 and 900 nm at $\mu_0 H_{IP} = 30$ mT and $I_{dc} = 2.8$ mA. Figure 5.12(a) shows the fundamental and second harmonics of the auto-oscillation signal of a single nanoconstriction-based SHNO versus φ. At smaller angles, the fundamental mode could not be detected, while a strong second harmonic appears at smaller angles.

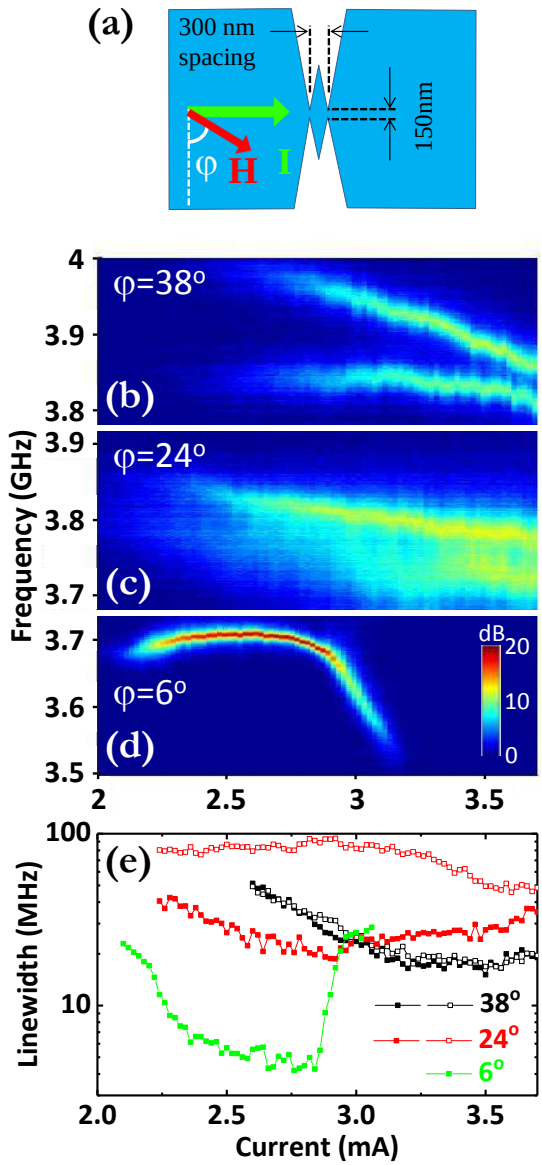

Figure 5.11: (a) Schematic of a double nanoconstriction-based SHNO (top view) with the direction of the in-plane external magnetic field and current in our experiments. Power spectral density map versus current for $\mu_0 H_{IP} = 30$ mT at (b) $\varphi = 38°$, (c) $\varphi = 24°$, and (d) $\varphi = 6°$; (e) the extracted linewidth. The error bars are smaller than the size of the symbols.

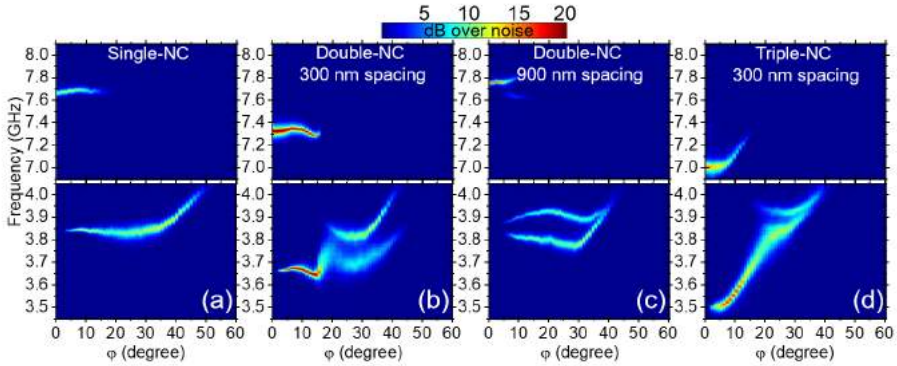

Figure 5.12: Power spectral density map of nanoconstriction-based SHNOs against in-plane field angle for $\mu_0 H_{IP} = 30$ mT and $I_{dc} = 2.8$ mA for (a) a single nanoconstriction and a double nanoconstriction with spacing of (b) 300 nm, (c) 900 nm, and (d) a triple nanoconstriction with spacing of 300 nm.

For the double nanoconstriction-based SHNO with 300 nm spacing (Figure 5.12(b)), each nanoconstriction oscillates independently with different frequencies at greater angles, similar to the current sweeps (Figure5.11(a)). However, at the smaller angles, the modes begin to be synchronized with a much narrower linewidth from a critical angle of ($\varphi_c \simeq 20°$). Besides the synchronization, a fairly strong second harmonic shows up from the same critical angle.

Figure 5.12(c) shows the PSD of a double nanoconstriction-based SHNO with a wider spacing of 900 nm. Compared to the device with the 300 nm spacing, the greater distance between the constrictions destroys the synchronization and pushes φ_c down to $\simeq 5°$. At the same time, a strong second harmonic of the synchronized mode is observed for angles below φ_c, but the fundamental harmonic of the synchronized mode is not detected.

Finally, the PSD for a triple nanoconstriction with 300 nm spacing between the constrictions is plotted in Figure 5.12(d). Similar to Figure 5.12(b), the synchronization is observed at smaller angles, along with a rather strong second harmonic. However, the frequency of the linear-like mode for the triple nanoconstriction shows a steeper angular dependence.

We have presented the mutual synchronization of nanoconstriction-based SHNOs in a weak in-plane field of 30 mT with higher power and lower linewidth. We have also investigated the dependence of the synchronization on the input current and the external magnetic field angle. We studied SHNOs with double and triple nanoconstrictions and with spacings of 300 and 900 nm. The synchronization is achieved at angles below a critical value of φ_c, and this critical angle is greater for the shorter spacing on account of the stronger synchronization between the

nanoconstrictions.

5.4 Magnetic Force Microscopy of Nanoconstriction-Based SHNOs

Following the design and implementation of an MFM system capable of probing an operational nanodevice, as described in Section 3.3.3, I present here some results of experimental testing of this system and the detailed results were presented in Paper II. In this experiment, we probed a nanoconstriction-based SHNO Pt/NiFe bilayer with a constriction width ranging from 80 to 300 nm (Figure 5.13).

In our conventional fabricated devices, short waveguides provide the electrical and microwave access to the nanodevice. However, as explained in Section 3.3.3, there is a limited space under the head of the MFM system; we thus fabricated and used longer waveguides to ensure that the microwave probe can stably and safely contact the waveguides. Figure 5.14 shows a chip of 20 SHNOs mounted on top of the VFM2 in order to apply an external in-plane magnetic field to the device that we want to measure it. For a consistent measurement, the device should be located exactly in the center of the magnetic poles. This will give a uniform field of almost the same magnitude as we set in the software. Further, to apply the field at a certain angle, it would be possible to rotate the chip and then adjust the angle, then making contact with the rf probe with the help of the microscope camera. With the MFM head mounted and with the high-resolution MFM probe calibrated and positioned, we started scanning.

In one of our experiments, we applied an 800 Oe external magnetic field to the device at an angle of $\varphi = 24°$ with an input current of I_{dc} = -6 mA. Figure 5.15(a) depicts the result of atomic force microscopy (AFM) of a nanoconstriction-based SHNO with a width of 300 nm, and Figure 5.15(b) shows the corresponding result

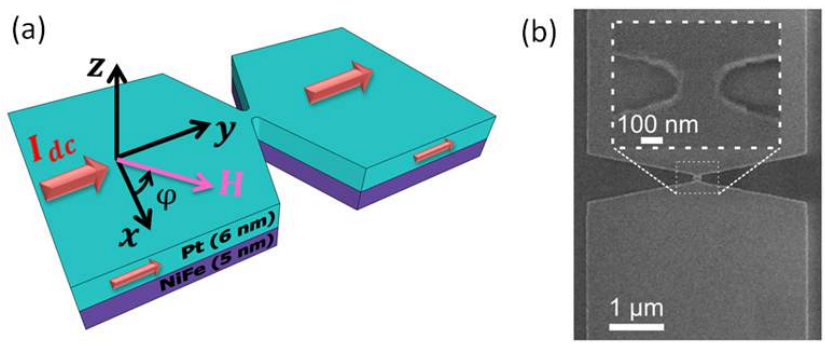

Figure 5.13: (a) Schematic and (b) SEM image of nanoconstriction-based SHNO device.

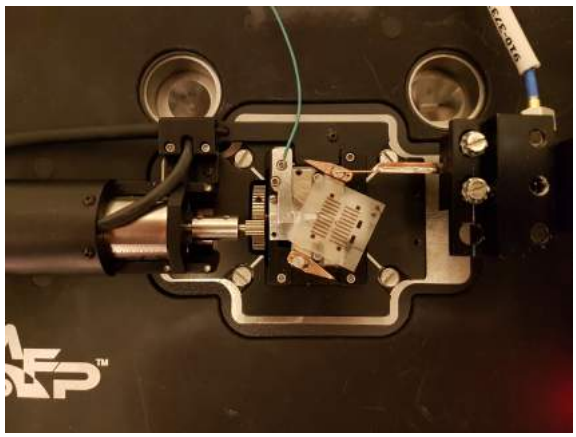

Figure 5.14: Mounted chip of nanoconstriction-based SHNO devices on the variable field module 2 (VFM2) of the MFM system.

from the magnetic channel of the system. We interpret the dark part of the MFM output as a result of high current density, which induces the Oe field, as can be recognized by the MFM technique.

We presented a new method of probing the spatial profile of an operational magnetic nanodevice using magnetic force microscopy (MFM). We developed a MFM system by adding a microwave probe station to provide simultaneous electrical and microwave contact with our fabricated devices during the MFM process. Further, because of the limited space under the MFM head, special devices with longer waveguides were designed and fabricated to ensure stable contact between the device and the microwave probe. Using this MFM system, we scanned operational nanoconstriction-based nano-oscillators. The experimental results show that this method is indeed useful for extracting the spatial profile of an operational magnetic nanodevice.

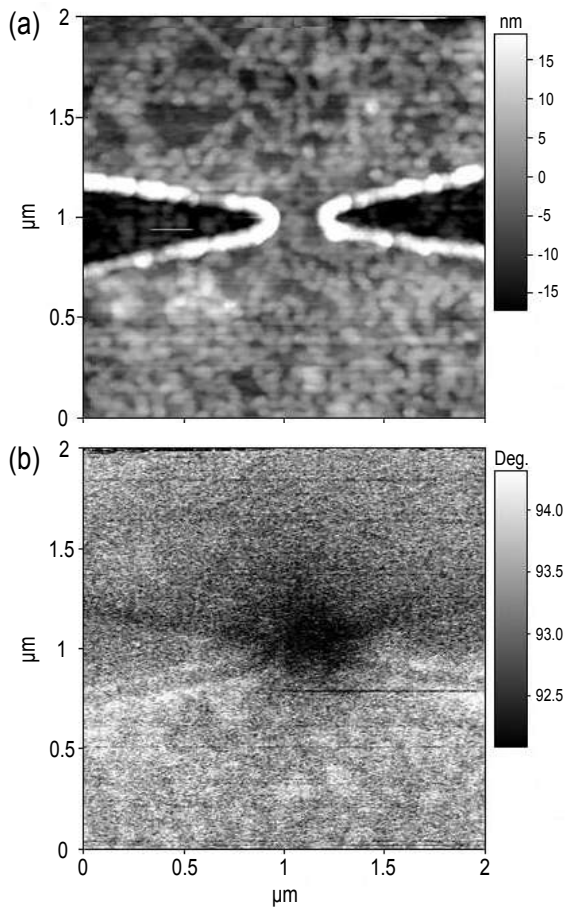

Figure 5.15: AFM and MFM of an operational nanoconstriction-based SHNO with constriction width of D = 300 nm for an applied magnetic field and input current of H = 800 Oe at in-plane angle of $\varphi = 24^{\circ}$ and I_{dc}=-6 mA.

Chapter 6

Conclusion and Future Work

The work presented in this thesis has focused on several experimental approaches for characterizing GMR nanocontact spin torque nano-oscillators, as well as nanogap-based and nanoconstriction-based spin Hall nano-oscillators, and optimizing parameters such as low current oscillations, improved output power at high frequencies, and low-linewidth signals. These improvements were achieved through research into the materials and structure of these devices, as well as by investigating the synchronization phenomena in these nanoscale devices. In particular, most of the results presented here rely on the development of instruments based on both conventional and new experimental techniques of characterizing fabricated devices.

To gain deeper insight into the physical phenomena, the magnetization properties, and the mechanism of magnetization oscillations in these particular devices, both numerical and micromagnetic simulations were employed. Moreover, all of the characterized devices are of interest in microwave applications, as they have the very high stability and high range tunability in their output frequency. Both the design of these devices' structure and the measurement techniques were therefore based on optimizing the capability of these microwave devices for industrial applications.

The further exploration of NC-STNOs and SHNOs is motivated from the point of view of new nanoelectronic application: microwave radio communication and a wide range of sensing platforms should benefit from CMOS-integrable on-chip nanosized oscillators with tunable output frequencies and fast modulation properties. Since the GHz frequencies generated by NC-STNOs and SHNOs can be adjusted by controlling the level of their bias current alone, these devices can be used in telecommunication operations as smart signal generators.

Determining maps of the spin-torque-excited propagating spin-wave modes generated by these devices is scientifically and technically crucial, and would be an interesting measurement case for scanning transmission X-ray microscopy, as well as for quantitative high resolution magnetic force microscopy (MFM). Although there are studies and reports describing observations of these excitations in similar devices,

instrument limitations mean there are still opportunities to work on developing instrument capabilities to achieve more accurate and reliable characterizations. For example, one possible evolution might involve adding a custom assembly of highly homogeneous magnets to the beamline of a synchrotron radiation light source with controllable magnetic field strength and angle, to easily determine the excitation profiles of STNOs and SHNOs.

Bibliography

[1] J. A. C. Bland and B. Heinrich, *Ultrathin Magnetic Structures I: An Introduction to the Electronic, Magnetic and Structural Properties*. Springer Science & Business Media, 2006, vol. 1.

[2] H. Zeng, J. Li, J. P. Liu, Z. L. Wang, and S. Sun, "Exchange-coupled nanocomposite magnets by nanoparticle self-assembly," *Nature*, vol. 420, no. 6914, p. 395, 2002.

[3] A. Hirohata and K. Takanashi, "Future perspectives for spintronic devices," *Journal of Physics D: Applied Physics*, vol. 47, no. 19, p. 193001, 2014.

[4] Z. Sheykhifard, S. M. Mohseni, B. Tork, M. Hajiali, L. Jamilpanah, B. Rahmati, F. Haddadi, M. Hamdi, S. M. Mohseni, M. Mohammadbeigi, A. Ghaderi, S. Erfanifam, M. Dashtdar, F. Feghhi, N. Ansari, S. Pakdel, M. Pourfath, A. Hosseinzadegan, M. Bahreini, S. H. Tavassoli, M. Ranjbar, S. A. H. Banuazizi, S. Chung, J. Åkerman, N. Nikkam, A. Sohrabi, and S. E. Roozmeh, "Magnetic graphene/ni-nano-crystal hybrid for small field magnetoresistive effect synthesized via electrochemical exfoliation/deposition technique," *Journal of Materials Science: Materials in Electronics*, vol. 29, no. 5, pp. 4171–4178, 2018.

[5] J. Åkerman, "Toward a universal memory," *Science*, vol. 308, no. 5721, pp. 508–510, 2005.

[6] J. W. Judy, "Microelectromechanical systems (mems): fabrication, design and applications," *Smart Materials and Structures*, vol. 10, no. 6, p. 1115, 2001.

[7] C. Enkrich, M. Wegener, S. Linden, S. Burger, L. Zschiedrich, F. Schmidt, J. Zhou, T. Koschny, and C. Soukoulis, "Magnetic metamaterials at telecommunication and visible frequencies," *Physical Review Letters*, vol. 95, no. 20, p. 203901, 2005.

[8] M. Díaz-Michelena, "Small magnetic sensors for space applications," *Sensors*, vol. 9, no. 4, pp. 2271–2288, 2009.

[9] Y. Chemla, H. Grossman, Y. Poon, R. McDermott, R. Stevens, M. Alper, and J. Clarke, "Ultrasensitive magnetic biosensor for homogeneous immunoassay,"

Proceedings of the National Academy of Sciences, vol. 97, no. 26, pp. 14 268–14 272, 2000.

[10] D. Issadore, J. Chung, H. Shao, M. Liong, A. A. Ghazani, C. M. Castro, R. Weissleder, and H. Lee, "Ultrasensitive clinical enumeration of rare cells ex vivo using a micro-hall detector," *Science Translational Medicine*, vol. 4, no. 141, pp. 141ra92–141ra92, 2012.

[11] J. P. Liu, E. Fullerton, O. Gutfleisch, and D. J. Sellmyer, *Nanoscale magnetic materials and applications*. Springer, 2009.

[12] J. Torrejon, M. Riou, F. A. Araujo, S. Tsunegi, G. Khalsa, D. Querlioz, P. Bortolotti, V. Cros, K. Yakushiji, A. Fukushima *et al.*, "Neuromorphic computing with nanoscale spintronic oscillators," *Nature*, vol. 547, no. 7664, p. 428, 2017.

[13] M. D. Stiles and A. Zangwill, "Anatomy of spin-transfer torque," *Physical Review B*, vol. 66, no. 1, p. 014407, 2002.

[14] S. Wolf, D. Awschalom, R. Buhrman, J. Daughton, S. Von Molnar, M. Roukes, A. Y. Chtchelkanova, and D. Treger, "Spintronics: a spin-based electronics vision for the future," *Science*, vol. 294, no. 5546, pp. 1488–1495, 2001.

[15] M. N. Baibich, J. M. Broto, A. Fert, F. N. Van Dau, F. Petroff, P. Etienne, G. Creuzet, A. Friederich, and J. Chazelas, "Giant magnetoresistance of (001) fe/(001) cr magnetic superlattices," *Physical Review Letters*, vol. 61, no. 21, p. 2472, 1988.

[16] G. Binasch, P. Grünberg, F. Saurenbach, and W. Zinn, "Enhanced magnetoresistance in layered magnetic structures with antiferromagnetic interlayer exchange," *Physical Review B*, vol. 39, no. 7, p. 4828, 1989.

[17] A. Fert, "Nobel lecture: Origin, development, and future of spintronics," *Reviews of Modern Physics*, vol. 80, no. 4, p. 1517, 2008.

[18] P. A. Grünberg, "Nobel lecture: From spin waves to giant magnetoresistance and beyond," *Reviews of Modern Physics*, vol. 80, no. 4, p. 1531, 2008.

[19] B. N. Engel, J. Åkerman, B. Butcher, R. W. Dave, M. DeHerrera, M. Durlam, G. Grynkewich, J. Janesky, S. V. Pietambaram, N. D. Rizzo, J. M. Slaughter, K. Smith, J. J. Sun, and S. Tehrani, "A 4-mb toggle mram based on a novel bit and switching method," *IEEE Transactions on Magnetics*, vol. 41, no. 1, pp. 132–136, 2005.

[20] "Spin Transfer Technologies," accessed: 2018-02-30. [Online]. Available: www.spintransfer.com/

[21] P. Villard, U. Ebels, D. Houssameddine, J. Katine, D. Mauri, B. Delaet, P. Vincent, M.-C. Cyrille, B. Viala, J.-P. Michel, J. Prouvée, and F. Badets, "A ghz spintronic-based rf oscillator," *IEEE Journal of Solid-State Circuits*, vol. 45, no. 1, pp. 214–223, 2010.

[22] P. Braganca, B. Gurney, B. Wilson, J. Katine, S. Maat, and J. Childress, "Nanoscale magnetic field detection using a spin torque oscillator," *Nanotechnology*, vol. 21, no. 23, p. 235202, 2010.

[23] T. Schneider, A. Serga, B. Leven, B. Hillebrands, R. Stamps, and M. Kostylev, "Realization of spin-wave logic gates," *Applied Physics Letters*, vol. 92, no. 2, p. 022505, 2008.

[24] G. Csaba, Á. Papp, and W. Porod, "Perspectives of using spin waves for computing and signal processing," *Physics Letters A*, vol. 381, no. 17, pp. 1471–1476, 2017.

[25] E. Dahlman, G. Mildh, S. Parkvall, J. Peisa, J. Sachs, Y. Selén, and J. Sköld, "5g wireless access: requirements and realization," *IEEE Communications Magazine*, vol. 52, no. 12, pp. 42–47, 2014.

[26] J. Katine and E. E. Fullerton, "Device implications of spin-transfer torques," *Journal of Magnetism and Magnetic Materials*, vol. 320, no. 7, pp. 1217–1226, 2008.

[27] T. Silva and W. Rippard, "Developments in nano-oscillators based upon spin-transfer point-contact devices," *Journal of Magnetism and Magnetic Materials*, vol. 320, no. 7, pp. 1260–1271, 2008.

[28] J.-V. Kim, "Spin-torque oscillators," in *Solid State Physics*. Elsevier, 2012, vol. 63, pp. 217–294.

[29] R. K. Dumas, S. R. Sani, S. M. Mohseni, E. Iacocca, Y. Pogoryelov, P. K. Muduli, S. Chung, P. Dürrenfeld, and J. Åkerman, "Recent advances in nanocontact spin-torque oscillators," *IEEE Transactions on Magnetics*, vol. 50, no. 6, pp. 1–7, 2014.

[30] T. Chen, R. K. Dumas, A. Eklund, P. K. Muduli, A. Houshang, A. A. Awad, P. Dürrenfeld, B. G. Malm, A. Rusu, and J. Åkerman, "Spin-torque and spin-hall nano-oscillators," *Proceedings of the IEEE*, vol. 104, no. 10, pp. 1919–1945, 2016.

[31] N. Locatelli, V. Cros, and J. Grollier, "Spin-torque building blocks," *Nature Materials*, vol. 13, no. 1, p. 11, 2014.

[32] T. Chen, A. Eklund, S. Sani, S. Rodriguez, B. G. Malm, J. Åkerman, and A. Rusu, "Integration of gmr-based spin torque oscillators and cmos circuitry," *Solid-State Electronics*, vol. 111, pp. 91–99, 2015.

[33] M. Zahedinejad, H. Mazraati, H. Fulara, J. Yue, S. Jiang, A. Awad, and J. Åkerman, "Cmos compatible w/cofeb/mgo spin hall nano-oscillators with wide frequency tunability," *Applied Physics Letters*, vol. 112, no. 13, p. 132404, 2018.

[34] T. Chen, P. Dürrenfeld, S. Rodriguez, J. Åkerman, and A. Rusu, "A highly tunable microwave oscillator based on mtj sto technology," *Microwave and Optical Technology Letters*, vol. 56, no. 9, pp. 2092–2095, 2014.

[35] J. C. Slonczewski, "Current-driven excitation of magnetic multilayers," *Journal of Magnetism and Magnetic Materials*, vol. 159, no. 1, pp. L1–L7, 1996.

[36] L. Berger, "Emission of spin waves by a magnetic multilayer traversed by a current," *Physical Review B*, vol. 54, no. 13, p. 9353, 1996.

[37] D. C. Ralph and M. D. Stiles, "Spin transfer torques," *Journal of Magnetism and Magnetic Materials*, vol. 320, no. 7, pp. 1190–1216, 2008.

[38] L. Liu, T. Moriyama, D. Ralph, and R. Buhrman, "Spin-torque ferromagnetic resonance induced by the spin hall effect," *Physical Review Letters*, vol. 106, no. 3, p. 036601, 2011.

[39] H. Mazraati, S. Chung, A. Houshang, M. Dvornik, L. Piazza, F. Qejvanaj, S. Jiang, T. Q. Le, J. Weissenrieder, and J. Åkerman, "Low operational current spin hall nano-oscillators based on nife/w bilayers," *Applied Physics Letters*, vol. 109, no. 24, p. 242402, 2016.

[40] S. Tacchi, R. Troncoso, M. Ahlberg, G. Gubbiotti, M. Madami, J. Åkerman, and P. Landeros, "Interfacial dzyaloshinskii-moriya interaction in pt/cofeb films: effect of the heavy-metal thickness," *Physical review letters*, vol. 118, no. 14, p. 147201, 2017.

[41] V. Kruglyak, S. Demokritov, and D. Grundler, "Magnonics," *Journal of Physics D: Applied Physics*, vol. 43, no. 26, p. 264001, 2010.

[42] B. Bransden and C. Joachain, "Physics of atoms and molecules longman scientific & technical," 1983.

[43] M. Getzlaff, *Fundamentals of magnetism*. Springer Science & Business Media, 2007.

[44] C. Kittel, *Introduction to solid state physics*. Wiley, 2005.

[45] R. Liu, W. Lim, and S. Urazhdin, "Spectral characteristics of the microwave emission by the spin hall nano-oscillator," *Physical Review Letters*, vol. 110, no. 14, p. 147601, 2013.

[46] V. E. Demidov, S. Urazhdin, H. Ulrichs, V. Tiberkevich, A. Slavin, D. Baither, G. Schmitz, and S. O. Demokritov, "Magnetic nano-oscillator driven by pure spin current," *Nature Materials*, vol. 11, no. 12, pp. 1028–1031, 2012.

[47] T. Miyazaki and N. Tezuka, "Giant magnetic tunneling effect in fe/al2o3/fe junction," *Journal of Magnetism and Magnetic Materials*, vol. 139, no. 3, pp. L231–L234, 1995.

[48] J. S. Moodera, L. R. Kinder, T. M. Wong, and R. Meservey, "Large magnetoresistance at room temperature in ferromagnetic thin film tunnel junctions," *Physical Review Letters*, vol. 74, no. 16, p. 3273, 1995.

[49] W. Thomson, "On the electro-dynamic qualities of metals:–effects of magnetization on the electric conductivity of nickel and of iron," *Proceedings of the Royal Society of London*, vol. 8, pp. 546–550, 1856.

[50] E. Myers, D. Ralph, J. Katine, R. Louie, and R. Buhrman, "Current-induced switching of domains in magnetic multilayer devices," *Science*, vol. 285, no. 5429, pp. 867–870, 1999.

[51] S. Bonetti, "Magnetization dynamics in nano-contact spin torque oscillators: Solitonic bullets and propagating spin waves," Ph.D. dissertation, KTH, 2010.

[52] S. Yuasa, T. Nagahama, A. Fukushima, Y. Suzuki, and K. Ando, "Giant room-temperature magnetoresistance in single-crystal fe/mgo/fe magnetic tunnel junctions," *Nature Materials*, vol. 3, no. 12, p. 868, 2004.

[53] D. D. Djayaprawira, K. Tsunekawa, M. Nagai, H. Maehara, S. Yamagata, N. Watanabe, S. Yuasa, Y. Suzuki, and K. Ando, "230% room-temperature magnetoresistance in cofeb/ mgo/ cofeb magnetic tunnel junctions," *Applied Physics Letters*, vol. 86, no. 9, p. 092502, 2005.

[54] Y. B. Bazaliy, B. Jones, and S.-C. Zhang, "Modification of the landau-lifshitz equation in the presence of a spin-polarized current in colossal-and giant-magnetoresistive materials," *Physical Review B*, vol. 57, no. 6, p. R3213, 1998.

[55] J. Slonczewski, "Excitation of spin waves by an electric current," *Journal of Magnetism and Magnetic Materials*, vol. 195, no. 2, pp. L261–L268, 1999.

[56] S. Bonetti, P. Muduli, F. Mancoff, and J. Åkerman, "Spin torque oscillator frequency versus magnetic field angle: The prospect of operation beyond 65 ghz," *Applied Physics Letters*, vol. 94, no. 10, p. 102507, 2009.

[57] E. H. Hall, "On a new action of the magnet on electric currents," *American Journal of Mathematics*, vol. 2, no. 3, pp. 287–292, 1879.

[58] E. Hall, "On the" rotational coefficient" in nickel and cobalt," *Proceedings of the Physical Society of London*, vol. 4, no. 1, p. 325, 1880.

[59] J. Hirsch, "Spin hall effect," *Physical Review Letters*, vol. 83, no. 9, p. 1834, 1999.

[60] J. Sinova, D. Culcer, Q. Niu, N. Sinitsyn, T. Jungwirth, and A. MacDonald, "Universal intrinsic spin hall effect," *Physical Review Letters*, vol. 92, no. 12, p. 126603, 2004.

[61] V. E. Demidov, S. Urazhdin, E. Edwards, M. D. Stiles, R. D. McMichael, and S. O. Demokritov, "Control of magnetic fluctuations by spin current," *Physical Review Letters*, vol. 107, no. 10, p. 107204, 2011.

[62] L. Liu, O. Lee, T. Gudmundsen, D. Ralph, and R. Buhrman, "Current-induced switching of perpendicularly magnetized magnetic layers using spin torque from the spin hall effect," *Physical Review Letters*, vol. 109, no. 9, p. 096602, 2012.

[63] A. Hoffmann, "Spin hall effects in metals," *IEEE Transactions on Magnetics*, vol. 49, no. 10, pp. 5172–5193, 2013.

[64] A. Awad, P. Dürrenfeld, A. Houshang, M. Dvornik, E. Iacocca, R. Dumas, and J. Åkerman, "Long-range mutual synchronization of spin hall nano-oscillators," *Nature Physics*, vol. 13, no. 3, p. 292, 2017.

[65] C.-F. Pai, L. Liu, Y. Li, H. Tseng, D. Ralph, and R. Buhrman, "Spin transfer torque devices utilizing the giant spin hall effect of tungsten," *Applied Physics Letters*, vol. 101, no. 12, p. 122404, 2012.

[66] S. A. H. Banuazizi, S. R. Sani, A. Eklund, M. M. Naiini, S. M. Mohseni, S. Chung, P. Dürrenfeld, B. G. Malm, and J. Åkerman, "Order of magnitude improvement of nano-contact spin torque nano-oscillator performance," *Nanoscale*, vol. 9, pp. 1896–1900, 2017.

[67] S. Redjai Sani, "Fabrication and characterization of nanocontact spin-torque oscillators," Ph.D. dissertation, KTH Royal Institute of Technology, 2013.

[68] A. Tulapurkar, Y. Suzuki, A. Fukushima, H. Kubota, H. Maehara, K. Tsunekawa, D. Djayaprawira, N. Watanabe, and S. Yuasa, "Spin-torque diode effect in magnetic tunnel junctions," *Nature*, vol. 438, no. 7066, pp. 339–342, 2005.

[69] J. Sankey, P. Braganca, A. Garcia, I. Krivorotov, R. Buhrman, and D. Ralph, "Spin-transfer-driven ferromagnetic resonance of individual nanomagnets," *Physical Review Letters*, vol. 96, no. 22, p. 227601, 2006.

[70] J. N. Kupferschmidt, S. Adam, and P. W. Brouwer, "Theory of the spin-torque-driven ferromagnetic resonance in a ferromagnet/normal-metal/ferromagnet structure," *Physical Review B*, vol. 74, no. 13, p. 134416, 2006.

[71] W. Chen, J.-M. Beaujour, G. De Loubens, A. Kent, and J. Sun, "Spin-torque driven ferromagnetic resonance of co/ ni synthetic layers in spin valves," *Applied Physics Letters*, vol. 92, no. 1, p. 012507, 2008.

[72] H. Mazraati, T. Q. Le, A. A. Awad, S. Chung, E. Hirayama, S. Ikeda, F. Matsukura, H. Ohno, and J. Åkerman, "Free-and reference-layer magnetization modes versus in-plane magnetic field in a magnetic tunnel junction with perpendicular magnetic easy axis," *Physical Review B*, vol. 94, no. 10, p. 104428, 2016.

[73] S. A. H. Banuazizi and J. Åkerman, "Microwave probe stations with three-dimensional control of the magnetic field to study high-frequency dynamics in nanoscale devices," *Review of Scientific Instruments*, 2018, DOI:10.1063/1.5032219.

[74] S. He, Z. Meng, L. Huang, L. K. Yap, T. Zhou, and C. Panagopoulos, "A versatile rotary-stage high frequency probe station for studying magnetic films and devices," *Review of Scientific Instruments*, vol. 87, no. 7, p. 074704, 2016.

[75] *GMW Projected Field Electromagnet 5201*, accessed February 6, 2017, www.gmw.com/electromagnets/Miniature/5201/5201.html.

[76] J. Li, E. Jin, H. Son, A. Tan, W. Cao, C. Hwang, and Z. Qiu, "Design of a vector magnet for the measurements of anisotropic magnetoresistance and rotational magneto-optic kerr effect," *Review of Scientific Instruments*, vol. 83, no. 3, p. 033906, 2012.

[77] *JANIS Magneto-Optical Micro-manipulated Probe System*, accessed February 6, 2017, www.janis.com/ProbeStationWithElectromagnet.aspx.

[78] *GMW Dipole Electromagnet 3470*, accessed February 6, 2017, www.gmw.com/electromagnets/dipole/3470/3470.html.

[79] *GMW Dipole Electromagnet 3470 (Specification)*, accessed February 6, 2017, www.gmw.com/electromagnets/dipole/3470/3470_Specs.html.

[80] S. Trout, "Use of helmholtz coils for magnetic measurements," *IEEE Transactions on Magnetics*, vol. 24, no. 4, pp. 2108–2111, 1988.

[81] C. Hwang, C. Chen, P. Chang, H. Chen, C. Chang, and M. Huang, "A permanent magnet device for producing variable high magnetic field in three dimensions," *Journal of Magnetism and Magnetic Materials*, vol. 209, no. 1-3, pp. 169–172, 2000.

[82] C. Hwang, C. Chen, C. Chang, C. Liu, F. Lin, B. Wang, and R. Wahrer, "A novel superconducting octupole magnet for photon scattering experiments," *Journal of Magnetism and Magnetic Materials*, vol. 239, no. 1-3, pp. 586–590, 2002.

[83] E. Arenholz and S. O. Prestemon, "Octupole magnet for soft x ray magnetic dichroism experiments: Design and performance," in *AIP Conference Proceedings*, vol. 705, no. 1. AIP, 2004, pp. 1170–1173.

[84] *F3A Magnetic Transducer*, accessed February 6, 2017, www.senis.ch/products/magnetometers/analog-magnetic-field-transducers/f3a-magnetic-transducer-with-fully-integrated-1-2-3-axis.

[85] *Transverse Probe Holder*, accessed February 6, 2017, www.gmw.com/magnetic_measurements/Senis/3-axis-acc.html.

[86] S. Chung, Q. T. Le, M. Ahlberg, M. Weigand, I. Bykova, A. A. Awad, H. Mazraati, A. Houshang, S. Jiang, T. Nguyen, E. Goering, G. Schütz, J. Gräfe, and J. Åkerman, "Direct observation of magnetic droplet solitons in all-perpendicular spin torque nano-oscillators," *arXiv preprint arXiv:1707.01595*, 2017.

[87] A. Eklund, S. Bonetti, S. R. Sani, S. M. Mohseni, J. Persson, S. Chung, S. A. H. Banuazizi, E. Iacocca, M. Östling, J. Åkerman, and B. G. Malm, "Dependence of the colored frequency noise in spin torque oscillators on current and magnetic field," *Applied Physics Letters*, vol. 104, no. 9, p. 092405, 2014.

[88] L. M. Belova, O. Hellwig, E. Dobisz, and E. Dan Dahlberg, "Rapid preparation of electron beam induced deposition co magnetic force microscopy tips with 10 nm spatial resolution," *Review of Scientific Instruments*, vol. 83, no. 9, p. 093711, 2012.

[89] "MFP-3D-SA-AFM," accessed: 2017-10-30. [Online]. Available: www.asylumresearch.com/Products/MFP3DClassic/MFP3DClassic.shtml

[90] "VFM2 Variable Field Module for Magnetic AFM Applications," accessed: 2017-10-30. [Online]. Available: www.asylumresearch.com/Products/VFM2/VFM2.shtml

[91] W. Rippard, M. Pufall, S. Kaka, S. Russek, and T. Silva, "Direct-current induced dynamics in c o 90 f e 10/n i 80 f e 20 point contacts," *Physical Review Letters*, vol. 92, no. 2, p. 027201, 2004.

[92] P. Muduli, O. Heinonen, and J. Åkerman, "Intrinsic frequency doubling in a magnetic tunnel junction–based spin torque oscillator," *Journal of Applied Physics*, vol. 110, no. 7, p. 076102, 2011.

[93] M. Pufall, W. Rippard, S. Kaka, T. Silva, and S. Russek, "Frequency modulation of spin-transfer oscillators," *Applied Physics Letters*, vol. 86, no. 8, p. 082506, 2005.

[94] M. Manfrini, T. Devolder, J.-V. Kim, P. Crozat, N. Zerounian, C. Chappert, W. Van Roy, L. Lagae, G. Hrkac, and T. Schrefl, "Agility of vortex-based nanocontact spin torque oscillators," *Applied Physics Letters*, vol. 95, no. 19, p. 192507, 2009.

[95] P. K. Muduli, Y. Pogoryelov, S. Bonetti, G. Consolo, F. Mancoff, and J. Åkerman, "Nonlinear frequency and amplitude modulation of a nanocontact-based spin-torque oscillator," *Physical Review B*, vol. 81, no. 14, p. 140408, 2010.

[96] P. Muduli, Y. Pogoryelov, Y. Zhou, F. Mancoff, and J. Åkerman, "Spin torque oscillators and rf currents–modulation, locking, and ringing," *Integrated Ferroelectrics*, vol. 125, no. 1, pp. 147–154, 2011.

[97] Y. Pogoryelov, P. Muduli, S. Bonetti, E. Iacocca, F. Mancoff, and J. Åkerman, "Frequency modulation of spin torque oscillator pairs," *Applied Physics Letters*, vol. 98, no. 19, p. 192501, 2011.

[98] Y. Pogoryelov, P. Muduli, S. Bonetti, F. Mancoff, and J. Åkerman, "Spin-torque oscillator linewidth narrowing under current modulation," *Applied Physics Letters*, vol. 98, no. 19, p. 192506, 2011.

[99] R. Sharma, N. Sisodia, E. Iacocca, A. A. Awad, J. Åkerman, and P. Muduli, "A high-speed single sideband generator using a magnetic tunnel junction spin torque nano-oscillator," *Scientific Reports*, vol. 7, no. 1, p. 13422, 2017.

[100] P. Dürrenfeld, Y. Xu, J. Åkerman, and Y. Zhou, "Controlled skyrmion nucleation in extended magnetic layers using a nanocontact geometry," *Physical Review B*, vol. 96, no. 5, p. 054430, 2017.

[101] A. Slavin and V. Tiberkevich, "Spin wave mode excited by spin-polarized current in a magnetic nanocontact is a standing self-localized wave bullet," *Physical Review Letters*, vol. 95, no. 23, p. 237201, 2005.

[102] S. Bonetti, V. Tiberkevich, G. Consolo, G. Finocchio, P. Muduli, F. Mancoff, A. Slavin, and J. Åkerman, "Experimental evidence of self-localized and propagating spin wave modes in obliquely magnetized current-driven nanocontacts," *Physical Review Letters*, vol. 105, no. 21, p. 217204, 2010.

[103] V. E. Demidov, S. Urazhdin, and S. O. Demokritov, "Direct observation and mapping of spin waves emitted by spin-torque nano-oscillators," *Nature Materials*, vol. 9, no. 12, pp. 984–988, 2010.

[104] M. Madami, S. Bonetti, G. Consolo, S. Tacchi, G. Carlotti, G. Gubbiotti, F. Mancoff, M. A. Yar, and J. Åkerman, "Direct observation of a propagating spin wave induced by spin-transfer torque," *Nature Nanotechnology*, vol. 6, no. 10, pp. 635–638, 2011.

[105] R. K. Dumas, E. Iacocca, S. Bonetti, S. Sani, S. M. Mohseni, A. Eklund, J. Persson, O. Heinonen, and J. Åkerman, "Spin-wave-mode coexistence on the nanoscale: a consequence of the oersted-field-induced asymmetric energy landscape," *Physical Review Letters*, vol. 110, no. 25, p. 257202, 2013.

[106] S. M. Mohseni, S. R. Sani, J. Persson, T. N. A. Nguyen, S. Chung, Y. Pogoryelov, P. K. Muduli, E. Iacocca, A. Eklund, R. K. Dumas, S. Bonetti, A. Deac, M. A. Hoefer, and J. Åkerman, "Spin torque–generated magnetic droplet solitons," *Science*, vol. 339, no. 6125, pp. 1295–1298, 2013.

[107] S. Sani, J. Persson, S. M. Mohseni, Y. Pogoryelov, P. Muduli, A. Eklund, G. Malm, M. Käll, A. Dmitriev, and J. Åkerman, "Mutually synchronized bottom-up multi-nanocontact spin–torque oscillators," *Nature Communications*, vol. 4, no. 2731, p. 2731, 2013.

[108] E. Iacocca, P. Dürrenfeld, O. Heinonen, J. Åkerman, and R. K. Dumas, "Mode-coupling mechanisms in nanocontact spin-torque oscillators," *Physical Review B*, vol. 91, no. 10, p. 104405, 2015.

[109] A. Houshang, E. Iacocca, P. Dürrenfeld, S. Sani, J. Åkerman, and R. Dumas, "Spin-wave-beam driven synchronization of nanocontact spin-torque oscillators," *Nature Nanotechnology*, vol. 11, no. 3, pp. 280–286, 2016.

[110] S. Bonetti and J. Åkerman, "Nano-contact spin-torque oscillators as magnonic building blocks," in *Magnonics*. Springer, 2013, pp. 177–187.

[111] Y. Yin, F. Pan, M. Ahlberg, M. Ranjbar, P. Dürrenfeld, A. Houshang, M. Haidar, L. Bergqvist, Y. Zhai, R. K. Dumas *et al.*, "Tunable permalloy-based films for magnonic devices," *Physical Review B*, vol. 92, no. 2, p. 024427, 2015.

[112] F. Albert, N. Emley, E. Myers, D. Ralph, and R. Buhrman, "Quantitative study of magnetization reversal by spin-polarized current in magnetic multilayer nanopillars," *Physical Review Letters*, vol. 89, no. 22, p. 226802, 2002.

[113] S. Mangin, Y. Henry, D. Ravelosona, J. Katine, and E. E. Fullerton, "Reducing the critical current for spin-transfer switching of perpendicularly magnetized nanomagnets," *Applied Physics Letters*, vol. 94, no. 1, p. 012502, 2009.

[114] J. M. Shaw, H. T. Nembach, and T. Silva, "Roughness induced magnetic inhomogeneity in co/ni multilayers: Ferromagnetic resonance and switching properties in nanostructures," *Journal of Applied Physics*, vol. 108, no. 9, p. 093922, 2010.

[115] Y. Zhou, S. Bonetti, C. Zha, and J. Åkerman, "Zero-field precession and hysteretic threshold currents in a spin torque nano device with tilted polarizer," *New Journal of Physics*, vol. 11, no. 10, p. 103028, 2009.

[116] Y. Zhang, H. Zhao, A. Lyle, P. A. Crowell, and J.-P. Wang, "High power and low critical current spin torque oscillation from a magnetic tunnel junction with a built-in hard axis polarizer," *Applied Physics Letters*, vol. 100, no. 3, p. 032405, 2012.

[117] C. Thirion, W. Wernsdorfer, and D. Mailly, "Switching of magnetization by nonlinear resonance studied in single nanoparticles," *Nature Materials*, vol. 2, no. 8, pp. 524–527, 2003.

[118] G. Woltersdorf and C. H. Back, "Microwave assisted switching of single domain ni 80 fe 20 elements," *Physical Review Letters*, vol. 99, no. 22, p. 227207, 2007.

[119] H. Nembach, H. Bauer, J. Shaw, M. Schneider, and T. Silva, "Microwave assisted magnetization reversal in single domain nanoelements," *Applied Physics Letters*, vol. 95, no. 6, p. 062506, 2009.

[120] D. Houssameddine, U. Ebels, B. Delaët, B. Rodmacq, I. Firastrau, F. Ponthenier, M. Brunet, C. Thirion, J.-P. Michel, L. Prejbeanu-Buda, M.-C. Cyrille, R. O, and B. Dieny, "Spin-torque oscillator using a perpendicular polarizer and a planar free layer," *Nature Materials*, vol. 6, no. 6, pp. 447–453, 2007.

[121] J. Xiao, A. Zangwill, and M. Stiles, "Boltzmann test of slonczewski's theory of spin-transfer torque," *Physical Review B*, vol. 70, no. 17, p. 172405, 2004.

[122] V. Tiberkevich, J.-V. Kim, and A. Slavin, "Microwave power generated by a spin-torque oscillator in the presence of noise," *Applied Physics Letters*, vol. 91, no. 19, p. 192506, 2007.

[123] C. Zha, Y. Fang, J. Nogués, and J. Åkerman, "Improved magnetoresistance through spacer thickness optimization in tilted pseudo spin valves based on l 1 0 (111)-oriented feptcu fixed layers," *Journal of Applied Physics*, vol. 106, no. 5, p. 053909, 2009.

[124] M. Fazlali, M. Dvornik, E. Iacocca, P. Dürrenfeld, M. Haidar, J. Åkerman, and R. K. Dumas, "Homodyne-detected ferromagnetic resonance of in-plane magnetized nanocontacts: Composite spin-wave resonances and their excitation mechanism," *Physical Review B*, vol. 93, no. 13, p. 134427, 2016.

[125] T. J. Silva and W. H. Rippard, "Developments in nano-oscillators based upon spin-transfer point-contact devices," *Journal of Magnetism and Magnetic Materials*, vol. 320, no. 7, pp. 1260–1271, 2008.

[126] W. Rippard, M. Pufall, S. Kaka, T. Silva, and S. Russek, "Current-driven microwave dynamics in magnetic point contacts as a function of applied field angle," *Physical Review B*, vol. 70, no. 10, p. 100406, 2004.

[127] S. Bonetti, V. Puliafito, G. Consolo, V. S. Tiberkevich, A. N. Slavin, and J. Åkerman, "Power and linewidth of propagating and localized modes in nanocontact spin-torque oscillators," *Physical Review B*, vol. 85, no. 17, p. 174427, 2012.

[128] S. R. Sani, J. Persson, S. Mohseni, V. Fallahi, and J. Åkerman, "Current induced vortices in multi-nanocontact spin-torque devices," *Journal of Applied Physics*, vol. 109, no. 7, p. 07C913, 2011.

[129] S. M. Mohseni, S. R. Sani, J. Persson, T. Anh Nguyen, S. Chung, Y. Pogoryelov, and J. Åkerman, "High frequency operation of a spin-torque oscillator at low field," *Physica Status Solidi (RRL)*, vol. 5, no. 12, pp. 432–434, 2011.

[130] F. Mancoff, N. Rizzo, B. Engel, and S. Tehrani, "Area dependence of high-frequency spin-transfer resonance in giant magnetoresistance contacts up to 300 nm diameter," *Applied Physics Letters*, vol. 88, no. 11, p. 2507, 2006.

[131] Z. Wei and M. Tsoi, "Probing wavenumbers of current-induced excitations in point-contact experiments," *Nanotechnology, Science and Applications*, vol. 3, p. 17, 2010.

[132] S. Petit-Watelot, R. Otxoa, and M. Manfrini, "Electrical properties of magnetic nanocontact devices computed using finite-element simulations," *Applied Physics Letters*, vol. 100, no. 8, p. 083507, 2012.

[133] A. Slavin and V. Tiberkevich, "Nonlinear auto-oscillator theory of microwave generation by spin-polarized current," *IEEE Transactions on Magnetics*, vol. 45, no. 4, pp. 1875–1918, 2009.

[134] M. R. Pufall, W. H. Rippard, S. E. Russek, and E. R. Evarts, "Anisotropic frequency response of spin-torque oscillators with applied field polarity and direction," *Physical Review B*, vol. 86, no. 9, p. 094404, 2012.

[135] T. Nozaki, Y. Shiota, S. Miwa, S. Murakami, F. Bonell, S. Ishibashi, H. Kubota, K. Yakushiji, T. Saruya, A. Fukushima *et al.*, "Electric-field-induced ferromagnetic resonance excitation in an ultrathin ferromagnetic metal layer," *Nature Physics*, vol. 8, no. 6, p. 491, 2012.

[136] D. Tiwari, N. Sisodia, R. Sharma, P. Dürrenfeld, J. Åkerman, and P. Muduli, "Enhancement of spin-torque diode sensitivity in a magnetic tunnel junction by parametric synchronization," *Applied Physics Letters*, vol. 108, no. 8, p. 082402, 2016.

[137] W. Chen, G. De Loubens, J.-M. Beaujour, J. Sun, and A. Kent, "Spin-torque driven ferromagnetic resonance in a nonlinear regime," *Applied Physics Letters*, vol. 95, no. 17, p. 172513, 2009.

[138] M. Laufenberg, W. Bührer, D. Bedau, P.-E. Melchy, M. Kläui, L. Vila, G. Faini, C. A. Vaz, J. A. C. Bland, and U. Rüdiger, "Temperature dependence of the spin torque effect in current-induced domain wall motion," *Physical Review Letters*, vol. 97, no. 4, p. 046602, 2006.

[139] M. Mohseni, M. Hamdi, H. F. Yazdi, S. A. H. Banuazizi, S. Chung, S. R. Sani, J. Åkerman, and M. Mohseni, "Magnetic droplet soliton nucleation in oblique fields," *Physical Review B*, vol. 97, p. 184402, May 2018.

[140] J. Slonczewski, "Currents and torques in metallic magnetic multilayers," *Journal of Magnetism and Magnetic Materials*, vol. 247, no. 3, pp. 324–338, 2002.

[141] M. Tsoi, A. Jansen, J. Bass, W.-C. Chiang, V. Tsoi, and P. Wyder, "Generation and detection of phase-coherent current-driven magnons in magnetic multilayers," *Nature*, vol. 406, no. 6791, p. 46, 2000.

[142] F. Macià, D. Backes, and A. D. Kent, "Stable magnetic droplet solitons in spin-transfer nanocontacts," *Nature nanotechnology*, vol. 9, no. 12, p. 992, 2014.

[143] C. Wang, D. Xiao, Y. Zhou, J. Åkerman, and Y. Liu, "Phase-locking of multiple magnetic droplets by a microwave magnetic field," *AIP Advances*, vol. 7, no. 5, p. 056019, 2017.

[144] D. Xiao, V. Tiberkevich, Y. Liu, Y. Liu, S. Mohseni, S. Chung, M. Ahlberg, A. Slavin, J. Åkerman, and Y. Zhou, "Parametric autoexcitation of magnetic droplet soliton perimeter modes," *Physical Review B*, vol. 95, no. 2, p. 024106, 2017.

[145] P. Wills, E. Iacocca, and M. Hoefer, "Deterministic drift instability and stochastic thermal perturbations of magnetic dissipative droplet solitons," *Physical Review B*, vol. 93, no. 14, p. 144408, 2016.

[146] S. Lendínez, N. Statuto, D. Backes, A. D. Kent, and F. Macià, "Observation of droplet soliton drift resonances in a spin-transfer-torque nanocontact to a ferromagnetic thin film," *Physical Review B*, vol. 92, no. 17, p. 174426, 2015.

[147] L. Bookman and M. Hoefer, "Perturbation theory for propagating magnetic droplet solitons," *Proceedings of the Royal Society of London A*, vol. 471, no. 2179, p. 20150042, 2015.

[148] S. Chung, A. Eklund, E. Iacocca, S. M. Mohseni, S. R. Sani, L. Bookman, M. A. Hoefer, R. K. Dumas, and J. Åkerman, "Magnetic droplet nucleation boundary in orthogonal spin-torque nano-oscillators," *Nature Communications*, vol. 7, p. 11209, 2016.

[149] D. Xiao, Y. Liu, Y. Zhou, S. M. Mohseni, S. Chung, and J. Åkerman, "Merging droplets in double nanocontact spin torque oscillators," *Physical Review B*, vol. 93, no. 9, p. 094431, 2016.

[150] A. Vansteenkiste, "A. vansteenkiste, j. leliaert, m. dvornik, m. helsen, f. garcia-sanchez, and b. van waeyenberge, aip adv. 4, 107133 (2014)." *AIP Advances*, vol. 4, p. 107133, 2014.

[151] S. M. Mohseni, H. Yazdi, M. Hamdi, T. Brächer, and S. M. Mohseni, "Current induced multi-mode propagating spin waves in a spin transfer torque nanocontact with strong perpendicular magnetic anisotropy," *Journal of Magnetism and Magnetic Materials*, vol. 450, pp. 40–45, 2018.

[152] S. Mangin, D. Ravelosona, J. Katine, M. Carey, B. Terris, and E. E. Fullerton, "Current-induced magnetization reversal in nanopillars with perpendicular anisotropy," *Nature Materials*, vol. 5, no. 3, p. 210, 2006.

[153] H. Meng and J.-P. Wang, "Spin transfer in nanomagnetic devices with perpendicular anisotropy," *Applied physics letters*, vol. 88, no. 17, p. 172506, 2006.

[154] S. Ikeda, K. Miura, H. Yamamoto, K. Mizunuma, H. Gan, M. Endo, S. Kanai, J. Hayakawa, F. Matsukura, and H. Ohno, "A perpendicular-anisotropy cofeb–mgo magnetic tunnel junction," *Nature Materials*, vol. 9, no. 9, p. 721, 2010.

[155] H. Meng, R. Sbiaa, S. Lua, C. Wang, M. Akhtar, S. Wong, P. Luo, C. Carlberg, and K. Ang, "Low current density induced spin-transfer torque switching in cofeb–mgo magnetic tunnel junctions with perpendicular anisotropy," *Journal of Physics D: Applied Physics*, vol. 44, no. 40, p. 405001, 2011.

[156] W.-G. Wang, M. Li, S. Hageman, and C. Chien, "Electric-field-assisted switching in magnetic tunnel junctions," *Nature Materials*, vol. 11, no. 1, p. 64, 2012.

[157] Z. Zeng, G. Finocchio, and H. Jiang, "Spin transfer nano-oscillators," *Nanoscale*, vol. 5, no. 6, pp. 2219–2231, 2013.

[158] K. Ando, S. Fujita, J. Ito, S. Yuasa, Y. Suzuki, Y. Nakatani, T. Miyazaki, and H. Yoda, "Spin-transfer torque magnetoresistive random-access memory technologies for normally off computing," *Journal of Applied Physics*, vol. 115, no. 17, p. 172607, 2014.

[159] A. Houshang, R. Khymyn, M. Dvornik, M. Haidar, S. Etesami, R. Ferreira, P. Freitas, R. Dumas, and J. Åkerman, "Faster, farther, stronger: spin transfer torque driven high order propagating spin waves in nano-contact magnetic tunnel junctions," *arXiv preprint arXiv:1712.00954*, 2017.

[160] U.-H. Pi, S.-C. Lee, K.-S. Kim, K. Kim, J.-K. Shin, and U.-i. Chung, "The effect of the static magnetic susceptibility on the spin precession in mgo based magnetic tunnel junction," *Applied Physics Letters*, vol. 98, no. 24, p. 242509, 2011.

[161] M. Tsoi, A. Jansen, J. Bass, W.-C. Chiang, M. Seck, V. Tsoi, and P. Wyder, "Excitation of a magnetic multilayer by an electric current," *Physical Review Letters*, vol. 80, no. 19, p. 4281, 1998.

[162] V. Demidov, H. Ulrichs, S. Gurevich, S. Demokritov, V. Tiberkevich, A. Slavin, A. Zholud, and S. Urazhdin, "Synchronization of spin hall nano-oscillators to external microwave signals," *Nature Communications*, vol. 5, 2014.

[163] M. Ranjbar, P. Dürrenfeld, M. Haidar, E. Iacocca, M. Balinskiy, T. Le, M. Fazlali, A. Houshang, A. Awad, R. Dumas, and J. Åkerman, "Cofeb-based spin hall nano-oscillators," *IEEE Magnetics Letters*, vol. 5, pp. 1–4, 2014.

[164] P. Dürrenfeld, F. Gerhard, M. Ranjbar, C. Gould, L. Molenkamp, and J. Åkerman, "Spin hall effect-controlled magnetization dynamics in nimnsb," *Journal of Applied Physics*, vol. 117, no. 17, p. 17E103, 2015.

[165] M. Zahedinejad, A. A. Awad, P. Dürrenfeld, A. Houshang, Y. Yin, P. K. Muduli, and J. Åkerman, "Current modulation of nanoconstriction spin-hall nano-oscillators," *IEEE Magnetics Letters*, vol. 8, pp. 1–4, 2017.

[166] E. De Ranieri, A. Rushforth, K. Vỳbornỳ, U. Rana, E. Ahmad, R. Campion, C. Foxon, B. Gallagher, A. Irvine, J. Wunderlich, and T. Jungwirth, "Lithographically and electrically controlled strain effects on anisotropic magnetoresistance in (ga, mn) as," *New Journal of Physics*, vol. 10, no. 6, p. 065003, 2008.

[167] V. Demidov, S. Urazhdin, A. Zholud, A. Sadovnikov, and S. Demokritov, "Nanoconstriction-based spin-hall nano-oscillator," *Applied Physics Letters*, vol. 105, no. 17, p. 172410, 2014.

[168] A. Vansteenkiste, J. Leliaert, M. Dvornik, M. Helsen, F. Garcia-Sanchez, and B. Van Waeyenberge, "The design and verification of mumax3," *AIP Advances*, vol. 4, no. 10, p. 107133, 2014.

[169] T. Kendziorczyk and T. Kuhn, "Mutual synchronization of nanoconstriction-based spin hall nano-oscillators through evanescent and propagating spin waves," *Physical Review B*, vol. 93, no. 13, p. 134413, 2016.

Chapter 7

Papers